INVESTIGATIONS ON THREE APPROACHES FOR IMPROVING POWDER BED ADDITIVE MANUFACTURING

A Dissertation

by

WENCHAO DU

Submitted to the Graduate and Professional School of
Texas A&M University
in partial fulfillment of the requirements for the degree of

DOCTOR OF PHILOSOPHY

Chair of Committee,	Chao Ma
Co-Chair of Committee,	Zhijian Pei
Committee Members,	Alaa Elwany
	Miladin Radovic
Head of Department,	Lewis Ntaimo

December 2021

Major Subject: Industrial Engineering

ABSTRACT

The objective of this research is to investigate three approaches for improving the bulk density or mechanical strength of the parts from powder bed additive manufacturing technologies, with a focus on binder jetting additive manufacturing. At the beginning, a literature review was conducted to target the density issue. This review began with an overview of the process, material considerations, and process parameters. It then discussed different aspects of density. Afterward, it reviewed two categories of techniques to increase the part density: material preparation techniques and post-processing techniques. Finally, it presented the knowledge gaps in the literature.

Afterward, three approaches, i.e., powder mixing, powder coating, and powder granulation were studied. For the powder mixing approach, an analytical model was used first to study the mixture packing density. Both modeling and experimental results showed that powder mixtures (binary or ternary) with a multimodal particle size distribution could achieve a higher packing density than their component powders and there existed an optimal mixing fraction to achieve the maximum mixture packing density. Afterward, theoretical tools to select parameters for the powder mixing approach were established. Moreover, three linear packing models (de Larrard's, Kwan's, and Yu's) were assessed for their prediction performances on micropowder mixtures in terms of predicted powder packing densities and optimal mixing fractions. Results showed that Kwan's model achieved the best prediction performance on powder packing density. In terms of optimal mixing fraction, the prediction performance depends on the specific mixing system.

A new powder surface modification method, i.e., particle coating, was applied to increase the powder sinterability and the part strength. Specifically, coarse crystalline alumina particles were coated with amorphous alumina, in which the micron-sized core was designed to provide the high flowability and the amorphous shell to promote sintering due to its high activity. The sintered samples from the coated powders demonstrated enhanced necking, increased diameter shrinkage, and improved compressive strength, compared with those from the raw powders.

For powder granulation approach, powders were firstly prepared using spray freeze drying and the effects of preparation parameters on the powder properties were studied. Results showed that a low spraying pressure and a high feed rate led to a large granule size and consequently a higher flowability. Thereafter, the granulated powder from spray freeze drying was compared with nanopowder and micropowder in terms of flowability and sinterability. Results showed that the granulated powder had both a high flowability and a high sinterability. Finally, a granulation method called direct freeze drying was used to prepare the granulated powders from slurries with different solid loadings. Powder spreading and compaction tests were conducted on a commercially available binder jetting 3D printer equipped with a forward-rotating roller compaction system. Results showed that a low slurry solid loading could enhance the powder bed density in roller-compaction-assisted binder jetting.

ACKNOWLEDGEMENTS

I would like to thank my committee chair, Dr. Chao Ma, and co-chair, Dr. Zhijian Pei, for their guidance and support throughout the course of this research. Dr. Ma always provides the most valuable guidance, under which I can take full advantage of this research to enhance my research skills and expand my expertise. Dr. Pei always offers remarkable input to my research activities by not only advising me on the how but also going deep for the why. It is under their tremendous support that I can gain the knowledge for this dissertation, set my career pathway, and keep a permanent curiosity for research.

I would like to acknowledge Dr. Dileep Singh at Argonne National Laboratory for offering the visiting opportunity. Thanks go to Dr. Alaa Elwany and Dr. Miladin Radovic for serving in my doctoral committee. I also want to thank my colleagues in the research group for the advice and collaboration. Support from Dr. Xiaorui Ren at my early stage of research is greatly appreciated. Thanks also go to my friends and the department faculty and staff for making my time at Texas A&M University a great experience.

Sections 2–4 and 6–7 are based upon work supported by the National Science Foundation under Grant No. 1762341 (Division of Civil, Mechanical and Manufacturing Innovation). Section 5 did not receive any specific grant from funding agencies in the public, commercial, or not-for-profit sectors. Section 8 is based upon work supported by the National Science Foundation under Grant No. 2047908 (Division of Civil, Mechanical and Manufacturing Innovation).

Finally, thanks to my family for the encouragement and love.

CONTRIBUTORS AND FUNDING SOURCES

Contributors

This work was supervised by a dissertation committee consisting of Professor Ma [advisor] of the Department of Engineering Technology and Industrial Distribution, Professors Pei [co-advisor] and Elwany of the Department of Industrial and Systems Engineering, and Professor Radovic of the Department of Materials Science and Engineering.

Some of the scanning electron microscope images in Chapters 3 and 4 were acquired with the aid of Mr. Ming Li. The experimental work in Chapter 5 was conducted with the aid of Dr. Xiaorui Ren. The powder preparation work in Chapters 6 and 7 was conducted with the aid of Mr. Guanxiong Miao.

All other work conducted for the dissertation was completed by the student independently.

Funding Sources

Graduate study was supported by startup funding from Texas A&M University and research funding from National Science Foundation under Grant Numbers [1762341] and [2047908].

TABLE OF CONTENTS

Page

LIST OF FIGURES

Page

LIST OF TABLES

Page

1. INTRODUCTION

Additive manufacturing (AM), also known as 3D printing, can be described as the process of joining or adding materials for making objects from 3D model data using a layer-by-layer principle [1]. The AM market is increasing rapidly every year, from $12 billion in 2020 to an expected $51 billion by 2030, representing a compound annual growth rate of 15% [2]. According to the ASTM standard [1], most AM technologies can be classified into seven categories: binder jetting, vat photopolymerization, powder bed fusion, directed energy deposition, material extrusion, material jetting, and sheet lamination. Binder jetting and powder bed fusion have a similar working principle. Binder jetting (BJ) is defined by ASTM as "an additive manufacturing process in which a liquid bonding agent is selectively deposited to join powder materials." Powder bed fusion (PBF) is defined by ASTM as "an additive manufacturing process in which thermal energy selectively fuses regions of a powder bed." Both BJ and PBF involve a powder bed and thus can be classified into powder bed AM.

Various materials, including polymers, metals, ceramics, and composites, can all be printed using powder bed AM technologies. Powder bed AM has been widely investigated in the literature to overcome the limitations of conventional manufacturing techniques [3,4]. For example, it is sometimes very costly to fabricate objects of complex shapes using conventional manufacturing techniques due to the high cost of tooling. Other disadvantages of conventional techniques include excessive cost in prototyping and difficulty to make design changes.

Although powder bed AM can overcome some limitations of conventional manufacturing techniques, tremendous research is still required. Many researchers have reported binder jetting studies using different feedstock materials [5–8] and different post-processing methods [9–12]. However, the relative bulk density of pure ceramic materials by only printing and sintering is low

according to the reported studies in the literature [12–15]. This low density (and consequent inferior mechanical properties) is the main disadvantage and the most challenging problem in the field of ceramic binder jetting AM.

The objective of this research is to investigate three approaches for improving the bulk density or mechanical strength of the parts printed from powder bed AM technologies, with a focus on binder jetting. At the beginning, a literature review was conducted. Afterward, three approaches, i.e., powder mixing, powder coating, and powder granulation were studied. It should be noted that alumina was chosen as the model material and binder jetting as the model powder bed AM technology. Although only one material and one AM technology were tested, some knowledge in this dissertation maintain their potentialities for other materials and other powder bed AM technologies.

The dissertation outline is shown in Figure 1.1. Chapter 2 contains a literature review, which was to summarize the current status and identify the knowledge gaps in ceramic binder jetting, with a particular focus on density. Chapter 3 presents a study of both modeling and experiments of the powder mixing approach and its effect on density. Chapter 4 reports an assessment study of three powder packing models in terms of prediction performances on powder packing density and optimal mixing fraction. Chapter 5 focuses on the powder coating approach to increases the powder sinterability and consequent part mechanical properties. Chapters 6–8 report three studies of the powder granulation approach. In Chapter 6, a granulated powder was prepared with spray freeze drying, and the effects of preparation parameters on the powder properties were studied. In Chapter 7, a study on the comparison of powder flowability and sinterability was conducted among three powders: nanopowder, micropowder, and granulated powder. In Chapter 8, the effects of

granulated powder preparation on powder bed conditions in roller-compaction-assisted binder jetting were studied. Conclusions were drawn based on the results in each chapter.

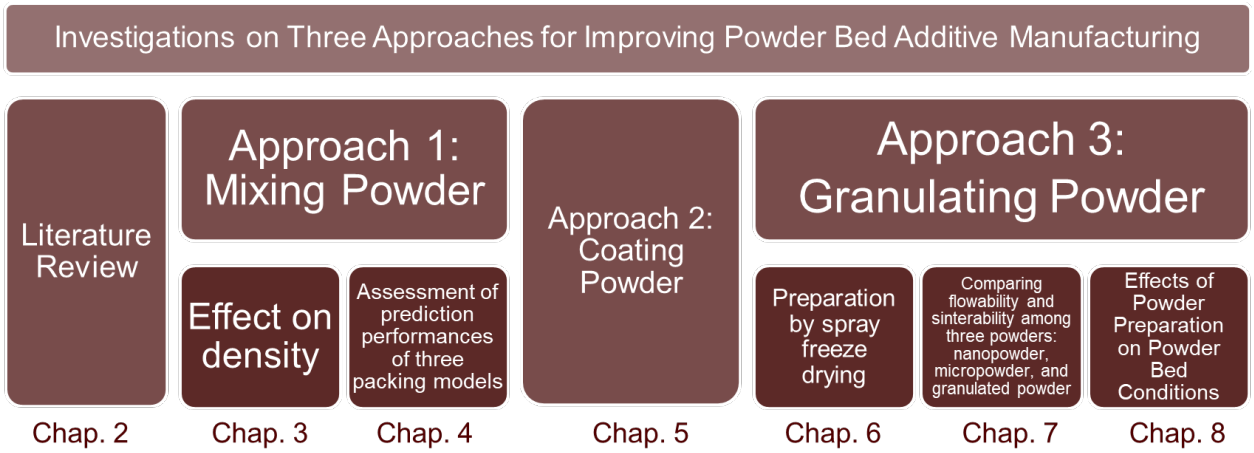

Figure 1.1 Dissertation outline

1.1. References

[1] ASTM International, 2012, "F2792-12a: Standard Terminology for Additive Manufacturing Technologies."

[2] "Additive Manufacturing Market Forecast to Reach $51 Billion by 2030" [Online]. Available: https://www.metal-am.com/am-market-forecast-to-reach-51-billion-by-2030/. [Accessed: 25-Sep-2021].

[3] Li, M., Du, W., Elwany, A., Pei, Z., and Ma, C., 2020, "Metal Binder Jetting Additive Manufacturing: A Literature Review," Journal of Manufacturing Science and Engineering, **142**(9), p. 090801 (17 pages).

[4] Abdulhameed, O., Al-Ahmari, A., Ameen, W., and Mian, S. H., 2019, "Additive Manufacturing: Challenges, Trends, and Applications," Advances in Mechanical Engineering, **11**(2), pp. 1–27.

[5] Sachs, E., Cima, M., and Cornie, J., 1990, "Three Dimensional Printing: Rapid Tooling and Prototypes Directly from CAD Pepresentation," *Solid Freeform Fabrication Symposium*, Austin, TX, pp. 27–47.

[6] Díaz-Moreno, C. A., Lin, Y., Hurtado-Macías, A., Espalin, D., Terrazas, C. A., Murr, L. E., and Wicker, R. B., 2019, "Binder Jetting Additive Manufacturing of Aluminum Nitride Components," Ceramics International, **45**(11), pp. 13620–13627.

[7] Suwanprateeb, J., Sanngam, R., Suvannapruk, W., and Panyathanmaporn, T., 2009, "Mechanical and in Vitro Performance of Apatite-Wollastonite Glass Ceramic Reinforced Hydroxyapatite Composite Fabricated by 3D-Printing," Journal of Materials Science: Materials in Medicine, **20**(6), pp. 1281–1289.

[8] Du, W., Singh, M., and Singh, D., 2020, "Binder Jetting Additive Manufacturing of Silicon Carbide Ceramics: Development of Bimodal Powder Feedstocks by Modeling and Experimental Methods," Ceramics International, **46**(12), pp. 19701–19707.

[9] Grant, L. O., Alameen, M. B., Carazzone, J. R., Fred, C., Iii, H., and Cordero, Z. C., 2018, "Mitigating Distortion During Sintering of Binder Jet Printed Ceramics," *Solid Freeform Fabrication Symposium*, Austin, TX, pp. 135–142.

[10] Rabinskiy, L., Ripetsky, A., Sitnikov, S., Solyaev, Y., and Kahramanov, R., 2016, "Fabrication of Porous Silicon Nitride Ceramics Using Binder Jetting Technology," IOP Conference Series Materials Science and Engineering, **140**(1), pp. 1–6.

[11] Maleksaeedi, S., Eng, H., Wiria, F. E., Ha, T. M. H., and He, Z., 2014, "Property Enhancement of 3D-Printed Alumina Ceramics Using Vacuum Infiltration," Journal of Materials Processing Technology, **214**(7), pp. 1301–1306.

[12] Yoo, J., Cima, M. J., Khanuja, S., and Sachs, E. M., 1993, "Structural Ceramic Components by 3D Printing," *Solid Freeform Fabrication Symposium*, Austin, TX, pp. 40–50.

[13] Melcher, R., Travitzky, N., Zollfrank, C., and Greil, P., 2011, "3D Printing of Al2O3/Cu-O Interpenetrating Phase Composite," Journal of Materials Science, **46**(5), pp. 1203–1210.

[14] Mariani, M., Beltrami, R., Brusa, P., Galassi, C., Ardito, R., and Lecis, N., 2021, "3D Printing of Fine Alumina Powders by Binder Jetting," Journal of the European Ceramic Society, **41**(10), pp. 5307–5315.

[15] Du, W., Ren, X., Pei, Z., and Ma, C., 2020, “Ceramic Binder Jetting Additive Manufacturing: A Literature Review on Density,” Journal of Manufacturing Science and Engineering, **142**(4), p. 040801 (19 pages).

2. LITERATURE REVIEW ON CERAMIC BINDER JETTING ADDITIVE MANUFACTURING*

2.1. Introduction

Ceramic materials can have outstanding properties, such as extraordinary hardness, excellent resistance to wear, heat, and corrosion, and exceptional biocompatibility. Therefore, ceramic materials have a wide range of applications, from orthopaedic and dental implants in the biomedical industry to engine components in the aerospace and automotive industries. However, it is very costly to fabricate ceramic parts of complex shapes using conventional manufacturing techniques. For complex ceramic parts, tooling can contribute up to 80% of the overall cost if conventional techniques are used [1]. Conventional techniques have other disadvantages including excessive cost in prototyping and difficulty to make design changes. All these disadvantages have impeded the widespread applications of advanced ceramic materials (e.g., alumina, zirconia, and silicon carbide). For example, there are millions of joint replacement surgeries every year [2]. Although ceramic materials are an excellent choice for joint implants because of their excellent wear resistance and exceptional biocompatibility [3], they are not widely utilized because it is not cost-effective to fabricate them using conventional manufacturing technologies [4].

According to the ASTM standard [5], most additive manufacturing (AM) technologies can be classified into seven categories: binder jetting, vat photopolymerization, powder bed fusion, directed energy deposition, material extrusion, material jetting, and sheet lamination. Binder jetting is defined by ASTM as "additive manufacturing processes in which a liquid bonding agent is selectively deposited to join powder materials" [5]. Binder jetting was initially developed at

Massachusetts Institute of Technology in the late 1980s [6,7] and commercialized by Soligen in 1993 [8], Z Corporation [9] and Therics [10] in 1997, ExOne in 2001 [11], Voxeljet in 2002 [12], Microjet in 2016 [13], and Desktop Metal [14] and Digital Metal [15] in 2017. After presenting their innovation in various conference [7,16,17] and journal [18,19] papers, the inventors investigated various perspectives of this technology, including the powder bed density improvement [20,21], powder-binder interaction [22,23], new feedstock form (i.e., slurry instead of powder) [24–31], and potential application areas (e.g., casting cores and shells [32], optical lenses [29], cutting tools [33], and biomedical devices [34]).

Table 2.1 summarizes advantages and disadvantages of the seven AM categories for printing ceramic materials. Compared with others, binder jetting has some unique features. First, the surrounding powder supports the printed part during the building process. Therefore, there is no need for explicit support structures for overhangs and undercuts [35]. Secondly, the amount of binder in the green body is low, and thus debinding is much easier for large parts than some other processes such as vat photopolymerization [36,37]. Thirdly, as print heads can consist of up to thousands of jets working in parallel, binder jetting is easily scalable for fabricating large parts [38]. Moreover, binder jetting is suitable for biomedical applications due to its capability of printing functionally graded materials [39]. For example, bioinks with drugs can be added to the binder [40].

Table 2.1 Advantages and disadvantages of various AM categories for ceramics

Category	Advantage	Disadvantage
Binder jetting	No need for support [35], minimal amount of sacrificial materials [37], high scalability [38]	High porosity [41]
Vat photopolymerization	Excellent resolution and accuracy [42], smooth surface [42], high density [41]	Limited part size
Powder bed fusion (indirect)	No need for support	High porosity
Material extrusion	Low cost, high density, multiple materials within a part [43]	Low resolution [41], interfacial porosity
Material Jetting	Excellent surface quality [42], multiple materials within a part	Limited part size
Directed energy deposition	High density [44]	Thermal cracks [45]
Sheet lamination	High speed, no need for support	Delamination, interfacial porosity [41]

Several review papers on ceramic AM have discussed binder jetting. The first one [46], which was published in 2003, discussed its process, dimensional control, and applications. Other four ceramic AM review papers, published in 2014 [42,47], 2015 [41], and 2017 [48], also included binder jetting. Travitzky et al. [42] reviewed the dimensional control methods and several applications in the orthopaedic field. Deckers et al. [47] reviewed the low-density issue of ceramic binder jetting. Zocca et al. [41] reviewed the material preparation methods to improve the powder bed density, while Yang et al. [48] discussed the advantages and material limitations of ceramic binder jetting. A recent review paper about binder jetting summarized various powder deposition methods, reviewed binder selection criteria, and discussed key printing parameters such as binder saturation and layer thickness [49]. In addition to these review papers, a book chapter also reviewed some ceramic materials that have been used in binder jetting, including several applications related to these materials [50].

The literature has reported an increasing number of studies on binder jetting. Various techniques have been reported to improve the density (and mechanical properties in some cases) of printed parts. However, there are no review papers devoted to ceramic binder jetting that comprehensively compile the available reports in the literature on density improvement. This literature review is to fill the gap.

This paper first provides an overview of ceramic binder jetting, including the process, materials, and resultant densities. The focus of this review is to summarize and analyze reported techniques for density improvement, which is considered as the most challenging issue in this field. Finally, existing knowledge gaps are identified.

2.2. Description of Ceramic Binder Jetting

2.2.1. Process overview

Figure 2.1 illustrates major components of binder jetting equipment, including powder stock, build platform, spreader, binder cartridge, and print head. The printing process is as follows. First, the spreader deposits a thin layer of powder from the powder stock onto the build platform, forming the powder bed. Then the print head jets binder onto selected areas defined by a 3D model to bond the powder particles in these areas. After one layer is finished, the build platform is lowered and the powder stock is raised, after which a new powder layer is spread onto the finished layer. These steps are repeated until the whole part is printed. The printed part is then separated from the loose powder after curing [6,37].

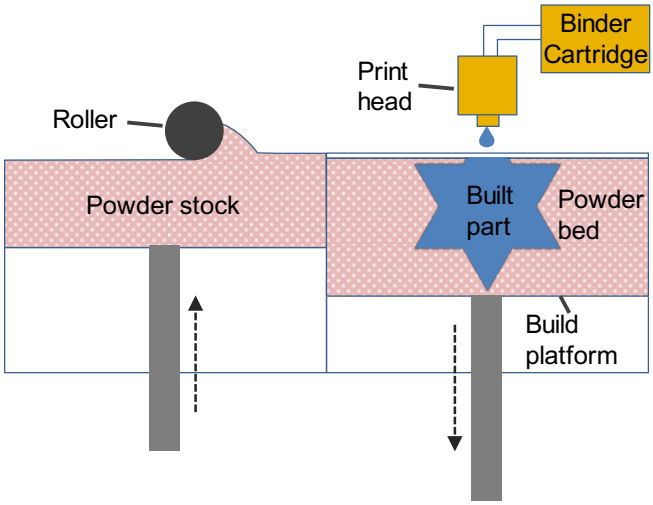

Figure 2.1 Major components of binder jetting equipment

A generic cycle of ceramic binder jetting is shown in Figure 2.2. The feedstock is ceramic powder. The powder needs to meet certain requirements (e.g., high flowability and sinterability to be discussed in Section 1.2.3) for making high-quality parts. The printed part is called “green part”. The green part is then heated to a specific temperature (usually around 200°C), during which the binder is thermally activated by solvent evaporation, polymerization, cross-linking, or other mechanisms to strengthen the green part [42,47]. It should be noted that curing can be applied layer by layer [51]. Curing temperature could be higher (up to 800°C) if an inorganic binder, usually colloidal silica [18], is used.

Afterward, post-processing steps (such as debinding and sintering) are usually applied to the green parts to improve their material properties. In the debinding step, the binder is thermally decomposed or burned out by heat treatment between 400 °C and 800 °C, producing a “brown part”. The heating rate is controlled to ensure the escape of gaseous reaction products. In the sintering step, the part is heated to a high temperature (usually just below the melting point of the ceramic material), followed by dwelling and furnace cooling. The sintering step increases the density of the part by mass transport across the boundaries of ceramic particles [52]. Other

densification techniques (e.g., isostatic pressing, infiltration, etc.) can also be used to further increase the density and thus mechanical properties. However, they may compromise other properties such as geometrical accuracy, biocompatibility, and heat resistance. Details of some post-processing steps are reviewed in Section 1.5.

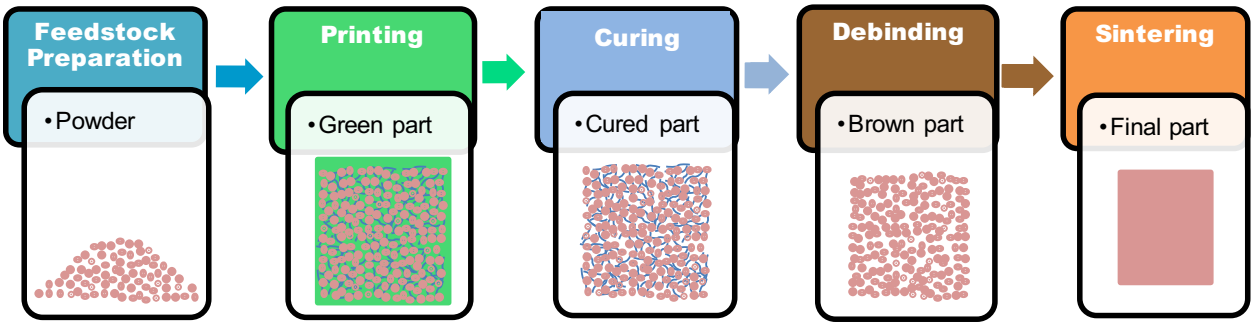

Figure 2.2 Steps of ceramic binder jetting

2.2.2. Materials and applications

Figure 2.3 shows the proportions of application areas of ceramic binder jetting in reported studies. The application with the highest number of papers is in the orthopaedic field to make bone scaffolds and implants. The structural application has the second highest number of papers. A small number of dentures and crowns are reported as well. For electronic applications, fabrication of dielectric radio frequency filters and ferroelectric dielectric capacitors is reported. There is also one paper about the fabrication of a gradient-index lens for optical application.

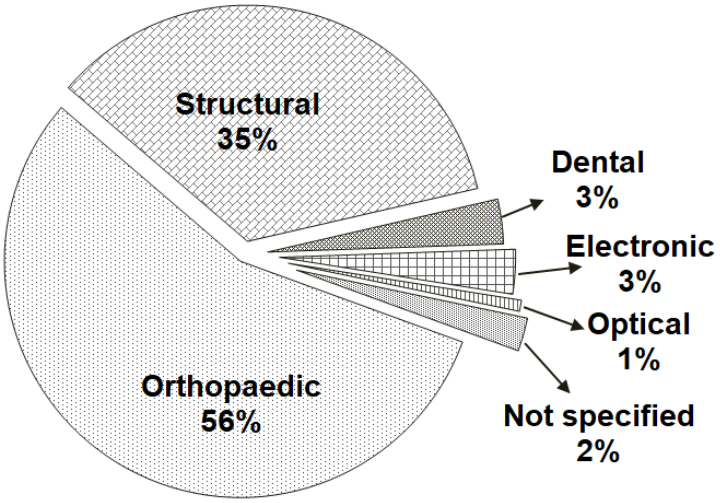

Figure 2.3 Proportions of various application areas of ceramic binder jetting reported in the literature

Table 2.2 summarizes the reported materials grouped by their application areas. Sometimes, the feedstock and resultant materials (if identified) are different and thus listed in different columns. Additives and infiltrants are also included.

Table 2.2 Feedstock and resultant materials reported in ceramic binder jetting

Application	Feedstock material	Additive (A) or infiltrant (I)	Resultant material	Reference
Structural	Al	/	Al_2O_3	[53]
Structural	Al+Al_2O_3	/	Al_2O_3	[54]
Structural	AlN	/	AlN	[55,56]
Structural	Al_2O_3	/	Al_2O_3	[7,18,19,23,24,38,57–68]
Structural	Al_2O_3	(I) Al_2O_3	Al_2O_3	[69]
Structural	Al_2O_3	(I) Cu+Cu_2O	Al_2O_3+Cu+Cu_2O	[67,70]
Structural	Al_2O_3	(I) Glass	Al_2O_3+Glass	[71]
Structural	Al_2O_3+ZrO_2	/	Al_2O_3+ZrO_2	[72]
Structural	B_4C+SiC	/	B_4C+SiC	[73]
Structural	CaO	(A) ZrO_2	CaO+$CaZrO_3$	[74]
Structural	$CaSO_4 \cdot 0.5H_2O$		$CaSO_4 \cdot 0.5H_2O$	[75]
Structural	$CaSO_4 \cdot 0.5H_2O$	(I) $C_{21}H_{25}ClO_5$	$C_{21}H_{25}ClO_5$+$CaSO_4$	[76]
Structural	Porcelain	/	Porcelain	[77]
Structural	Si	/	SiC+Si_3N_4+SiON	[78,79]
Structural	Si+SiC	(I) Silicone	SiSiC	[80]

Structural	SiC	(I) Si	SiSiC	[81,82]
Structural	Silicone	/	SiOC	[83]
Structural	Si_3N_4	/	Si_3N_4	[24]
Structural	SiO_2	(I) Al	$Al+Al_2O_3$	[84]
Structural	TiC	(I) Si	$Ti_3SiC_2+TiSi_2+TiC+SiC$	[85]
Structural	$TiC+TiO_2$	(I) Al	$Al+Al_2O_3+TiAl_3$	[86]
Structural	$TiC+TiO_2$	(I) Al	$Al+Al_2O_3+TiAl_3+Ti_3AlC_2+TiC$	[87]
Structural	$TiC+TiO_2$	(I) Al	$Al_2O_3+TiAl_3+Ti_3AlC_2$	[88]
Structural	Ti_3SiC_2	/	Ti_3SiC_2	[89,90]
Structural	WC+Co	/	WC+Co	[91–93]
Structural	ZrO_2	/	ZrO_2	[94]
Orthopaedic	Bioactive glass	/	Bioactive glass	[95–97]
Orthopaedic	Bioactive glass+$Ca_5(PO_4)_3(OH)$	/	Bioactive glass+$Ca_5(PO_4)_3(OH)$	[98]
Orthopaedic	Bioactive glass+$Ca_3(PO_4)_2$	/	/	[99,100]
Orthopaedic	Bioactive glass+$Ca_5(PO_4)_3(OH)$	/	$Ca_3(PO_4)_2+Ca_5(PO_4)_3(OH)+Ca_2SiO_4$	[101]
Orthopaedic	Bioactive glass+$CaCO_3$+Silicone	/	$Ca_5(PO_4)_3F+Ca_5(PO_4)_3(OH)+CaSiO_3+Ca_2SiO_4+SiO_2$	[102]
Orthopaedic	$Ca_8H_2(PO_4)_6\cdot 5H_2O$	/	$Ca(HPO_4)\cdot 2H_2O+Ca_3(PO_4)_2$	[103]
Orthopaedic	$Ca(HPO_4)+Ca(OH)_2$	/	$Ca(HPO_4)+Ca(OH)_2+Ca_5(PO_4)_3(OH)$ or $Ca(HPO_4)+Ca_3(PO_4)_2$	[104]
Orthopaedic	$CaO+Na_2O+P_2O_5+SiO_2$	/	$CaO+Na_2O+P_2O_5+SiO_2$	[105,106]
Orthopaedic	$[Ca(PO_3)_2]_n$	/	$[Ca(PO_3)_2]_n$	[107,108]
Orthopaedic	$Ca_3(PO_4)_2$	/	/	[109–112]
Orthopaedic	$Ca_3(PO_4)_2$	/	$Ca(HPO_4)$	[113–116]
Orthopaedic	$Ca_3(PO_4)_2$	/	$Ca(HPO_4)+Ca(HPO_4)\cdot 2H_2O$	[117]
Orthopaedic	$Ca_3(PO_4)_2$	/	$Ca(HPO_4)+Ca(HPO_4)\cdot 2H_2O+Ca_3(PO_4)_2$	[118–120]
Orthopaedic	$Ca_3(PO_4)_2$	/	$Ca(HPO_4)\cdot 2H_2O$	[121]
Orthopaedic	$Ca_3(PO_4)_2$	/	$Ca(HPO_4)\cdot 2H_2O+Ca_3(PO_4)_2$	[122,123]
Orthopaedic	$Ca_3(PO_4)_2$	/	$Ca_3(PO_4)_2$	[124–135]
Orthopaedic	$Ca_3(PO_4)_2$	(A) $MgO+SiO_2$	$Ca_3(PO_4)_2+MgO+SiO_2$	[134]
Orthopaedic	$Ca_3(PO_4)_2$	(A) MgO+SrO	$Ca_3(PO_4)_2+MgO+SrO$	[132,133]
Orthopaedic	$Ca_3(PO_4)_2$	(A) SiO_2+ZnO	$Ca_3(PO_4)_2+SiO_2+ZnO$	[135]
Orthopaedic	$Ca_3(PO_4)_2+CaCO_3$	/	$Ca_3(PO_4)_2+Ca_5(PO_4)_3(OH)$	[136]

Orthopaedic	$Ca_3(PO_4)_2$+$Ca_4(PO_4)_2O$	/	$Ca_4(PO_4)_2O$+$Ca_5(PO_4)_3(OH)$	[137]
Orthopaedic	$Ca_3(PO_4)_2$+$Ca_5(PO_4)_3(OH)$	/	$Ca(HPO_4)$+$Ca_3(PO_4)_2$+$Ca_5(PO_4)_3(OH)$	[138]
Orthopaedic	$Ca_3(PO_4)_2$+$Ca_5(PO_4)_3(OH)$	/	/	[139,140]
Orthopaedic	$Ca_3(PO_4)_2$+$Ca_5(PO_4)_3(OH)$	/	$Ca_3(PO_4)_2$+$Ca_5(PO_4)_3(OH)$	[141–144]
Orthopaedic	$Ca_3(PO_4)_2$+$Ca_5(PO_4)_3(OH)$+$CaSO_4$	/	$Ca_5(PO_4)_3(OH)$+$CaSO_4·2H_2O$	[145]
Orthopaedic	$Ca_4(PO_4)_2O$	/	$Ca(HPO_4)$+$Ca(HPO_4)·2H_2O$+$Ca_3(PO_4)_2$	[120]
Orthopaedic	$Ca_5(PO_4)_3(OH)$	/	/	[146–148]
Orthopaedic	$Ca_5(PO_4)_3(OH)$	/	$Ca_5(PO_4)_3(OH)$	[35,126,127,149–154]
Orthopaedic	$Ca_5(PO_4)_3(OH)$	(I) Bioactive polymer	Bioactive polymer+$Ca_5(PO_4)_3(OH)$	[155]
Orthopaedic	$CaSO_4$	/	$CaSO_4·0.5H_2O$	[156–158]
Orthopaedic	$CaSO_4·0.5H_2O$	/	$Ca_5(PO_4)_3(OH)$	[159]
Orthopaedic	$CaSO_4·0.5H_2O$	/	$CaSO_4·2H_2O$	[160]
Orthopaedic	$CaSO_4·0.5H_2O$	/	$Ca_5(PO_4)_3(OH)$+$CaSO_4·0.5H_2O$	[161]
Orthopaedic	$CaSO_4·0.5H_2O$	/	$Ca_5(PO_4)_3(OH)$+$CaSO_4·2H_2O$	[159,160]
Orthopaedic	$CaSO_4·0.5H_2O$	/	$Ca(HPO_4)$+$Ca_5(PO_4)_3(OH)$+$CaSO_4·2H_2O$	[160]
Orthopaedic	$CaSO_4·0.5H_2O$	/	$CaCO_3$+$CaSO_4$+$CaSO_4·2H_2O$	[162]
Orthopaedic	$CaSO_4·0.5H_2O$	(A) $AgNO_3$	Ag_3PO_4+$Ca_5(PO_4)_3(OH)$	[163]
Orthopaedic	$CaSO_4·0.5H_2O$	(I) $(C_6H_{10}O_2)n$	$(C_6H_{10}O_2)n$+$Ca_5(PO_4)_3(OH)$	[159]
Orthopaedic	$Mg_3(PO_4)_2$	/	$Mg_3(PO_4)_2$	[164]
Orthopaedic	$Mg_3(PO_4)_2$+$Mg_5Sr(PO_4)_4$+$Mg_2Sr(PO_4)_2$	/	$MgHPO_4·3H_2O$+$Mg(OH)_2$+$SrCO_3$	[164]
Orthopaedic	$Mg_3(PO_4)_2$+$(NH_4)_2HPO_4$	/	$NH_4MgPO_4·6H_2O$	[165]
Electronic	Al_2O_3	/	Al_2O_3	[25,27,166]
Electronic	$BaTiO_3$	/	$BaTiO_3$	[27,167,168]
Electronic	Si_3N_4	/	Si_3N_4	[25]
Dental	Al_2O_3	(I) Dental glass	Al_2O_3+Dental glass	[169]
Dental	Dental porcelain	/	Dental porcelain	[170,171]

Dental	Dental porcelain	(A) Al_2O_3	Al_2O_3+Dental porcelain	[172]
Optical	SiO_2	/	SiO_2	[173]

Materials investigated for structural applications include oxides (Al_2O_3, TiO_2, ZrO_2), carbides (WC, TiC, SiC), and nitrides (AlN, Si_3N_4). For orthopaedic applications, materials in the calcium phosphate family, such as hydroxyapatite (HA, $Ca_5(PO4)_3(OH)$) and tricalcium phosphate (TCP, $Ca_3(PO_4)_2$), are the most common choice due to their compositional similarity to human bones and thus excellent biocompatibility [174]. Other calcium phosphate materials include calcium polyphosphate (CPP, $[Ca(PO_3)_2]_n$), tetracalcium phosphate (TTCP, $Ca_4(PO_4)_2O$), and dicalcium phosphate (DCP, $CaHPO_4$). Alumina is the first material studied by the inventors of binder jetting [6,7]. In the past decades, it is also one of the mostly studied materials in different applications including structural, electronic, and dental areas.

In addition to the pure compound materials, a large portion of studies used composites to enhance various properties. For example, 12.5 vol.% zirconia was mixed with 40 vol.% alumina slurry to attain optimum strength for the printed and sintered parts [72]. Although composite materials can offer improved properties, they sometimes sacrifice other properties, such as biocompatibility [37].

2.2.3. Feedstock powder

Feedstock powder and its deposition method [175] determine various physical and chemical processes during fabrication, such as powder spreading, binder-powder interaction, and sintering densification. This section discusses important feedstock powder parameters and deposition methods.

2.2.3.1. Powder flowability

Flowability, the ability of a powder to freely flow, is crucial for uniform powder spreading [176] and thus homogeneous green and sintered part structure [48]. Flowability [102,167] is also called depositability [177], mobility [59], pourability [42], and spreadability [69,75,110,169].

Flowability can be assessed using different metrics, including flow factor (ff_c) [109,110], Hausner Ratio (*HR*) [11, 43, 79–81], Carr Index (*CI*) [178], and flow rate [147,150,152], among others. Flow factor is defined by the following equation,

$$ff_c = \frac{\sigma_1}{\sigma_c} \tag{1}$$

where σ_1 is the consolidation stress and σ_c is the compression strength, both of which can be measured with a ring shear tester [109,110].

Hausner Ratio [11, 43, 79–81] is defined by the following equation,

$$HR = \frac{\rho_t}{\rho_a} \tag{2}$$

where ρ_t and ρ_a are the tap density (the density of powder after a certain number of tapping cycles [64,97,179,180]) and apparent density (the density of freely settled powder), respectively. *HR* value is always larger than or equal to one. A smaller *HR* value, i.e., closer to one, indicates better flowability. Carr Index [178] is similar to Hausner Ratio. A smaller index value indicates better flowability. Its definition and relationship with Hausner Ratio are shown as follows,

$$CI = 100\left(1 - \frac{\rho_a}{\rho_t}\right) \tag{3}$$

$$CI = 100\left(1 - \frac{1}{HR}\right) \tag{4}$$

Flow rate is usually measured by a Hall flowmeter [147,150,152], in which a defined volume of powder passes through a small opening of a metal funnel. The flow rate can be represented by

the total time required for a certain amount of powder to pass [91,150] or the mass of the powder passing through in a unit time [147,152].

2.2.3.2. Powder Sinterability

Sintering is "a thermal treatment for bonding particles into a coherent, predominantly solid structure via mass transport events that often occur on the atomic scale" [181]. It is affected by powder properties and packing state. Powder sinterability is used to compare the sintering performance of different powders under a similar packing condition, and it is important for the selection of the optimal feedstock material before printing. Sintered bulk density is commonly used to describe powder sinterability since high sinterability leads to high sintered density under same conditions [52]. Volumetric shrinkage is another sinterability metric because high sinterability leads to large volumetric shrinkage under same conditions [182]. Powder sinterability can also be assessed by the densification ratio,

$$\varphi = \frac{\rho_s - \rho_g}{\rho_{th} - \rho_g} \tag{5}$$

where φ is the densification ratio and ρ_g, ρ_s, and ρ_{th} are the green density, sintered density, and theoretical density, respectively [183]. Theoretical density is calculated based on corresponding crystal structure [184].

2.2.3.3. Powder particle shape

Various particle shapes have been reported in the literature, as shown in Figure 2.4. Spherical particles usually have better flowability. For example, the flow times of spherical and irregular calcium alkaline phosphate powders (45–90 μm, 50 g) are 121 and 166 s under the same conditions, respectively [185], which indicates the better flowability of spherical particles.

There are no reported studies about effects of powder particle shape in ceramic binder jetting. However, effects of particle shape on powder bed density were reported from other fields, such as

geology [186]. Compared with non-spherical powders, sand powder with spherical particle shape could lead to a higher value of powder bed density [186].

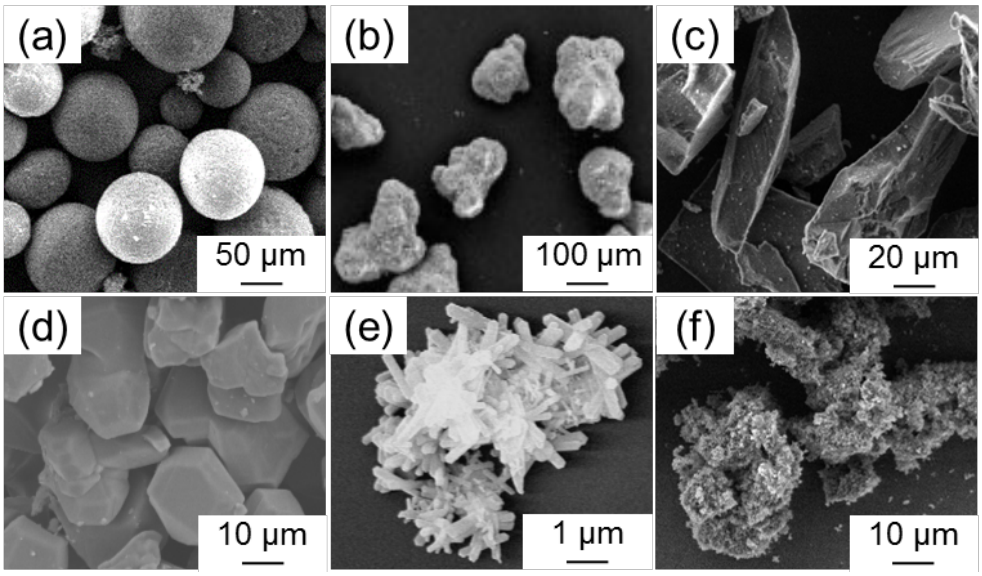

Figure 2.4 Different ceramic particle shapes used in binder jetting: (a) spherical, (b) rounded [176], (c) angular, (d) polygonal [169], (e) irregular [101], (f) aggregate.

2.2.3.4. Powder particle size

Reported particle size of feedstock powder used in ceramic binder jetting ranges from 0.3 (the minimum particle size in [170]) to 355 μm (the maximum particle size in [164]). Particle size of feedstock powder in binder jetting affects powder flowing and sintering behaviors.

Coarse powder usually has good flowability while fine powder often has good sinterability [109]. When particle size is smaller than a certain value, the interparticle cohesion becomes more dominant than the inertia [187]. Therefore, fine particles tend to agglomerate, usually resulting in bimodal pore size distribution in the spread powder layer [145,162,188] and a low powder bed density. Particle size also plays a vital role in powder sinterability. The specific surface area of fine powder is larger than that of coarse powder, leading to a larger sintering driving force and consequently a higher densification after sintering [97]. It is noted that larger particles are desirable

for better flowability while smaller particles are preferred for better sinterability. These two requirements on particle size are contradictory.

Sun et al. reported that the poor flowability of a mixed glass-ceramic powder of a relatively small particle size (< 25 μm) caused powder adhesion onto the roller and thus the movement of the printed layer when spreading a new layer, eventually leading to a significant misalignment between printed layers [97]. In Zocca et al.'s study [96], lithium alumino-silicate glass powder with a median diameter of 75 μm (fine powder) had an *HR* value of 1.29 and the powder with a median diameter of 223 μm (coarse powder) had an *HR* value of 1.11, indicating the better flowability for the coarse powder.

2.2.3.5. Powder deposition methods

In binder jetting, the powder can be deposited with various methods. Figure 2.5 shows four powder deposition methods, where h is desired layer thickness and h_d is pre-deposited thickness. A parameter called compaction ratio, which is the ratio of h_d to h, is used to quantify the compaction level, and a value of two is a common choice [75,167]. The effect of an amount increase of the pre-deposited powder, which induces a higher compaction ratio, has been experimentally studied [57]. It shows that green parts made with more pre-deposited powder have a higher bulk density.

Among all deposition methods, doctor blade spreading is the simplest, with little powder compaction occurring. Other three methods use a roller instead of a blade, and the roller can be fixed [178], forward-rotating [75], or counter-rotating [178]. The counter-rotating roller is the most commonly used. The traversing movement of the roller deposits and compacts the powder, while the rotation smooths the powder bed. Compared with counter-rotating roller, fixed roller and forward-rotating roller have not drawn much interest because of the higher surface roughness of

the spread powder bed [178] and powder bed disturbance by the powder adhering onto the roller surface [75], respectively.

In a numerical study, counter-rotating roller outperforms the doctor blade in achieving high powder bed density and low surface roughness [189]. Combination of different methods, e.g. forward-rotating roller and doctor blade [75] has been reported to increase powder bed density. Parameters of each deposition method can also be tuned to improve powder bed density. For example, Shanjani et al. [190] introduced an analytical model and calculated the powder bed density formed by a counter-rotating roller system. It was found that larger roller diameter leads to denser powder bed. It should be noted that there is no research directly investigating the effect of different powder deposition methods on printed part properties.

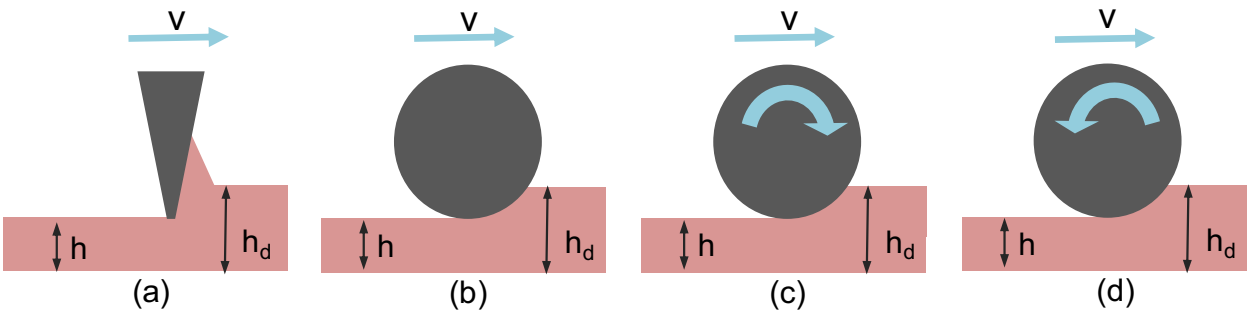

Figure 2.5 Various powder deposition methods: (a) doctor blade, (b) fixed roller, (c) forward-rotating roller, and (d) counter-rotating roller. h is desired layer thickness and h_d is pre-deposited thickness

Though sub-micron and nanometer powders can be easily sintered, it is not easy to spread them due to their high surface energy and thus agglomeration issue [191]. One possible method to address this problem is vibration-assisted spreading. For example, Sachs employed three different methods to vibrate different parts during the printing process, including the build platform, the powder bed surface, and the scraper [20], to spread ceramic powders with a particle size of about

20 μm. A vibrating counter-rotating roller [191], though not used for ceramic materials, is another potential method to break down agglomerates in fine powder with a particle size as small as 100 nm.

2.2.4. Binder

2.2.4.1. Binder material and concentration

Table 2.3 lists binder materials used in reported studies. Organic materials, including polymers (e.g., polyvinyl alcohol) and carbohydrates (e.g., dextrin), are the most common choice for the binder. They have versatility to almost any powder and capability of thermal decomposition with little residue. Phosphoric acid is another common choice, especially for the scaffold parts from the calcium phosphate family. Colloidal silica is used in some cases where the binder is to be incorporated into the final component [18].

Table 2.3 Binder materials used in reported studies

Binder material	Reference
Carbohydrates (dextrin, maltodextrin, starch, etc.)	[38,54,68,71,80,82,85,86,88,95,98,101,105,106,127,142,143,146,147,152,153,155,159,160,163,164]
Phosphoric acid	[85,100,103,109–111,113,115–120,122,123,130,136,138,139,165]
Polymers (polyvinyl alcohol, polyethylene glycol, polyvinylpyrrolidone, etc.)	[23–25,27,38,57,58,64,65,67,69,73,80,93,94,107,108,112,131,140,141,150,154]
Colloidal silica	[6,7,18,20,72]
Acrylic acid	[23,27,79,144]

Binder concentration quantifies the amount of the adhesive material in the binder solution. For a powder-binder system in which chemical reaction happens between them, binder concentration could affect the green density. In Gbureck et al.'s study [117], tricalcium phosphate

($Ca_3(PO_4)_2$) part was printed with various phosphoric acid binder concentrations (5, 10, 20, and 30 wt.%) and the green density was measured. Results show that the increase of binder concentration led to an improvement of the binder-powder reaction between tricalcium phosphate and the phosphoric acid forming dicalcium hydrogen phosphate ($CaHPO_4{\cdot}2H_2O$) and dicalcium pyrophosphate ($Ca_2P_2O_7$) as cement materials for the part [100,123,192]. They observed a downward trend of the green porosity. It should be noted that for a powder-binder system in which binder only bonds the particles together and does not involve any chemical reaction, binder concentration does not significantly affect the part density as the binder will be burnt off during debinding.

2.2.4.2. Binder application methods

Figure 2.6 illustrates two different methods of binder application. The first method, called binder jetting in-place, is to add the binder material to the printing solution and then jet the binder solution onto the powder bed [6,109,157,170]. The second is to pre-mix powder and binder by either a dry [107,108,160] or wet [85,140,155] approach and use the powder-binder mixture as the feedstock material. For dry mixing, the ceramic and binder materials are pre-mixed using a grinder, ball mill, or pestle and mortar. For wet mixing, the binder material is dissolved in a solvent (e.g., water), and the ceramic material is added to obtain mixture slurry. Then the slurry is spray-dried [35,68,99,100,124,126,127,136,140,144,146,147,149–152,155] or freeze-dried [63,70,71,80,85,87,88] and sieved. For both dry and wet mixing, the binder within the powder feedstock joins the ceramic particles wherever the printing liquid (usually a water-based solution) is jetted.

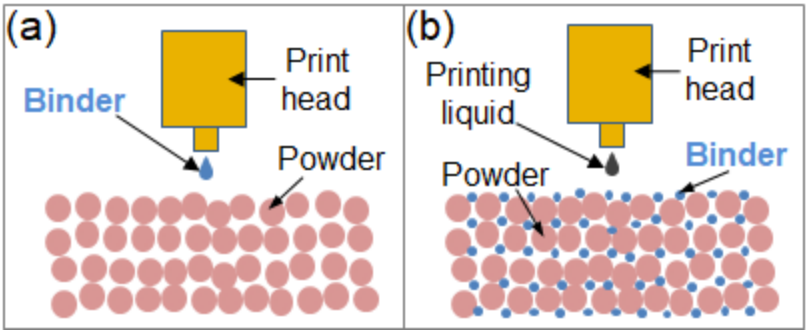

Figure 2.6 Two methods of applying binder: (a) binder jetting in-place; (b) powder-binder pre-mixing

Figure 2.7 shows shares of each of the binder application methods in the reported studies. Binder jetting in-place method is less complicated than the other two due to fewer feedstock preparation steps, and has the most shares in the reported studies. The powder-binder pre-mixing method allows for the use of a low-viscosity printing liquid because the binder is supplied in the powder feedstock, which decreases the possibility of nozzle clogging. Wet pre-mixing can be more advantageous than dry pre-mixing because the binder is more evenly mixed with the ceramic material.

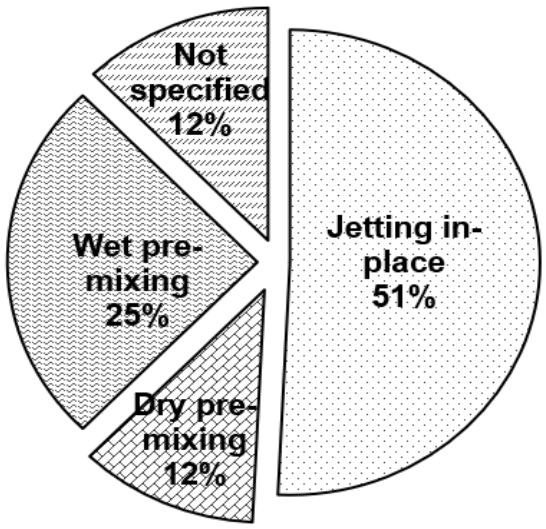

Figure 2.7 Shares of different binder application methods in reported studies

2.2.5. Process parameters

2.2.5.1. Layer thickness

Layer thickness directly affects the time needed to print a part and the surface roughness of the part. A smaller layer thickness can lead to smoother surface but a longer printing time, and vice versa [100]. The particle size is an important parameter to consider for selecting layer thickness. For binder jetting, there are no universally accepted rules for selecting layer thickness. Rules reported in the literature include at least greater than the largest particle size [75,162,193], twice the particle size [194], and at least three times the particle size [110,177].

Some studies have been reported about the effects of layer thickness on various material properties. Meier et al. employed a discrete element method (DEM) model that considered particle-to-particle and particle-to-wall interactions involving frictional contact, rolling resistance, and adhesive forces [195]. It was found that the powder bed density increased with increasing layer thickness. Some other studies found different effects of layer thickness on printed part density. For example, Shanjani et al. introduced an analytical model to predict the powder bed density under various layer thickness values [190]. The model was based on the mechanics of plastic strains of a volume-compressible continuum [196]. They found that an increase of layer thickness led to a decrease of the powder bed density.

2.2.5.2. Binder saturation

Binder saturation, S_b, quantifies the amount of the binder solution applied during the printing process. It is defined as the percentage of air space (in the powder bed) that is filled with binder solution, given by the following equations,

$$S_b = \frac{V_b}{V_a} \tag{6}$$

$$V_a = \left(1 - \rho_p'\right) \times V_e \tag{7}$$

where V_b is the volume of the binder applied to a pre-defined envelope, V_a is the air space volume of the powder bed within the same envelope before jetting binder, ρ_p' is the relative

packing density of the powder bed, and V_e the volume of the pre-defined envelope. It should be noted that the value of binder saturation may exceed one hundred percent because the binder in the previous layers can dry out and therefore more binder than the presumed total free volume can be jetted to the powder [96].

A low binder saturation level leads to limited contact between powder and binder, and results in fragile green parts. In contrast, a high binder saturation level causes the binder to spread out of the selected area, which is called bleeding, compromising the dimensional accuracy and surface smoothness of printed parts [176]. Effect of binder saturation on the sintered density was studied in Sun et al.'s study. A continuously decreasing trend of the sintered bulk density from 66.5% to 55.9% on titanium silicon carbide was reported with the increase in the saturation level of a commercial binder from 10% to 30% [89], which may be due to the increased surface roughness resulted from binder bleeding and thus larger apparent porosity. Melcher et al. found that the bulk density of sintered alumina parts from granulated powder (granule size of <150 μm) increased from 56% to 67% with the increase of the binder saturation of a water-based commercial binder from 0.14 g/cm^3 to 0.35 g/cm^3 [63]. It might be due to stronger particle bonding and thus denser green part after printing with the higher binder saturation.

2.3. Terminologies, Measurement Methods, and Achieved values for Density and Porosity

2.3.1. Definition of various terminologies

Density and porosity are the most commonly assessed material properties in ceramic binder jetting. There are many terminologies related to density and porosity, dependent on what packing state the powder is in, what processing stage the part has gone through, and what pores are included in the calculation. The definitions are not always made clear in published reports. These terminologies and their definitions are summarized in Table 2.4.

Table 2.4 Terminologies for density and porosity

Category	Terminology	Definition	Reference
Powder density in different packing states	Apparent density	Density of freely settled powder	[96,97,109,145]
	Tap density	Density of powder after standard tapping process	[96,97,145,152]
	Powder bed (packing) density	Density of powder that is spread on the build platform	[23–25,63,80,93,98,145,169,171]
Part density after different process stages	Green density	Density after printing	[23,25,80,88,98,108,117,141,152]
	Brown density	Density after debinding	[197]
	Sintered density	Density after sintering	[63,70,71,78,85,87,95,96,101,102,106,132–134,136,142,144,171]
Part density and porosity when different pores are included	Apparent solid density	Mass per unit apparent solid volume (total volume of solid material and closed pores)	[68,147,166,167]
	Bulk density	Mass per unit bulk volume (total volume of the solid material, open pores, and closed pores)	[97,125,132,133,155,159]
	Apparent porosity	Volume percentage of open pores in the bulk material	[63,84,96,97,104,108,117,121,122,131,141,147,152,154,158,161,164,172]
	Closed porosity	Volume percentage of closed pores in the bulk material	[125,132,133,135]
	Bulk porosity	The sum of apparent and closed porosity	[83,87,157,95,99,102,114–116,124,142]

2.3.1.1. Powder density in different packing states

There are three terminologies to define the powder density depending on different packing states: apparent density, tap density, and powder bed density. Apparent density is the density of freely settled powder [198–201]. Tap density is the density of a powder that has been tapped, to settle contents, in a container under specified conditions [179,180]. Powder bed density is the

density of the powder that is spread on the build platform. Unlike apparent density and tap density that can be measured by following standards [179,180,198–201], powder bed density can be measured by various methods. A common method is to spread a number (e.g., 50) of layers of powder and then measure the bulk volume and the mass of the powder [63,75,167]. Another method is to print multiple cylindrical cups and then measure the cup size and weight change after depowdering [202]. For a given powder, powder bed density is usually between those of apparent and tap densities.

2.3.1.2. Part density after different process stages

Green density, brown density, and sintered density are the part densities that just after printing, debinding, and sintering, respectively. Green and sintered densities have been vastly investigated while brown density has been rarely reported for the friability of the debound part and thus the difficulty of density measurement. Other densities can be obtained if additional post-processing steps are applied. For example, infiltrated density can be measured if infiltration is performed [69,82,85,88,155,159] and pressed density can be obtained if isostatic pressing is implemented [64,90,93].

Relative density (ρ') is the ratio of absolute density (ρ) to theoretical density (ρ_{th}):

$$\rho' = \frac{\rho}{\rho_{th}} \tag{8}$$

where theoretical density (ρ_{th}) is calculated based on crystal structure and unit cell dimensions. In this paper, relative densities are used since they can be readily compared across various materials.

2.3.1.3. Part density and porosity including different pores

For a part with both open and closed pores, its volume measurement is complicated. Figure 2.8 schematically shows these pores in a part. Open pores are permeable from a surface while

closed pores are not. The bulk volume of the part includes volumes of solid as well as both open and closed pores, while the apparent solid volume includes volumes of solid as well as closed pores. The only difference between these two volumes is that the bulk volume includes open pores but the apparent solid volume does not. Accordingly, the bulk density is the mass per unit bulk volume while the apparent solid density is the mass per unit apparent solid volume. Similarly, apparent porosity [203], closed porosity, and bulk porosity are the fractions of the volumes of open pores, closed pores, and both of them, respectively, in the bulk volume. The bulk porosity (π_b), apparent porosity (π_a), and closed porosity (π_c) can be estimated from the relative apparent solid density (ρ'_{as}) and relative bulk density (ρ'_b) based on the following equations

$$\pi_b = 1 - \rho'_b \tag{9}$$

$$\pi_a = 1 - \frac{\rho'_b}{\rho'_{as}} \tag{10}$$

$$\pi_c = \frac{\rho'_b(1 - \rho'_{as})}{\rho'_{as}} \tag{11}$$

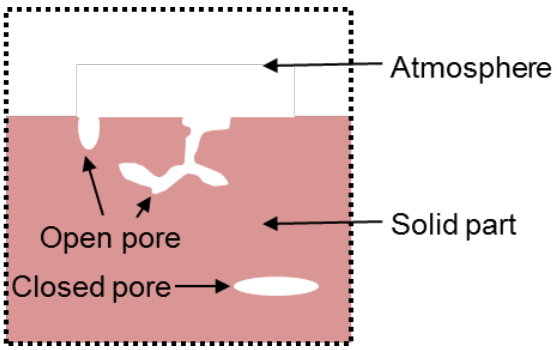

Figure 2.8 Open and closed pores in a cross section of a part

The methods for part density and porosity measurement are listed in Table 2.5. The geometry method works for a part with a simple shape (e.g., cuboid and cylinder). The simple Archimedes' method measures two kinds of sample masses: dry mass and immersed mass in water (to calculate the immersed volume). Usually, water is infiltrated into the open pores. The immersed volume is

the apparent solid volume. Therefore, the simple Archimedes' method only measures the apparent solid density. Compared with that, a full water absorption into the open pores is induced in the modified Archimedes' method by boiling [203,204] or vacuuming [203,205,206], after which immersed mass and soaked mass (in addition to dry mass) are measured to evaluate the open pore volume [203]. Therefore, this method is capable to simultaneously measure apparent solid and bulk densities.

In the mercury intrusion method, mercury as a non-wetting liquid is used, and does not enter open pores unless under pressure. The volume of the pores is determined from the mercury volume intruded at each pressure increment [207]. Gas pycnometer has a similar principle with that of simple Archimedes' method but with a displacement medium of gas (e.g., helium), which is suitable for physically or chemically sensitive materials [208] or for small pores. Computed tomography is a non-destructive method which uses X-ray and mathematical algorithm to generate cross section images of the part [209]. From these cross section images, the volume can be determined. Image analysis method uses 2D images of the sample cross section and quantifies the porosity [167].

Table 2.5 The capabilities of different measurement methods

Method	Bulk density	Apparent solid density	Bulk porosity	Apparent porosity	Closed porosity	References
Geometry	Yes	No	Yes	No	No	[94,111,125,132,133,137,144,155,159]
Simple Archimedes'	No	Yes	No	No	No	[68,94,97,165–167]
Modified Archimedes'	Yes	Yes	Yes	Yes	Yes	[38,69,83,86–88,95,96,101,102,107,108,129,135,146,147,152,154,168]
Mercury intrusion	Yes	Yes	Yes	Yes	Yes	[23,63,70,71,106,141,153,160]
Gas pycnometer	No	Yes	No	No	No	[82,104,137,144]
Computed tomography	Yes	Yes	Yes	Yes	Yes	[139,142,157,158]
Image analysis	Yes	Yes	Yes	Yes	Yes	[167]

2.3.2. Achieved part density in reported studies

As relative densities and porosities can be readily compared across different materials, all absolute values have been transformed to relative values based on Equation (8). Theoretical density values are shown in Table 2.6. It should be noted that only materials whose density values were reported in absolute values are shown in this table.

Table 2.6 Theoretical density values of different materials

Material	Theoretical density (g/cm^3)	Reference
Al_2O_3	3.97	[210]
AlN	3.25	[210]
$BaTiO_3$	6.02	[210]
$CaSO_4$	2.32	[211]
SiC	3.22	[210]
TiC	4.91	[210]
$TiAl_3$	3.40	[212]

Figures 2.9 and 2.10 show the achieved relative densities and porosities of the green and sintered parts. Different densities and porosities are interpreted by the reported terminologies and measurement methods in the corresponding papers. Special treatment techniques are used to categorize all values. Specific data values of Figures 1.9 and 1.10 and the corresponding references are shown in Appendixes A and B, respectively. It should be noted that besides these 54 density and porosity values from 41 publications, there are some unclear values because of the lack of specific description of the measurement method, or non-standard metrics (e.g., porosity derived from apparent solid density).

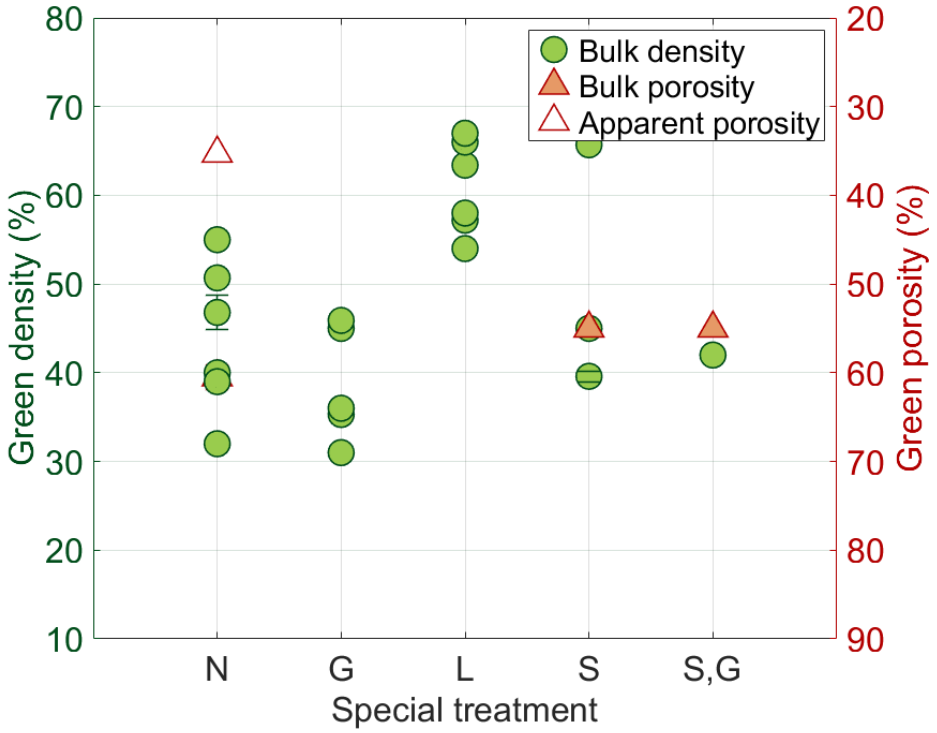

Figure 2.9 Achieved values of relative green densities and porosities by various special treatment techniques (N stands for no special treatment, G for powder granulation, L for using slurry feedstock, S for mixing powders of different sizes) [23–25,27,38,55,57,58,63,64,67,68,73,74,81,82,86–88,91,108,153,158]

Green bulk density determines the sintered bulk density and thus other material properties. A slurry feedstock usually leads to a green bulk density of higher than 50%. Using a slurry with a 35 vol.% alumina (0.5 µm), a green bulk density of 67% was achieved in the study by Grau et al. [24], which is the highest in the literature. Mixing powders of different size is another commonly used method to improve green density. Kunchala et al. [58] introduced alumina nanoparticles (less than 50 nm) to the binder and printed alumina powder feedstock with an average size of 40 µm. A green bulk density of 65.7% was obtained when the nanoparticle concentration in the binder was 15 wt.%.

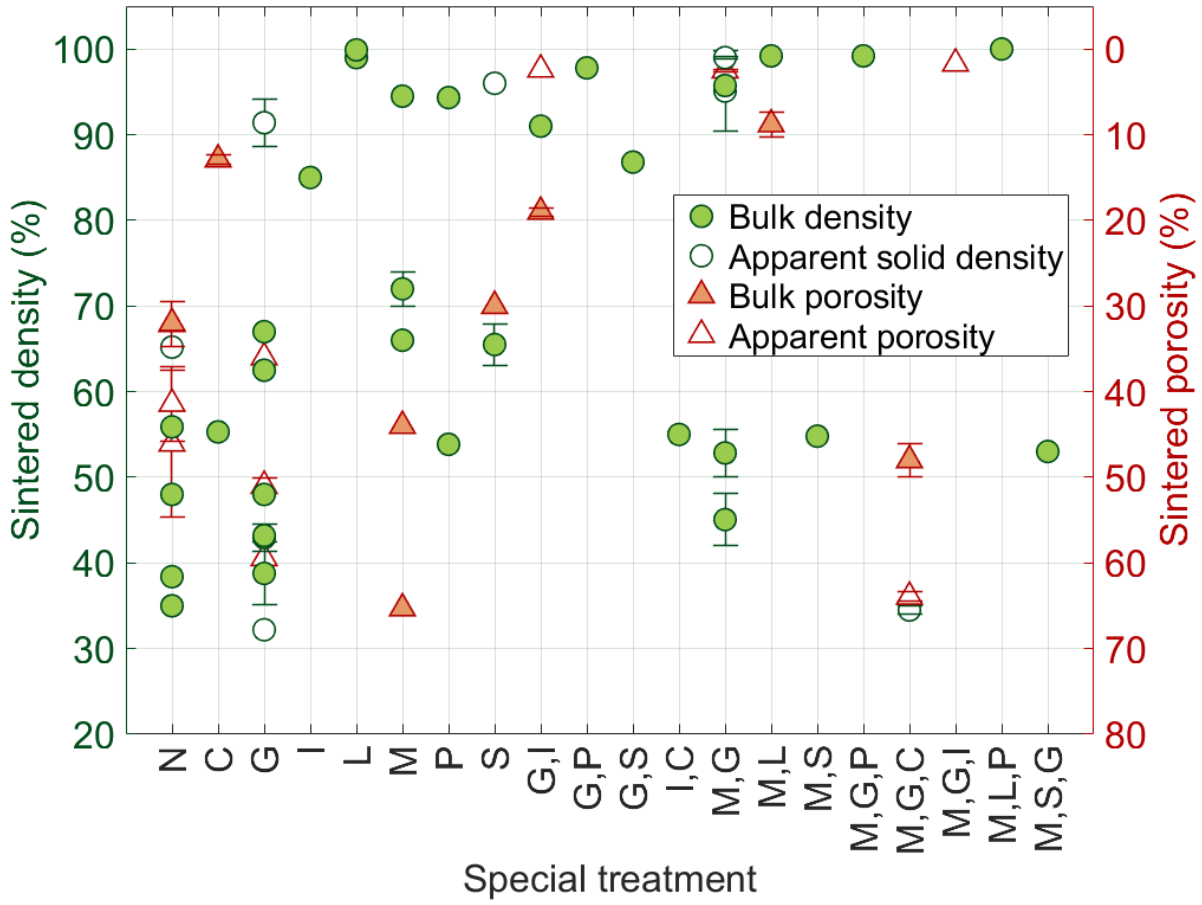

Figure 2.10 Achieved values of relative sintered densities and porosities by various special treatment techniques (N stands for no special treatment, C for chemical reaction, G for powder granulation, I for infiltration, L for using slurry feedstock, M for mixing different materials, P for pressing, and S for mixing powders of different sizes) [24,27,69–71,77,83,85,86,88,89,91,38,93–97,99,101,102,106,107,53,108,124,125,129,132,133,135,142,144,147,54,152–155,166,167,171,55,63–65,68]

Sintered bulk density directly determines other material properties. Therefore, it is mostly reported in the literature. A high sintered bulk density (>90%) was achieved in some studies by applying slurry feedstock [24,27,38,93], infiltration [86], or isostatic pressing [64,89,93]. Slurry feedstock is among the most effective techniques. In Cima et al's study [27], parts printed with alumina slurry achieved a green bulk density of 58% and a sintered bulk density of 99.9%. Combinations of special treatments can lead to high sintered bulk density as well. Specifically,

Kernan et al. [93] studied the printing of tungsten carbide with an average particle size of 0.8 μm, in which a combination of mixing different materials (tungsten carbide and cobalt), slurry feedstock (25 vol.% water-based slurry) and hot isostatic pressing (5.5 MPa during sintering) was applied and the achieved sintered bulk density was 100%. A bulk density of 99.2% was achieved by using an alumina slurry feedstock (0.5 μm, 34 vol.%) in combination with applying sintering additives in Zocca et al's study [38]. Bulk density of the printed alumina part increased from 34% to 61% by warm isostatic pressing in Yoo et al's study [64], leading to a sintered bulk density of 99.2% (with the additional help of sintering additive and powder granulation).

2.4. Material Preparation Techniques for Density Improvement

2.4.1. Powder granulation

The contradiction between the flowability and the sinterability of feedstock powder is among the main challenges in the field of ceramic binder jetting. Generally, the particle size used in binder jetting is in the range of 10–100 μm to ensure a good flowability and avoid defects in powder bed layers. At the same time, the particle size should be less than 1 μm to ensure a high sinterability and thus a dense part after sintering [64]. However, the flowability of fine powder (less than 1 μm) is usually not high enough to form a uniform and smooth layer of powder bed due to its high interparticle cohesion [178,213]. Fine powder spreading usually creates pores and cracks on powder bed, which are consequently inherited by the green and sintered parts. Therefore, increasing the flowability of fine powder is highly beneficial to fabricate dense parts with a minimal number of pores.

One common technique to increase powder flowability is granulation [214]. Granulated powder can significantly improve the flowability of feedstock powder. The fine raw particles ensures the required sinterability and the coarse resultant granules ensures the required flowability.

Its principle is schematized in Figure 2.11. Basically, raw (fine) particles are bonded by a binder to form larger aggregates (or granules). Steps for granulation include mixing, drying, comminuting, and sieving, as shown in Figure 2.12 and listed in Table 2.7. A ball mill, grinder, or pestle and mortar can be used to mix raw particles with a binder solution to form a slurry, which can be dried by a spray dryer, freeze dryer, or oven. Comminuting step is not needed for the powder from a spray dryer because the size is determined by sprayed droplets. For the cakes dried by a freeze dryer or an oven, comminuting step is needed to decrease the size by ball milling, grinding, or manual crushing. Then a sieving step screens the powder into several groups with different size ranges. Generally, the manual granulation method, comprising of manual mixing in a crucible, oven drying, manual crushing in a crucible, and finally sieving, is simple, although the granule shape is irregular. Commercial granulation machines based on spray drying technologies, though costly, can produce spherical and large-batch granulated powder.

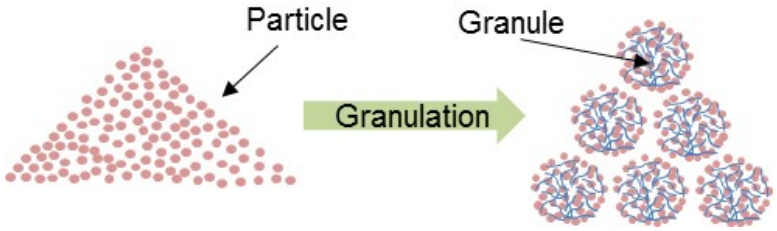

Figure 2.11 Principle of granulation

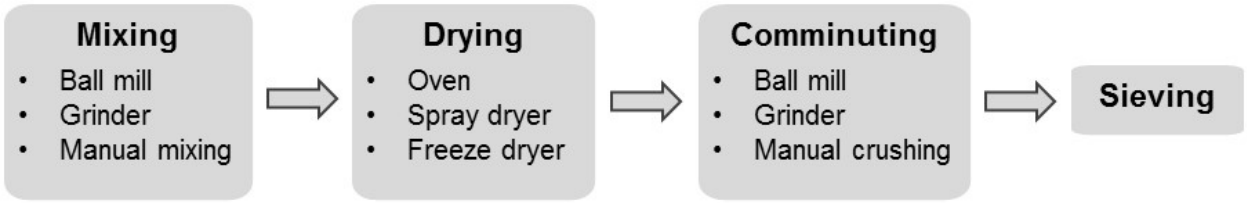

Figure 2.12 Basic granulation steps

Table 2.7 Granulation process practiced in reported studies

Granulation process	Reference
Dry mixed, dry ball milled	[86]
Dry mixed, sieved	[80]
Wet mixed, (wet ball milled), spray dried	[68,99,100,124,135,140,144,146,147,150,152,155]
Wet mixed, (wet ball milled), oven dried, dry ball milled	[78,125,132–134]
Wet mixed, (wet ball milled), freeze dried, dry ball milled, sieved	[63,70,71,85,87,88,94]
Commercial spray-dried powder	[35,126,149,151]

Chumnanklang et al. [147] investigated the effect of binder fraction on the flowability of spray-dried hydroxyapatite powder. The powder flow rate increased from 14.6 to 21.2 g/s when binder fraction decreased from 48.3 to 15.7 vol.%. Gildenhaar et al. prepared spray-dried calcium alkaline phosphate powder with various raw particle sizes [185]. They found that printed parts made with granules from fine raw powder (3.1 μm) had a higher compressive strength (2.5 MPa) than those from coarse raw powder (7.5 μm, 1.80 MPa).

With the same raw powder, different granulation technologies can result in different material properties. Suwanprateeb et al. [152] studied two granulation technologies, manual granulation with mortar and pestle, and spray drying. After printing and sintering at 1300 °C, samples made with manually granulated hydroxyapatite powder showed ~20% higher bulk density and approximately two times higher flexural modulus and strength than those made from spray-dried powder. One of the reasons is the larger number of inter-granule pores from the spray-dried powder than the manually granulated powder, leading to a lower green density. Another possible reason is the large pores within the spray-dried granules, which are formed due to the solvent evaporation during the drying process [215].

These two issues of spray-dried granules can potentially be resolved by another granulation technique called spray freeze drying [216–218]. The granules from spray freeze drying can be soft, making the particles loosely bonded and easily breakable. The granules can be crushed by externally exerted forces such as the roller compaction force. Therefore, the granules retain a microscale size before spreading and facture to a nanoscale size after compaction. The other feature of the granules from spray freeze drying is its homogeneous structure. No large pores are formed inside a granule after drying as the sprayed droplet is frozen first and the drying process is solvent sublimation instead of evaporation [216].

2.4.2. Mixing powders with different sizes

Particle size distribution plays a key role in powder packing, which can be either monomodal or multimodal. Since fine particles can fill voids between coarse particles, powder with a multimodal size distribution has less interparticle voids. From this point of view, mixing powders of different sizes can be an effective technique to increase powder bed density and consequently green density of printed parts [65]. Moreover, this technique could also reduce sintered shrinkage as there are less voids in the green part. This is beneficial for improving the dimensional accuracy after sintering.

Table 2.8 lists studies on mixing powders of different sizes for feedstock preparation. For example, Sun et al. studied the effects of powder mixing on powder flowability, part sintered density, and part bending strength [97]. Glass-ceramic powders with three size ranges were mixed in various fractions. The mixture with 60 wt.% 45–100 μm and 40 wt.% 0–25 μm particles achieved the highest sintered bulk density of 1.6 g/cm^3 and bending strength of 13.8 MPa. In Spath et al.'s experiment, parts made from mixed hydroxyapatite powder had a higher compressive strength than those from the two constituent powders [146].

Instead of finding the optimal ratio by trial and error, a promising direction is model-guided selection of particle size and mixing ratio of constituent powders. In the study by Du et al. [65], packing densities with various mixing ratios were predicted using the linear packing model [219]. Optimal mixing ratios to achieve the highest packing density were selected for both binary and ternary mixtures. The printed parts from optimal ternary ratios achieved the largest sintered bulk density. Although the improvement is small due to the decreased flowability, the study showed that the linear packing model has a potential to guide the selection of the particle size and mixing ratio.

Table 2.8 Parameters of powder mixing technique in reported studies

Material	Size (μm)	Mixing Ratio	Reference
Al_2O_3	2, 10, 70	17.6:21.1:61.3	[65]
Al_2O_3	30, 45, 53	1:1:1	[166]
Al_2O_3	20, 3.4, 0.4	63:27:10	[67]
Al_2O_3 and Al	0.6, 3	25:100, 30:100, 35:100, 40:100, 50:100	[54]
$Ca_3(PO_4)_2$ and bio-glass	8, 38	1:3, 1:1	[99]
$Ca_5(PO_4)_3(OH)$	38, 125	15:85, 25:75, 35:65	[146]
$Ca_5(PO_4)_3(OH)$	4, 50	15:85, 25:75, 40:60, 60:40, 75:25, 100:0	[153]
Glass-ceramic compound	0–25, 25–45, 45–100	0:100, 10:90, 20:80, 30:70, 40:60, 100:0	[97]

Another method to mix powders of different sizes is to introduce nanoparticles of the same material during printing [58,94]. These nanoparticles can enhance the sintering performance due to their high activity. For example, Zhang et al. demonstrated the feasibility of using 10 wt.% zirconia nanoparticle suspension as the printing liquid while printing zirconia parts [94]. The

printed and sintered bulk density increased from 75.2% to 86.8% as the binder saturation increased from 50% to 120%.

2.4.3. Slurry feedstock

Structural ceramic parts usually require fine-grained powder (submicron) and high green density (>50%) to achieve a full density after sintering [24]. However, it is difficult to meet these requirements simultaneously using dry powder feedstock. Due to its low packing density and agglomeration issues, dry fine powder feedstock generally results in parts with low green density and defects.

Slurry feedstock was used to meet both requirements of fine powder and high green density [24–31,38,77,81,93]. In this technique, a layer of ceramic slurry is deposited and then dried to form the powder bed [26]. Two slurry deposition methods have been reported in the literature. The first one is nozzle jetting [23–25,27,93,173] that was studied by the inventors of binder jetting. In this case, a thin slurry layer is deposited by a single nozzle scanning over a porous substrate [25]. The second deposition method is doctor blade spreading that was studied by Zocca et al. [38,81] and Lima et al. [77]. In both deposition methods, the layer top is dried by a heating lamp, while the bottom was dried due to capillary forces from the porous substrate or previously deposited and dried layers [24,220]. Delicate temperature and ventilation control is needed to achieve crack-free powder bed layers.

Compared with the dry powder deposition method, the slurry-based method can handle submicron particle size (down to 0.5 μm). It can achieve high powder bed density (up to 53% in Kernan et al.'s study [93]) and high green part bulk density (up to 67% in Grau et al.'s study [24]). Different materials (i.e., alumina [24,25,27,38,77], silicon nitride [24,25], silicon carbide [81], silica [173], and tungsten carbide with cobalt [93]) have been investigated with this method. In

Zocca et al's study [39], printed parts from an alumina slurry (solid loading of 34 vol.% and average particle size of 0.5 μm) achieved near theoretical density (i.e., bulk density of 99.2%) after sintering at 1600 °C with the help of sintering additives.

Maximum layer thickness, i.e. critical saturation thickness (CST) [30], exists for slurry feedstock technique. A layer thickness larger than the CST leads to cracking or warping of the powder bed due to capillary pressure of solvent evaporation [24,26,30]. Furthermore, thick parts are prone to crack and difficult to be fully dried [49].

It should be noted that slurry feedstock has been extensively used in other ceramic AM technologies such as vat photopolymerization and material extrusion. For example, Hu et al. prepared a 60 vol.% alumina slurry (average size of 138 nm) [221] for vat photopolymerization. After printing and sintering at 1650 °C for 2 h, the part achieved a bulk density of 3.96 g/cm^3 (99.7% in relative). Mamatha et al. [222] used a slurry with a solid loading of 64.75 wt.% of alumina powder (average size of 331 nm) in material extrusion. After printing and sintering at 1650 °C for 1 h, the part achieved a bulk density of 97.7%. Therefore, application of slurry feedstock in binder jetting can be advanced by learning from other AM technologies.

2.4.4. Mixing different materials

Mixing different materials is a common technique to increase printed and sintered density [77,91,95–97,99,101,104,106,117,120,121,135–137,139,141,142,144,171].. The mechanisms for density enhancement could be boosting the mass transport [38,74,132–135] or enabling liquid phase sintering [223]. In Bose et al.'s study, tricalcium phosphate powder was mixed with 0.5 wt.% MaO and 0.5 wt.% SiO_2. The part achieved a bulk porosity of 50.21% after sintering at 1250 °C, compared with that of 54.11% from pure tricalcium phosphate powder [134]. Yoo et al. doped alumina (mean particle size of 0.8 μm) with MgO and granulated both undoped and doped powders

to a granule size range of 70–150 μm [64]. The printed and sintered parts from doped alumina achieved a higher relative sintered bulk density (99.2%) and flexural strength (324 MPa) than the undoped powder (97.8% and 231.6 MPa) after printing, isostatic pressing, and sintering.

Although this mixing technique is fairly effective, other material properties (e.g., biocompatibility) may be impaired. The limited choice of additive materials is another of the drawbacks of this technique. Moreover, the additive particles may not be homogenously distributed within the ceramic powder, leading to structure heterogeneity (i.e., local variation) in the sintered part [52,210]. In addition, the selection of additives has remained largely empirical as the mechanism of the sintering additive has not been fully understood [210]. Therefore, this technique only works for specific materials.

2.5. Post-processing Techniques for Density Improvement

2.5.1. Sintering

Sintering is the process by which a powder compact is transformed to a dense body by heating [224]. It's the most commonly used method to increase the density. Sometimes it is considered an essential part of the process and not considered a separate post-processing method. The macroscopic driving force in sintering is the reduction in surface energy. The densification during sintering happens by the elimination of solid/vapor interfaces [224]. However, sintering is not required in some cases, for example, when porous parts are preferred or other post-processing techniques are applied.

One of the important sintering parameters is the sintering temperature. Sintering temperature significantly affects the material properties as it determines the mass transport of the ceramic particles. Typically, a higher sintering temperature can facilitate mass transport and subsequently increase part density and decrease porosity [53]. Another parameter that significantly affects the

sintered density is the green density. To present the effect of green density on sintered density, the bulk densities before and after sintering are shown in Figure 2.13. Powder bed density is also included as it is close to green density. As some parts were isostatically pressed before sintering [64], their pressed green densities are presented instead of printed green densities. Specific data values of Figure 2.13 and the corresponding references are shown in Appendix C. Generally, high green density leads to high sintered density. A high green density (i.e., >50%) is required to achieve a high sintered density (i.e., >90%).

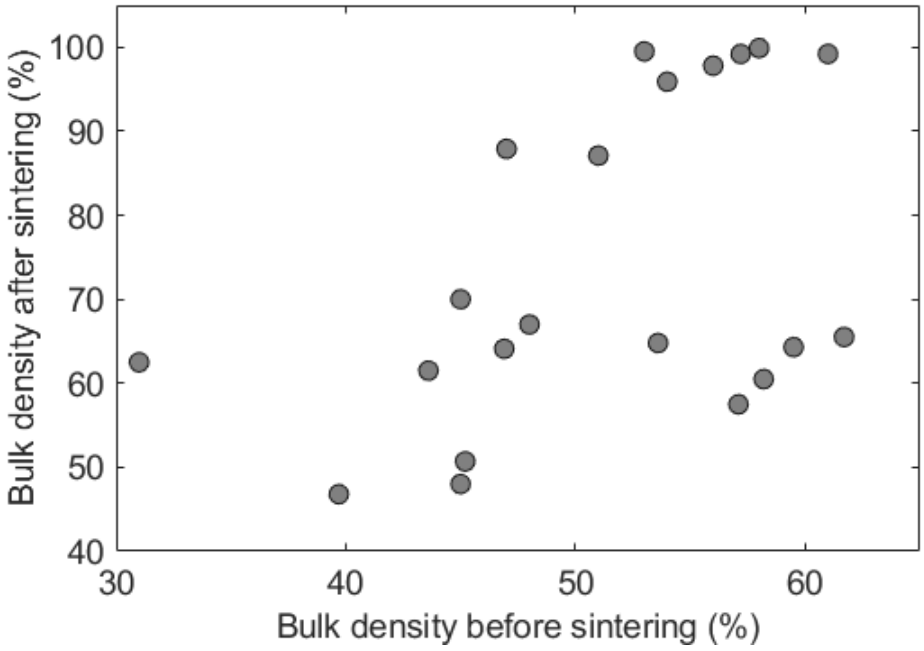

Figure 2.13 Bulk densities before and after sintering [24,27,38,55,63–65,68,83,93,153]

Shrinkage is a critical index to determine the density change by sintering. For parts with the same green density, a larger shrinkage leads to a higher sintered density. A primary factor that affects shrinkage is sinterability, which is directly related to particle size [52]. For example, Du et al. [65] used alumina powder with an average particle size of 10 μm and achieved a powder bed density of 57.1%. Using 0.5 μm alumina powder, Zocca et al. [38] achieved a green density of 57.2%. As there is no significant density change for the powder bed after printing, it can be assumed that green parts from Du et al.'s and Zocca et al.'s studies have approximately the same

green densities. After sintering at 1600 °C, parts made from coarse powder (10 μm alumina in Du et al.'s study) achieved only 0.7% volumetric shrinkage, leading to a bulk density of 57.7%. However, parts from fine alumina powder (0.5 μm in Zocca et al.'s study) achieved a volumetric shrinkage of 73.4% and bulk density of 99.2%.

It should be noted that sintering could also result in shape distortion due to gravity effect, non-uniform temperature gradient, liquid phase formation due to high sintering temperature, etc. [225]. For example, Grant et al. [226] studied the distortion of a hanging beam at different sintering stages. It was found that most of the distortion happened above 1180 °C. To mitigate the distortion, they introduced a reactive binder. During sintering, it decomposed to form titanium dioxide nanoparticles through hydrothermal reactions, which formed interparticle necks and mitigated the distortion [226].

2.5.2. Chemical Reaction

Chemical reaction is another common method to increase green and sintered densities in ceramic binder jetting, which includes metal oxidation [53,54,79,84], phosphoric acid immersion for calcium phosphate materials [111,114,160,116,117,119,120,122,123,139,159], and pyrolysis of preceramic polymers [83,102]. Metal oxidation uses a metal powder as the feedstock material and convert a printed metal part to a ceramic one by oxidation at a high temperature. Phosphoric acid immersion uses this acid solution to immerse calcium phosphate parts, which are printed with a binder of phosphoric acid solution. The immersion leads to a further reaction of unreacted material and thus a cemented structure. Pyrolysis of preceramic polymer uses polymeric precursor as the feedstock and ceramize the printed part at a high te17mperature. For example, Zocca et al. [83] investigated the possibility of using silicone (polymethylsilsesquioxane) as a preceramic polymer. A bulk density of 87.1% for the ceramized SiOC part was achieved after sintering at

1200 °C for 1 h. It should be noted that chemical reaction technique only works for certain material systems. Specifically, the ceramization reaction in the preceramic polymer pyrolysis technique involves a significant mass transport of the reagents and/or the by-products. Therefore, part size is limited with this technique.

2.5.3. Infiltration

Infiltration is another common method to increase the part density. Both a different material [71,85,88,159] and the same material [69] have been investigated to infiltrate parts from binder jetting. The most common infiltration method is melt infiltration [39,63,70,71,80,82,85–88,159,169]. In the study of Nan et al. [85], the printed and sintered TiC parts were infiltrated in melted silicon at 1600–1700 °C for 1 h and annealed at 1400 °C for 2 h, which produced Ti_3SiC_2 (about 45 vol.%), $TiSi_2$ (about 21 vol.%), and SiC. Infiltration with a different material changes the composition of a part and the resultant phases might be difficult to control sometimes.

Solution infiltration can be used for infiltrating a part with the same material, in which fine powder is mixed with a solvent and the part is immersed in it. The most critical parameter for this infiltration method is solid loading. For example, Maleksaeedi et al. [69] printed and pre-sintered alumina parts at 1000 °C for 2 h, infiltrated them in alumina slurries of different solid loadings, and post-sintered them at 1650 °C for 2 h. As the solid loading increased from 0 (no infiltration) to 50%, the bulk density of the final parts increased from 38% to 85%. Cross sections of the infiltrated parts after post-sintering are schematically shown in Figure 2.14. The infiltration depth for parts with the same shape and size decreased along the increase of solid loading. A non-infiltrated core remained in the parts treated with a slurry of a high solid loading.

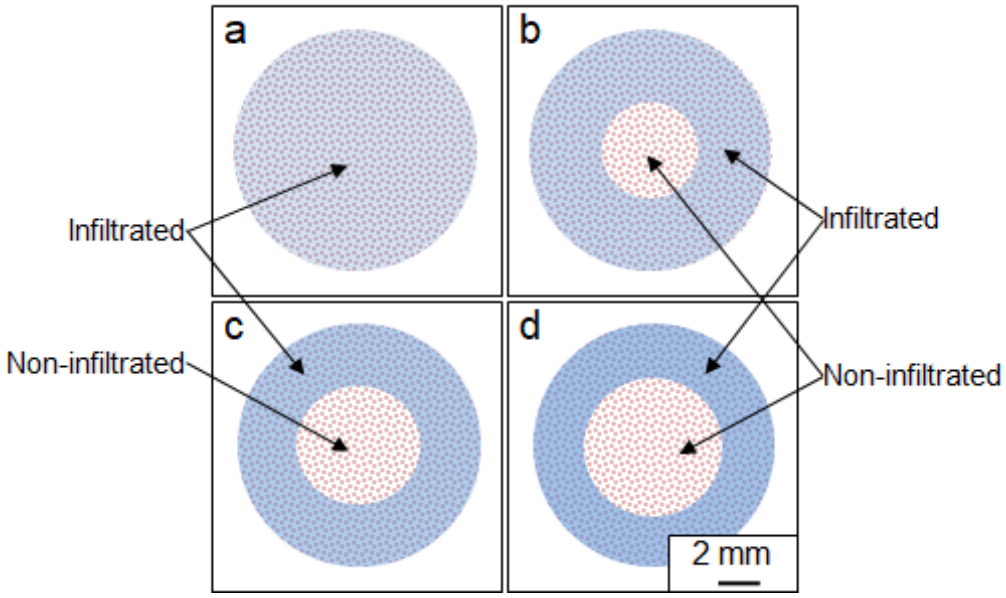

Figure 2.14 Schematic pictures of the cross sections under various infiltrate solid loadings: (a) 35%, (b) 40%, (c) 45%, (d) 50% [69]

2.5.4. Isostatic pressing

Isostatic pressing is a traditional powder metallurgy process that applies equal pressure in all directions on a powder compact, thus achieving uniform density and microstructure [210,227], The pressing medium that exerts equal pressure can be water, oil, and gas. Based on the operation temperature, this technique is classified as cold isostatic pressing (CIP), warm isostatic pressing (WIP), and hot isostatic pressing (HIP) [227,228]. CIP can consolidate green parts under room temperature to obtain higher green density ready for sintering. WIP operates at intermediate temperatures from 80 °C to 450 °C [228], which is suitable for parts requiring a heat-induced chemical reaction [227]. HIP heats and presses the part under gas medium (e.g., argon) with an accurate control of both temperature (up to 2000 °C) and pressure (50–200 MPa) [227]. It usually requires longer processing time than CIP and WIP.

All three kinds of isostatic pressing techniques have been utilized in ceramic binder jetting. For example, Sun et al. used cold isostatic pressing (CIP) method to consolidate green Ti_3SiC_2 bodies [89], which led to an increased sintered bulk density of 94.3% compared with 65.5%

without CIP. In Yoo et al's study, both CIP and WIP were utilized to densify alumina green parts. The bulk density increased from 36% to 54% after CIP and 34% to 61% after WIP, which resulted in sintered bulk densities of 95.9% and 99.2%, respectively [64]. Printed AlN parts were heated to 2000 °C and pressed at 310 MPa for 8 h by HIP, leading to a bulk density of 60.1% [55]. Isostatic pressing can increase green and thus sintered densities significantly, but it is not applicable to parts of complex geometries such as internal cavities.

2.6. Knowledge Gaps

To produce dense ceramic parts by binder jetting followed by pressureless sintering, fine powder (e.g., less than 1 μm) is needed because it has a large specific surface energy and thus allows for a high densification level through sintering [52]. However, the spreading, compaction, and densification behaviors are still not well understood.

2.6.1. Spreading behavior

Fine powder is known for its spreading difficulty: it is challenging to form a dense, smooth, and uniform powder bed. It is generally accepted that the spreading difficulty is a result of interparticle cohesion. However, the nature of the interparticle cohesion is not clear. When discussing the interparticle cohesion, researchers usually refer to van der Waals interaction and electrostatic interaction. Hydrogen bonding and capillary bridging are often overlooked. They could play an important role in powder spreading. In addition, the spreader design, spreading strategy and parameters, and environmental humidity can also affect the spreading behavior. However, these effects are still not well understood.

2.6.2. Compaction behavior

A high powder bed density is needed to have high green and consequently sintered densities. An effective way to increase powder bed density is compaction, during which the externally

applied stress exceeds the yield strength of the powder and leads to particle rearrangement [229,230]. Several compaction approaches, including a forward-rotating roller [64,231] and compaction plate [78], have been reported. However, important issues about this layer-by-layer compaction, have not been studied. For example, effects of compaction parameters on the powder bed and its uniformity with the same layer or across different layers are critical but unknown.

2.6.3. Densification behavior

The densification behavior of fine powder has been studied for traditional ceramic pressing and sintering. However, binder jetting poses unique challenges for densification. For example, the green density from binder jetting is usually not as high as that from pressing. It is necessary to understand the densification behavior of loosed packed particles. In addition, binder jetting is developed for producing parts with complex geometries. The relationship between geometry and densification is not well understood.

2.7. Concluding Remarks

Ceramic binder jetting additive manufacturing has many advantages. The main limitation preventing its widespread industrial applications seems to be related to the low density (and thus certain inferior mechanical properties) of printed parts. While various density terminologies have been used for parts by binder jetting, bulk density is more suitable in technical communications for structural applications as it directly determines mechanical properties. It has been reported that special treatment techniques could improve densities. However, most of these techniques have drawbacks, making them inappropriate for a wide range of applications. Granulation is a promising technology, but the literature does not contain sufficient studies on how to eliminate intra- and inter-granule porosities. Fine powder is needed to obtain dense ceramic parts by binder jetting, but there are no reported studies on its spreading, compaction, and densification behaviors.

2.8. References

[1] Klocke, F., 1997, "Modern Approaches for the Production of Ceramic Components," J. Eur. Ceram. Soc., **17**(2–3), pp. 457–465.

[2] Vetalice, J. A., 2012, "The Orthopaedic Industry Annual Report: Focus on Joint Replacement," OrthoKnow, pp. 1–8.

[3] Bose, S., and Tarafder, S., 2012, "Calcium Phosphate Ceramic Systems in Growth Factor and Drug Delivery for Bone Tissue Engineering: A Review," Acta Biomater., **8**(4), pp. 1401–21.

[4] R. Gmeiner, U. Deisinger, J. Schönherr, B. Lechner, R. Detsch, A. R. Boccaccini, J. Stampfl, E. A., 2015, "Additive Manufacturing of Bioactive Glasses and Silicate Bioceramics," J. Ceram. Sci. Technol., **6**(2), pp. 75–86.

[5] ASTM International, 2015, "ISO/ASTM 52900:2015 - Additive Manufacturing — General Principles — Terminology."

[6] Cima, M. J., Sachs, E., Fan, T., Michaels, S. P., Khanuja, S., Lauder, A., Lee, S.-J. J., Brancazio, D., Curodeau, A., and Tuerck, H., 1993, "Three-Dimensional Printing Techniques."

[7] Sachs, E., Cima, M., and Cornie, J., 1990, "Three Dimensional Printing: Rapid Tooling and Prototypes Directly from CAD Pepresentation," *Solid Freeform Fabrication Symposium*, Austin, TX, pp. 27–47.

[8] Chua, C. K., and Leong, K. F., 2014, *3D Printing and Additive Manufacturing: Principles and Applications*, World Scientific, Singapore.

[9] Chua, C. K., Leong, K. F., and Lim, C. S., 2010, *Rapid Prototyping: Principles and Applications*, World Scientific, Singapore.

[10] Chua, C. K., Leong, K. F., and Lim, C. S., 2003, *Rapid Prototyping: Principles and Applications*, World Scientific, Singapore.

[11] "History | ExOne" [Online]. Available: https://www.exone.com/About-ExOne/History. [Accessed: 09-Feb-2019].

[12] "Company History | Voxeljet 3D Printing Solutions" [Online]. Available: https://www.voxeljet.com/company/company-history/. [Accessed: 09-Feb-2019].

[13] "About MicroJet" [Online]. Available: http://www.microjet.com.tw/en/about/#. [Accessed: 09-Feb-2019].

[14] "Production Ready - Desktop Metal Prepares to Unleash Its Production System - TCT Magazine" [Online]. Available: https://www.tctmagazine.com/3d-printing-news/desktop-metal-unleashes-production-system/. [Accessed: 09-Feb-2019].

[15] "Digital Metal 3D Printing: The Smaller, the Better - TCT Magazine" [Online]. Available: https://www.tctmagazine.com/tct-events/tct-show-uk/digital-metal-metal-3d-printing-the-smaller-the-better/. [Accessed: 10-Feb-2019].

[16] Cima, M. J., and Sachs, E. M., 1991, "Three Dimensional Printing: Form, Materials, and Performance," *Solid Freeform Fabrication Symposium*, Austin, TX, pp. 187–194.

[17] Cima, M., Lauder, A., Khanuja, S., and Sachs, E. M., 1992, "Microstructural Elements of Components Derived from 3D Printing," *Solid Freeform Fabrication Symposium*, Austin, TX, pp. 220–227.

[18] Sachs, E., Cima, M., Williams, P., Brancazio, D., and Cornie, J., 1992, "Three Dimensional Printing: Rapid Tooling and Prototypes Directly from a CAD Model," J. Eng. Ind., **114**(4), pp. 481–488.

[19] Sachs, E., Cima, M., Cornie, J., Brancazio, D., Bredt, J., Curodeau, A., Fan, T., Khanuja,

S., Lauder, A., Lee, J., and Michaels, S., 1993, "Three-Dimensional Printing: The Physics and Implications of Additive Manufacturing," CIRP Ann., **42**(1), pp. 257–260.

[20] Sachs, E. M., 2000, "Powder Dispensing Apparatus Using Vibration."

[21] Perrin, S. E., 1991, "Control of Thin Layer Powder Packing Density : Effects of Applied Vibration," Bachelor thesis, Massachusetts Institute of Technology, Cambridge, MA.

[22] Holman, R. K., Cima, M. J., Uhland, S. A., and Sachs, E., 2002, "Spreading and Infiltration of Inkjet-Printed Polymer Solution Droplets on a Porous Substrate," J. Colloid Interface Sci., **249**(2), pp. 432–440.

[23] Moon, J., Grau, J. E., Knezevic, V., Cima, M. J., and Sachs, E. M., 2002, "Ink-Jet Printing of Binders for Ceramic Components," J. Am. Ceram. Soc., **85**(4), pp. 755–762.

[24] Grau, J., Moon, J., Uhland, S., Cima, M., and Sachs, E., 1997, "High Green Density Ceramic Components Fabricated by the Slurry-Based 3DP Process," *Solid Freeform Fabrication Symposium*, Austin, TX, pp. 371–379.

[25] Uhland, S. A., Holman, R. K., Cima, M. J., Sachs, E., and Enokido, Y., 1998, "New Process and Materials Developments in 3-Dimensional Printing, 3DP™," *MRS Proceedings*, Boston, pp. 153–158.

[26] Grau, J. E., 1998, "Fabrication of Engineered Ceramic Components by the Slurry-Based Three Dimensional Printing Process," PhD thesis, Massachusetts Institute of Technology, Cambridge, MA.

[27] Cima, M. J., Wang, H.-R., Cima, M. J., Oliveira, M., Wang, H. R., Sachs, E., and Holman, R., 2001, "Slurry-Based 3DP and Fine Ceramic Components," *Solid Freeform Fabrication Symposium*, Austin, TX, pp. 216–223.

[28] Holman Richard K., 2001, "Effects of the Polymeric Binder System in Slurry-Based

Three Dimensional Printing of Ceramics," PhD thesis, Massachusetts Institute of Technology, Cambridge, MA.

[29] Wang, H. R., 2005, "Gradient-Index (GRIN) Lenses by Slurry-Based Three-Dimensional Printing (S-3DP)," PhD thesis, Massachusetts Institute of Technology, Cambridge, MA.

[30] Grau, J. E., Uhland, S. A., Moon, J., Cima, M. J., and Sachs, E. M., 2004, "Controlled Cracking of Multilayer Ceramic Bodies," J. Am. Ceram. Soc., **82**(8), pp. 2080–2086.

[31] Holman, R. K., Uhland, S. A., Cima, M. J., and Sachs, E., 2002, "Surface Adsorption Effects in the Inkjet Printing of an Aqueous Polymer Solution on a Porous Oxide Ceramic Substrate," J. Colloid Interface Sci., **247**(2), pp. 266–274.

[32] Lauder, A. J., 1992, "Microstructure and Particle Arrangement in Three Dimensional Printing," Master thesis, Massachusetts Institute of Technology, Cambridge, MA.

[33] Oliveira, M. A., 2002, "Slurry Based Three Dimensional Printing (S-3DP) of Tungsten Carbide Cobalt," PhD thesis, Massachusetts Institute of Technology, Cambridge, MA.

[34] Cima, M. J., Sachs, E. M., Cima, L. G., Yoo, J., Khanuja, S., Borland, S. W., Wu, B., and Giordano, R. A., 1994, "Computer-Derived Microstructures by 3D Printing: Bio-and Structural Materials," *Solid Freeform Fabrication Symposium*, Austin, TX, pp. 181–190.

[35] Seitz, H., Rieder, W., Irsen, S., Leukers, B., and Tille, C., 2005, "Three-Dimensional Printing of Porous Ceramic Scaffolds for Bone Tissue Engineering," J. Biomed. Mater. Res. - Part B Appl. Biomater., **74**(2), pp. 782–788.

[36] Dong, C., 1990, "Binder Removal in Ceramics," PhD thesis, Massachusetts Institute of Technology, Cambridge, MA.

[37] Du, W., Ren, X., Ma, C., and Pei, Z., 2017, "Binder Jetting Additive Manufacturing of Ceramics: A Literature Review," *ASME 2017 International Mechanical Engineering*

Congress and Exposition, Tampa, FL, pp. 1–12.

[38] Zocca, A., Lima, P., and Gunster, J., 2017, "LSD-Based 3D Printing of Alumina Ceramics," J. Ceram. Sci. Technol., **8**(1), pp. 141–148.

[39] Moon, J., Caballero, A. C., Hozer, L., Chiang, Y.-M., and Cima, M. J., 2001, "Fabrication of Functionally Graded Reaction Infiltrated SiC–Si Composite by Three-Dimensional Printing (3DP^{TM}) Process," Mater. Sci. Eng. A, **298**(1–2), pp. 110–119.

[40] Trombetta, R., Inzana, J. A., Schwarz, E. M., Kates, S. L., and Awad, H. A., 2017, "3D Printing of Calcium Phosphate Ceramics for Bone Tissue Engineering and Drug Delivery," Ann. Biomed. Eng., **45**(1), pp. 23–44.

[41] Zocca, A., Colombo, P., Gomes, C. M., and Günster, J., 2015, "Additive Manufacturing of Ceramics: Issues, Potentialities, and Opportunities," J. Am. Ceram. Soc., **98**(7), pp. 1983–2001.

[42] Travitzky, N., Bonet, A., Dermeik, B., Fey, T., Filbert-Demut, I., Schlier, L., Schlordt, T., and Greil, P., 2014, "Additive Manufacturing of Ceramic-Based Materials," Adv. Eng. Mater., **16**(6), pp. 729–754.

[43] Jafari, M. A., Han, W., Mohammadi, F., Safari, A., Danforth, S. C., and Langrana, N., 2000, "A Novel System for Fused Deposition of Advanced Multiple Ceramics," Rapid Prototyp. J., **6**(3), pp. 161–175.

[44] Wang, F., Mei, J., Jiang, H., and Wu, X., 2007, "Laser Fabrication of Ti6Al4V/TiC Composites Using Simultaneous Powder and Wire Feed," Mater. Sci. Eng. A, **445**, pp. 461–466.

[45] Balla, V. K., Bose, S., and Bandyopadhyay, A., 2008, "Processing of Bulk Alumina Ceramics Using Laser Engineered Net Shaping," Int. J. Appl. Ceram. Technol., **5**(3), pp.

234–242.

[46] Tay, B. Y., Evans, J. R. G., and Edirisinghe, M. J., 2003, “Solid Freeform Fabrication of Ceramics,” Int. Mater. Rev., **48**(6), pp. 341–370.

[47] Deckers, J., Vleugels, J., and Kruth, J. P., 2014, “Additive Manufacturing of Ceramics: A Review,” J. Ceram. Sci. Technol., **5**(4), pp. 245–260.

[48] Yang, L., and Miyanaji, H., 2017, “Ceramic Additive Manufacturing: A Review of Current Status and Challenges,” *Solid Freeform Fabrication Symposium*, Austin, TX, pp. 652–679.

[49] Ziaee, M., and Crane, N. B., 2019, “Binder Jetting: A Review of Process, Materials, and Methods,” Addit. Manuf., **28**, pp. 781–801.

[50] Moritz, T., and Maleksaeedi, S., 2018, “Additive Manufacturing of Ceramic Components,” *Additive Manufacturing: Materials, Processes, Quantifications and Applications*, Butterworth-Heinemann, Oxford, pp. 105–161.

[51] “Production | Desktop Metal” [Online]. Available: https://www.desktopmetal.com/products/production/. [Accessed: 10-Feb-2019].

[52] Kang, S.-J. L., 2005, *Sintering : Densification, Grain Growth, and Microstructure*, Elsevier Butterworth-Heinemann, Burlington.

[53] Yao, D., Gomes, C. M., Zeng, Y. P., Jiang, D., Günster, J., and Heinrich, J. G., 2015, “Near Zero Shrinkage Porous Al2O3 Prepared via 3D-Printing and Reaction Bonding,” Mater. Lett., **147**, pp. 116–118.

[54] Solis, D. M., Silva, A. V., Volpato, N., and Berti, L. F., 2019, “Reaction-Bonding of Aluminum Oxide Processed by Binder Jetting,” J. Manuf. Process., **41**, pp. 267–272.

[55] Díaz-Moreno, C. A., Lin, Y., Hurtado-Macías, A., Espalin, D., Terrazas, C. A., Murr, L.

E., and Wicker, R. B., 2019, “Binder Jetting Additive Manufacturing of Aluminum Nitride Components,” Ceram. Int., **45**(11), pp. 13620–13627.

[56] Diaz-Moreno, C. A., Rodarte, C., Ambriz, S., Bermudez, D., Roberson, D., Terrazas, C., Espalin, D., Ferguson, R., Shafirovich, E., Lin, Y., and Wicker, R. B., 2018, “Binder Jetting of High Temperature and Thermally Conductive (Aluminum Nitride) Ceramic,” *Solid Freeform Fabrication Symposium*, Austin, TX, pp. 143–159.

[57] Jimenez, E. M., Ding, D., Su, L., Joshi, A. R., Singh, A., Reeja-Jayan, B., and Beuth, J., 2019, “Parametric Analysis to Quantify Process Input Influence on the Printed Densities of Binder Jetted Alumina Ceramics,” Addit. Manuf., **30**, p. 100864.

[58] Kunchala, P., and Kappagantula, K., 2018, “3D Printing High Density Ceramics Using Binder Jetting with Nanoparticle Densifiers,” Mater. Des., **155**, pp. 443–450.

[59] Lanzetta, M., and Sachs, E., 2001, “The Line Formation with Alumina Powders in Drop on Demand Three Dimensional Printing,” *The First International Seminar on Progress in Inovative Manufacturing Engineering*, Sestri Levante, pp. 197–204.

[60] Lee, S. -J. J., Sachs, E., and Cima, M., 1995, “Layer Position Accuracy in Powder-based Rapid Prototyping,” Rapid Prototyp. J., **1**(4), pp. 24–37.

[61] Sachs, E. M., Cima, M. J., Bredt, J. F., Curodeau, A., Fan, T., and Brancazio, D., 1992, “CAD-Casting: The Direct Fabrication of Ceramic Shells and Cores by Three-Dimensional Printing,” Manuf. Rev., **5**(2), pp. 118–126.

[62] Sachs, E., Curodeau, A., Gossard, D., Jee, H., Cima, M., and Caldarise, S., 1994, “Surface Texture by 3D Printing,” *Solid Freeform Fabrication Symposium*, Austin, TX, pp. 56–64.

[63] Melcher, R., Travitzky, N., Zollfrank, C., and Greil, P., 2011, “3D Printing of Al2O3/Cu-O Interpenetrating Phase Composite,” J. Mater. Sci., **46**(5), pp. 1203–1210.

[64] Yoo, J., Cima, M. J., Khanuja, S., and Sachs, E. M., 1993, "Structural Ceramic Components by 3D Printing," *Solid Freeform Fabrication Symposium*, Austin, TX, pp. 40–50.

[65] Du, W., Ren, X., Chen, Y., Ma, C., Radovic, M., and Pei, Z., 2018, "Model Guided Mixing of Ceramic Powders with Graded Particle Sizes in Binder Jetting Additive Manufacturing," *ASME 2018 13th International Manufacturing Science and Engineering Conference*, College Station, TX, pp. 1–9.

[66] Du, W., Ren, X., Ma, C., and Pei, Z., 2019, "Ceramic Binder Jetting Additive Manufacturing: Particle Coating for Increasing Powder Sinterability and Part Strength," Mater. Lett., **234**, pp. 327–330.

[67] Hamano, R., and Ikoma, T., 2018, "Preparation of α-Alumina Powder and Binder For 3D Printer," MRS Adv., **3**(18), pp. 969–975.

[68] Hotta, M., Shimamura, A., Kondo, N., and Ohji, T., 2016, "Powder Layer Manufacturing of Alumina Ceramics Using Water Spray Bonding," J. Ceram. Soc. Japan, **124**(6), pp. 750–752.

[69] Maleksaeedi, S., Eng, H., Wiria, F. E., Ha, T. M. H., and He, Z., 2014, "Property Enhancement of 3D-Printed Alumina Ceramics Using Vacuum Infiltration," J. Mater. Process. Technol., **214**(7), pp. 1301–1306.

[70] Melcher, R., Martins, S., Travitzky, N., and Greil, P., 2006, "Fabrication of Al2O3-Based Composites by Indirect 3D-Printing," Mater. Lett., **60**(4), pp. 572–575.

[71] Zhang, W., Melcher, R., Travitzky, N., Bordia, R. K., and Greil, P., 2009, "Three-Dimensional Printing of Complex-Shaped Alumina/Glass Composites," Adv. Eng. Mater., **11**(12), pp. 1039–1043.

[72] Cima, M. J., Sachs, E. M., Cima, L. G., Yoo, J., Khanuja, S., Borland, S. W., Wu, B., and Giordano, R. A., 1994, "Computer-Derived Microstructures by 3D Printing: Bio- and Structural Materials," *Solid Freeform Fabrication Symposium*, Austin, TX, pp. 181–190.

[73] Fleisher, A., Zolotaryov, D., Kovalevsky, A., Muller-Kamskii, G., Eshed, E., Kazakin, M., and Popov, V. V., 2019, "Reaction Bonding of Silicon Carbides by Binder Jet 3D-Printing, Phenolic Resin Binder Impregnation and Capillary Liquid Silicon Infiltration," Ceram. Int., **45**(14), pp. 18023–18029.

[74] Zhao, H., Ye, C., Fan, Z., and Wang, C., 2017, "3D Printing of CaO-Based Ceramic Core Using Nanozirconia Suspension as a Binder," J. Eur. Ceram. Soc., **37**(15), pp. 5119–5125.

[75] Budding, A., and Vaneker, T. H. J., 2013, "New Strategies for Powder Compaction in Powder-Based Rapid Prototyping Techniques," Procedia CIRP, **6**, pp. 527–532.

[76] Vaezi, M., and Chua, C. K., 2011, "Effects of Layer Thickness and Binder Saturation Level Parameters on 3D Printing Process," Int. J. Adv. Manuf. Technol., **53**(1–4), pp. 275–284.

[77] Lima, P., Zocca, A., Acchar, W., and Günster, J., 2018, "3D Printing of Porcelain by Layerwise Slurry Deposition," J. Eur. Ceram. Soc., **38**(9), pp. 3395–3400.

[78] Rabinskiy, L. N., Sitnikov, S. A., Pogodin, V. A., Ripetskiy, A. A., and Solyaev, Y. O., 2017, "Binder Jetting of Si3N4 Ceramics with Different Porosity," Solid State Phenom., **269**, pp. 37–50.

[79] Rabinskiy, L., Ripetsky, A., Sitnikov, S., Solyaev, Y., and Kahramanov, R., 2016, "Fabrication of Porous Silicon Nitride Ceramics Using Binder Jetting Technology," IOP Conf. Ser. Mater. Sci. Eng., **140**(1), pp. 1–6.

[80] Fu, Z., Schlier, L., Travitzky, N., and Greil, P., 2013, "Three-Dimensional Printing of

SiSiC Lattice Truss Structures," Mater. Sci. Eng. A, **560**, pp. 851–856.

[81] Zocca, A., Lima, P., Diener, S., Katsikis, N., and Günster, J., 2019, "Additive Manufacturing of SiSiC by Layerwise Slurry Deposition and Binder Jetting (LSD-Print)," J. Eur. Ceram. Soc., **39**(13), pp. 3527–3533.

[82] Travitzky, N., Zimmermann, K., Melcher, R., and Greil, P., 2006, "From Polysaccharides to SiSiC Composites by 3d Printing," *Proceedings of the 107th Annual Meeting of The American Ceramic Society*, Baltimore, MD, pp. 37–45.

[83] Zocca, A., Gomes, C. M., Staude, A., Bernardo, E., Günster, J., and Colombo, P., 2013, "SiOC Ceramics with Ordered Porosity by 3D-Printing of a Preceramic Polymer," J. Mater. Res., **28**(17), pp. 2243–2252.

[84] Myers, K., Juhasz, M., Cortes, P., and Conner, B., 2015, "Mechanical Modeling Based on Numerical Homogenization of an Al2O3/Al Composite Manufactured via Binder Jet Printing," Comput. Mater. Sci., **108**, **Part**, pp. 128–135.

[85] Nan, B., Yin, X., Zhang, L., and Cheng, L., 2011, "Three-Dimensional Printing of Ti3SiC2-Based Ceramics," J. Am. Ceram. Soc., **94**(4), pp. 969–972.

[86] Yin, X., Travitzky, N., Melcher, R., and Greil, P., 2006, "Three-Dimensional Printing of TiAl3/Al2O3 Composites," Zeitschrift für Met., **97**(5), pp. 492–498.

[87] Yin, X., Travitzky, N., and Greil, P., 2007, "Near-Net-Shape Fabrication of Ti3AlC2-Based Composites," Int. J. Appl. Ceram. Technol., **4**(2), pp. 184–190.

[88] Yin, X., Travitzky, N., and Greil, P., 2007, "Three-Dimensional Printing of Nanolaminated Ti3AlC2 Toughened TiAl3-Al2O3 Composites," J. Am. Ceram. Soc., **90**(7), pp. 2128–2134.

[89] Sun, W., Dcosta, D. J., Lin, F., and El-Raghy, T., 2002, "Freeform Fabrication of Ti3SiC2

Powder-Based Structures: Part I—Integrated Fabrication Process," J. Mater. Process. Technol., **127**(3), pp. 343–351.

[90] Dcosta, D. J., Sun, W., Lin, F., and Ei-Raghy, T., 2002, "Freeform Fabrication of Ti3SiC2 Powder-Based Structures: Part II - Characterization and Microstructure Evaluation," J. Mater. Process. Technol., **127**(3), pp. 352–360.

[91] Enneti, R. K., Prough, K. C., Wolfe, T. A., Klein, A., Studley, N., and Trasorras, J. L., 2018, "Sintering of WC-12%Co Processed by Binder Jet 3D Printing (BJ3DP) Technology," Int. J. Refract. Met. Hard Mater., **71**, pp. 28–35.

[92] Enneti, R. K., and Prough, K. C., 2019, "Wear Properties of Sintered WC-12%Co Processed via Binder Jet 3D Printing (BJ3DP)," Int. J. Refract. Met. Hard Mater., **78**, pp. 228–232.

[93] Kernan, B. D., Sachs, E. M., Oliveira, M. A., and Cima, M. J., 2007, "Three-Dimensional Printing of Tungsten Carbide–10 Wt% Cobalt Using a Cobalt Oxide Precursor," Int. J. Refract. Met. Hard Mater., **25**(1), pp. 82–94.

[94] Zhao, H., Ye, C., Fan, Z., and Shi, Y., 2015, "3D Printing of ZrO2 Ceramic Using Nano-Zirconia Suspension as a Binder," *4th International Conference on Sensors, Measurement and Intelligent Materials*, Atlantis Press, Shenzhen, pp. 654–657.

[95] Mancuso, E., Alharbi, N., Bretcanu, O. A., Marshall, M., Birch, M. A., McCaskie, A. W., and Dalgarno, K. W., 2017, "Three-Dimensional Printing of Porous Load-Bearing Bioceramic Scaffolds," Proc. Inst. Mech. Eng. Part H J. Eng. Med., **231**(6), pp. 575–585.

[96] Zocca, A., Gomes, C. M., Bernardo, E., Muller, R., Gunster, J., and Colombo, P., 2013, "LAS Glass-Ceramic Scaffolds by Three-Dimensional Printing," J. Eur. Ceram. Soc., **33**(9), pp. 1525–1533.

[97] Sun, C., Tian, X., Wang, L., Liu, Y., Wirth, C. M., Günster, J., Li, D., and Jin, Z., 2017, "Effect of Particle Size Gradation on the Performance of Glass-Ceramic 3D Printing Process," Ceram. Int., **43**(1), pp. 578–584.

[98] Winkel, A., Meszaros, R., Reinsch, S., Müller, R., Travitzky, N., Fey, T., Greil, P., and Wondraczek, L., 2012, "Sintering of 3D-Printed Glass/HAp Composites," J. Am. Ceram. Soc., **95**(11), pp. 3387–3393.

[99] Seidenstuecker, M., Kerr, L., Bernstein, A., Mayr, H., Suedkamp, N., Gadow, R., Krieg, P., Hernandez Latorre, S., Thomann, R., Syrowatka, F., and Esslinger, S., 2017, "3D Powder Printed Bioglass and β-Tricalcium Phosphate Bone Scaffolds," Materials (Basel)., **11**(13), pp. 1–21.

[100] Bergmann, C., Lindner, M., Zhang, W., Koczur, K., Kirsten, A., Telle, R., and Fischer, H., 2010, "3D Printing of Bone Substitute Implants Using Calcium Phosphate and Bioactive Glasses," J. Eur. Ceram. Soc., **30**(12), pp. 2563–2567.

[101] Suwanprateeb, J., Sanngam, R., Suvannapruk, W., and Panyathanmaporn, T., 2009, "Mechanical and in Vitro Performance of Apatite-Wollastonite Glass Ceramic Reinforced Hydroxyapatite Composite Fabricated by 3D-Printing," J. Mater. Sci. Mater. Med., **20**(6), pp. 1281–1289.

[102] Zocca, A., Elsayed, H., Bernardo, E., Gomes, C. M., Lopez-Heredia, M. A., Knabe, C., Colombo, P., and Günster, J., 2015, "3D-Printed Silicate Porous Bioceramics Using a Non-Sacrificial Preceramic Polymer Binder," Biofabrication, **7**(2), pp. 1–12.

[103] Komlev, V. S., Popov, V. K., Mironov, A. V, Fedotov, A. Y., Teterina, A. Y., Smirnov, I. V, Bozo, I. Y., Rybko, V. A., and Deev, R. V, 2015, "3D Printing of Octacalcium Phosphate Bone Substitutes," Front. Bioeng. Biotechnol., **3**, pp. 1–7.

[104] Szucs, T. D., and Brabazon, D., 2009, "Effect of Saturation and Post Processing on 3D Printed Calcium Phosphate Scaffolds," Bioceram. 21, **396**–**398**, pp. 663–666.

[105] El-Ghannam, A., Cunningham, L., Pienkowski, D., and Hart, A., 2007, "Bone Engineering of the Rabbit Ulna," J. Oral Maxillofac. Surg., **65**(8), pp. 1495–1502.

[106] El-Ghannam, A., Hart, A., White, D., and Cunningham, L., 2013, "Mechanical Properties and Cytotoxicity of a Resorbable Bioactive Implant Prepared by Rapid Prototyping Technique," J. Biomed. Mater. Res. - Part A, **101**(10), pp. 2851–2861.

[107] Shanjani, Y., Amritha De Croos, J. N., Pilliar, R. M., Kandel, R. A., and Toyserkani, E., 2010, "Solid Freeform Fabrication and Characterization of Porous Calcium Polyphosphate Structures for Tissue Engineering Purposes," J. Biomed. Mater. Res. - Part B Appl. Biomater., **93**(2), pp. 510–519.

[108] Sheydaeian, E., Vlasea, M., Woo, A., Pilliar, R., Hu, E., and Toyserkani, E., 2017, "Effect of Glycerol Concentrations on the Mechanical Properties of Additive Manufactured Porous Calcium Polyphosphate Structures for Bone Substitute Applications," J. Biomed. Mater. Res. - Part B Appl. Biomater., **105**(4), pp. 828–835.

[109] Butscher, A., Bohner, M., Roth, C., Ernstberger, A., Heuberger, R., Doebelin, N., Rudolf Von Rohr, P., and Müller, R., 2012, "Printability of Calcium Phosphate Powders for Three-Dimensional Printing of Tissue Engineering Scaffolds," Acta Biomater., **8**(1), pp. 373–385.

[110] Butscher, A., Bohner, M., Doebelin, N., Galea, L., Loeffel, O., and Müller, R., 2013, "Moisture Based Three-Dimensional Printing of Calcium Phosphate Structures for Scaffold Engineering," Acta Biomater., **9**(2), pp. 5369–5378.

[111] Mehrban, N., Bowen, J., Vorndran, E., Gbureck, U., and Grover, L. M., 2013, "Structural

Changes to Resorbable Calcium Phosphate Bioceramic Aged in Vitro," Colloids Surfaces B Biointerfaces, **111**, pp. 469–478.

[112] Peters, F., Groisman, D., Davids, R., Hänel, T., Dürr, H., and Klein, M., 2006, "Comparative Study of Patient Individual Implants from β-Tricalcium Phosphate Made by Different Techniques Based on CT Data," Materwiss. Werksttech., **37**(6), pp. 457–461.

[113] Klammert, U., Gbureck, U., Vorndran, E., Rödiger, J., Meyer-Marcotty, P., and Kübler, A. C., 2010, "3D Powder Printed Calcium Phosphate Implants for Reconstruction of Cranial and Maxillofacial Defects," J. Cranio-Maxillofacial Surg., **38**(8), pp. 565–570.

[114] Tamimi, F., Torres, J., Gbureck, U., Lopez-Cabarcos, E., Bassett, D. C., Alkhraisat, M. H., and Barralet, J. E., 2009, "Craniofacial Vertical Bone Augmentation: A Comparison between 3D Printed Monolithic Monetite Blocks and Autologous Onlay Grafts in the Rabbit," Biomaterials, **30**(31), pp. 6318–6326.

[115] Tamimi, F., Torres, J., Al-Abedalla, K., Lopez-Cabarcos, E., Alkhraisat, M. H., Bassett, D. C., Gbureck, U., and Barralet, J. E., 2014, "Osseointegration of Dental Implants in 3D-Printed Synthetic Onlay Grafts Customized According to Bone Metabolic Activity in Recipient Site," Biomaterials, **35**(21), pp. 5436–5445.

[116] Torres, J., Tamimi, F., Alkhraisat, M. H., Prados-Frutos, J. C., Rastikerdar, E., Gbureck, U., Barralet, J. E., and Lõpez-Cabarcos, E., 2011, "Vertical Bone Augmentation with 3D-Synthetic Monetite Blocks in the Rabbit Calvaria," J. Clin. Periodontol., **38**(12), pp. 1147–1153.

[117] Gbureck, U., Hölzel, T., Klammert, U., Würzler, K., Müller, F. A., and Barralet, J. E., 2007, "Resorbable Dicalcium Phosphate Bone Substitutes Prepared by 3D Powder Printing," Adv. Funct. Mater., **17**(18), pp. 3940–3945.

[118] Castilho, M., Dias, M., Vorndran, E., Gbureck, U., Fernandes, P., Pires, I., Gouveia, B., Armés, H., Pires, E., and Rodrigues, J., 2014, "Application of a 3D Printed Customized Implant for Canine Cruciate Ligament Treatment by Tibial Tuberosity Advancement," Biofabrication, **6**(2), pp. 1–13.

[119] Habibovic, P., Gbureck, U., Doillon, C. J., Bassett, D. C., van Blitterswijk, C. A., and Barralet, J. E., 2008, "Osteoconduction and Osteoinduction of Low-Temperature 3D Printed Bioceramic Implants," Biomaterials, **29**(7), pp. 944–953.

[120] Gbureck, U., Hölzel, T., Doillon, C. J., Müller, F. A., and Barralet, J. E., 2007, "Direct Printing of Bioceramic Implants with Spatially Localized Angiogenic Factors," Adv. Mater., **19**(6), pp. 795–800.

[121] Vorndran, E., Klarner, M., Klammert, U., Grover, L. M., Patel, S., Barralet, J. E., and Gbureck, U., 2008, "3D Powder Printing of β-Tricalcium Phosphate Ceramics Using Different Strategies," Adv. Eng. Mater., **10**(12), pp. B67–B71.

[122] Klammert, U., Reuther, T., Jahn, C., Kraski, B., Kübler, A. C., and Gbureck, U., 2009, "Cytocompatibility of Brushite and Monetite Cell Culture Scaffolds Made by Three-Dimensional Powder Printing," Acta Biomater., **5**(2), pp. 727–734.

[123] Gbureck, U., Hölzel, T., Biermann, I., Barralet, J. E., and Grover, L. M., 2008, "Preparation of Tricalcium Phosphate/Calcium Pyrophosphate Structures via Rapid Prototyping," J. Mater. Sci. Mater. Med., **19**(4), pp. 1559–1563.

[124] Birkholz, M. N., Agrawal, G., Bergmann, C., Schröder, R., Lechner, S. J., Pich, A., and Fischer, H., 2015, "Calcium Phosphate/Microgel Composites for 3D Powderbed Printing of Ceramic Materials," Biomed. Tech., **61**(3), pp. 267–279.

[125] Tarafder, S., Balla, V. K., Davies, N. M., Bandyopadhyay, A., and Bose, S., 2013,

"Microwave-Sintered 3D Printed Tricalcium Phosphate Scaffolds for Bone Tissue Engineering," J. Tissue Eng. Regen. Med., **7**(8), pp. 631–641.

[126] Warnke, P. H., Seitz, H., Warnke, F., Becker, S. T., Sivananthan, S., Sherry, E., Liu, Q., Wiltfang, J., and Douglas, T., 2010, "Ceramic Scaffolds Produced by Computer-Assisted 3D Printing and Sintering: Characterization and Biocompatibility Investigations," J. Biomed. Mater. Res. - Part B Appl. Biomater., **93**(1), pp. 212–217.

[127] Becker, S. T., Bolte, H., Krapf, O., Seitz, H., Douglas, T., Sivananthan, S., Wiltfang, J., Sherry, E., and Warnke, P. H., 2009, "Endocultivation: 3D Printed Customized Porous Scaffolds for Heterotopic Bone Induction," Oral Oncol., **45**(11), pp. e181–e188.

[128] Igawa, K., Mochizuki, M., Sugimori, O., Shimizu, K., Yamazawa, K., Kawaguchi, H., Nakamura, K., Takato, T., Nishimura, R., Suzuki, S., and Anzai, M., 2006, "Tailor-Made Tricalcium Phosphate Bone Implant Directly Fabricated by a Three-Dimensional Ink-Jet Printer," J. Artif. Organs, **9**(4), pp. 234–240.

[129] Santos, C. F. L., Silva, A. P., Lopes, L., Pires, I., and Correia, I. J., 2012, "Design and Production of Sintered β-Tricalcium Phosphate 3D Scaffolds for Bone Tissue Regeneration," Mater. Sci. Eng. C, **32**(5), pp. 1293–1298.

[130] Barralet, J., Gbureck, U., Habibovic, P., Vorndran, E., Gerard, C., and Doillon, C. J., 2009, "Angiogenesis in Calcium Phosphate Scaffolds by Inorganic Copper Ion Release.," Tissue Eng. Part A, **15**(7), pp. 1601–1609.

[131] Roy, T. D., Simon, J. L., Ricci, J. L., Rekow, E. D., Thompson, V. P., and Parsons, J. R., 2003, "Performance of Degradable Composite Bone Repair Products Made via Three-Dimensional Fabrication Techniques," J. Biomed. Mater. Res., **66A**(2), pp. 283–291.

[132] Tarafder, S., Davies, N. M., Bandyopadhyay, A., and Bose, S., 2013, "3D Printed

Tricalcium Phosphate Bone Tissue Engineering Scaffolds: Effect of SrO and MgO Doping on in Vivo Osteogenesis in a Rat Distal Femoral Defect Model," Biomater. Sci., **1**(12), pp. 1250–1259.

[133] Tarafder, S., Dernell, W. S., Bandyopadhyay, A., and Bose, S., 2015, "SrO- and MgO-Doped Microwave Sintered 3D Printed Tricalcium Phosphate Scaffolds: Mechanical Properties and in Vivo Osteogenesis in a Rabbit Model," J. Biomed. Mater. Res. - Part B Appl. Biomater., **103**(3), pp. 679–690.

[134] Bose, S., Tarafder, S., and Bandyopadhyay, A., 2017, "Effect of Chemistry on Osteogenesis and Angiogenesis Towards Bone Tissue Engineering Using 3D Printed Scaffolds," Ann. Biomed. Eng., **45**(1), pp. 261–272.

[135] Fielding, G. A., Bandyopadhyay, A., and Bose, S., 2012, "Effects of Silica and Zinc Oxide Doping on Mechanical and Biological Properties of 3D Printed Tricalcium Phosphate Tissue Engineering Scaffolds," Dent. Mater., **28**(2), pp. 113–122.

[136] Castilho, M., Moseke, C., Ewald, A., Gbureck, U., Groll, J., Pires, I., Teßmar, J., and Vorndran, E., 2014, "Direct 3D Powder Printing of Biphasic Calcium Phosphate Scaffolds for Substitution of Complex Bone Defects," Biofabrication, **6**(1), pp. 1–12.

[137] Khalyfa, A., Vogt, S., Weisser, J., Grimm, G., Rechtenbach, A., Meyer, W., and Schnabelrauch, M., 2007, "Development of a New Calcium Phosphate Powder-Binder System for the 3D Printing of Patient Specific Implants," J. Mater. Sci. Mater. Med., **18**(5), pp. 909–916.

[138] Vella, J. B., Trombetta, R. P., Hoffman, M. D., Inzana, J., Awad, H., and Benoit, D. S. W., 2017, "Three Dimensional Printed Calcium Phosphate and Poly(Caprolactone) Composites with Improved Mechanical Properties and Preserved Microstructure," J.

Biomed. Mater. Res. - Part A, pp. 1–10.

[139] Inzana, J. A., Olvera, D., Fuller, S. M., Kelly, J. P., Graeve, O. A., Schwarz, E. M., Kates, S. L., and Awad, H. A., 2014, "3D Printing of Composite Calcium Phosphate and Collagen Scaffolds for Bone Regeneration," Biomaterials, **35**(13), pp. 4026–4034.

[140] Seitz, H., Deisinger, U., Leukers, B., Detsch, R., and Ziegler, G., 2009, "Different Calcium Phosphate Granules for 3-D Printing of Bone Tissue Engineering Scaffolds," Adv. Eng. Mater., **11**(5), pp. 41–46.

[141] Wang, Y., Wang, K., Li, X., Wei, Q., Chai, W., Wang, S., Che, Y., Lu, T., and Zhang, B., 2017, "3D Fabrication and Characterization of Phosphoric Acid Scaffold with a HA / β - TCP Weight Ratio of 60 : 40 for Bone Tissue Engineering Applications," PLoS One, **12**(4), pp. 1–17.

[142] Strobel, L., Rath, S., Maier, A., Beier, J., Arkudas, A., Greil, P., Horch, R., and Kneser, U., 2014, "Induction of Bone Formation in Biphasic Calcium Phosphate Scaffolds by Bone Morphogenetic Protein-2 and Primary Osteoblasts," J. Tissue Eng. Regen. Med., **8**(3), pp. 176–185.

[143] Rath, S. N., Strobel, L. A., Arkudas, A., Beier, J. P., Maier, A. K., Greil, P., Horch, R. E., and Kneser, U., 2012, "Osteoinduction and Survival of Osteoblasts and Bone-Marrow Stromal Cells in 3D Biphasic Calcium Phosphate Scaffolds under Static and Dynamic Culture Conditions," J. Cell. Mol. Med., **16**(10), pp. 2350–2361.

[144] Detsch, R., Schaefer, S., Deisinger, U., Ziegler, G., Seitz, H., and Leukers, B., 2011, "In Vitro -Osteoclastic Activity Studies on Surfaces of 3D Printed Calcium Phosphate Scaffolds," J. Biomater. Appl., **26**(3), pp. 359–380.

[145] Zhou, Z., Buchanan, F., Mitchell, C., and Dunne, N., 2014, "Printability of Calcium

Phosphate: Calcium Sulfate Powders for the Application of Tissue Engineered Bone Scaffolds Using the 3D Printing Technique," Mater. Sci. Eng. C, **38**(1), pp. 1–10.

[146] Spath, S., Drescher, P., and Seitz, H., 2015, "Impact of Particle Size of Ceramic Granule Blends on Mechanical Strength and Porosity of 3D Printed Scaffolds," Materials (Basel)., **8**(8), pp. 4720–4732.

[147] Chumnanklang, R., Panyathanmaporn, T., Sitthiseripratip, K., and Suwanprateeb, J., 2007, "3D Printing of Hydroxyapatite: Effect of Binder Concentration in Pre-Coated Particle on Part Strength," Mater. Sci. Eng. C, **27**(4), pp. 914–921.

[148] Wang, Y., Li, X., Li, C., Yang, M., and Wei, Q., 2015, "Binder Droplet Impact Mechanism on a Hydroxyapatite Microsphere Surface in 3D Printing of Bone Scaffolds," J. Mater. Sci., **50**(14), pp. 5014–5023.

[149] Fierz, F. C., Beckmann, F., Huser, M., Irsen, S. H., Leukers, B., Witte, F., Degistirici, Ö., Andronache, A., Thie, M., and Müller, B., 2008, "The Morphology of Anisotropic 3D-Printed Hydroxyapatite Scaffolds," Biomaterials, **29**(28), pp. 3799–3806.

[150] Irsen, S. H., Leukers, B., Höckling, C., Tille, C., and Seitz, H., 2006, "Bioceramic Granulates for Use in 3D Printing: Process Engineering Aspects," Materwiss. Werksttech., **37**(6), pp. 533–537.

[151] Leukers, B., Gülkan, H., Irsen, S., and Milz, S., 2005, "Hydroxyapatite Scaffolds for Bone Tissue Engineering Made by 3D Printing," J. Mater. Sci. Mater. Med., **6**, pp. 1121–1124.

[152] Suwanprateeb, J., Sanngam, R., and Panyathanmaporn, T., 2010, "Influence of Raw Powder Preparation Routes on Properties of Hydroxyapatite Fabricated by 3D Printing Technique," Mater. Sci. Eng. C, **30**(4), pp. 610–617.

[153] Will, J., Melcher, R., Treul, C., Travitzky, N., Kneser, U., Polykandriotis, E., Horch, R.,

and Greil, P., 2008, “Porous Ceramic Bone Scaffolds for Vascularized Bone Tissue Regeneration,” J. Mater. Sci. Mater. Med., **19**(8), pp. 2781–2790.

[154] Qian, C., and Sun, J., 2013, “Fabrication of the Porous Hydroxyapatite Implant by 3D Printing,” J. Ceram. Process. Res., **14**(4), pp. 513–516.

[155] Suwanprateeb, J., Sanngam, R., and Suwanpreuk, W., 2008, “Fabrication of Bioactive Hydroxyapatite/Bis-GMA Based Composite via Three Dimensional Printing,” J. Mater. Sci. Mater. Med., **19**(7), pp. 2637–2645.

[156] Farzadi, A., Solati-Hashjin, M., Asadi-Eydivand, M., and Osman, N. A. A., 2014, “Effect of Layer Thickness and Printing Orientation on Mechanical Properties and Dimensional Accuracy of 3D Printed Porous Samples for Bone Tissue Engineering,” PLoS One, **9**(9), pp. 1–14.

[157] Farzadi, A., Waran, V., Solati-Hashjin, M., Rahman, Z. A. A., Asadi, M., and Osman, N. A. A., 2015, “Effect of Layer Printing Delay on Mechanical Properties and Dimensional Accuracy of 3D Printed Porous Prototypes in Bone Tissue Engineering,” Ceram. Int., **41**(7), pp. 8320–8330.

[158] Asadi-Eydivand, M., Solati-Hashjin, M., Fathi, A., Padashi, M., and Abu Osman, N. A., 2016, “Optimal Design of a 3D-Printed Scaffold Using Intelligent Evolutionary Algorithms,” Appl. Soft Comput. J., **39**, pp. 36–47.

[159] Suwanprateeb, J., Thammarakcharoen, F., and Hobang, N., 2016, “Enhancement of Mechanical Properties of 3D Printed Hydroxyapatite by Combined Low and High Molecular Weight Polycaprolactone Sequential Infiltration,” J. Mater. Sci. Mater. Med., **27**(11), pp. 1–12.

[160] Suwanprateeb, J., Thammarakcharoen, F., Wasoontararat, K., and Suvannapruk, W., 2012,

"Influence of Printing Parameters on the Transformation Efficiency of 3D-Printed Plaster of Paris to Hydroxyapatite and Its Properties," Rapid Prototyp. J., **18**(6), pp. 490–499.

[161] Lowmunkong, R., Sohmura, T., Suzuki, Y., Matsuya, S., and Ishikawa, K., 2009, "Fabrication of Freeform Bone-Filling Calcium Phosphate Ceramics by Gypsum 3D Printing Method," J. Biomed. Mater. Res. - Part B Appl. Biomater., **90 B**(2), pp. 531–539.

[162] Zhou, Z., Mitchell, C. A., Buchanan, F. J., and Dunne, N. J., 2013, "Effects of Heat Treatment on the Mechanical and Degradation Properties of 3D-Printed Calcium-Sulphate-Based Scaffolds," ISRN Biomater., **2013**, pp. 1–10.

[163] Suvannapruk, W., Thammarakcharoen, F., Phanpiriya, P., and Suwanprateeb, J., 2013, "Development of Antibiotics Impregnated Nanosized Silver Phosphate-Doped Hydroxyapatite Bone Graft," J. Nanomater., **2013**, pp. 1–9.

[164] Meininger, S., Mandal, S., Kumar, A., Groll, J., Basu, B., and Gbureck, U., 2016, "Strength Reliability and in Vitro Degradation of Three-Dimensional Powder Printed Strontium-Substituted Magnesium Phosphate Scaffolds," Acta Biomater., **31**, pp. 401–411.

[165] Klammert, U., Vorndran, E., Reuther, T., Müller, F. A., Zorn, K., and Gbureck, U., 2010, "Low Temperature Fabrication of Magnesium Phosphate Cement Scaffolds by 3D Powder Printing," J. Mater. Sci. Mater. Med., **21**(11), pp. 2947–2953.

[166] Gonzalez, J. A., Mireles, J., Lin, Y., and Wicker, R. B., 2016, "Characterization of Ceramic Components Fabricated Using Binder Jetting Additive Manufacturing Technology," Ceram. Int., **42**, pp. 10559–10564.

[167] Gaytan, S. M., Cadena, M. A., Karim, H., Delfin, D., Lin, Y., Espalin, D., MacDonald, E., and Wicker, R. B., 2015, "Fabrication of Barium Titanate by Binder Jetting Additive

Manufacturing Technology," Ceram. Int., **41**(5), pp. 6610–6619.

[168] Gaytan, S. M., Cadena, M., Aldaz, M., Herderick, E., Medina, F., and Wicker, R., 2013, "Analysis of Ferroelectric Ceramic Fabricated by Binder Jetting Technology," *Proceedings of Solid Freeform Fabrication Symposium*, Austin, pp. 859–868.

[169] Utela, B., Anderson, R. L., and Kuhn, H., 2006, "Advanced Ceramic Materials and Processes for Three-Dimensional Printing (3DP)," *Solid Freeform Fabrication Symposium*, Austin, TX, pp. 290–303.

[170] Miyanaji, H., Zhang, S., Lassell, A., Zandinejad, A. A., and Yang, L., 2016, "Optimal Process Parameters for 3D Printing of Porcelain Structures," Procedia Manuf., **5**, pp. 870–887.

[171] Miyanaji, H., Zhang, S., Lassell, A., Zandinejad, A., and Yang, L., 2016, "Process Development of Porcelain Ceramic Material with Binder Jetting Process for Dental Applications," JOM, **68**(3), pp. 831–841.

[172] Miyanaji, H., Yang, L., Zhang, S., and Zandinejad, A., 2014, "A Preliminary Study of the Graded Dental Porcelain Ceramic Structures Fabricated via Binder Jetting 3D Printing," *Solid Freeform Fabrication Symposium*, Austin, TX, pp. 578–589.

[173] Wang, H.-R., Cima, M. J., and Sachs, E. M., 2002, "Three-Dimensional Printing (3DP^{TM}) of Gradient-Index (GRIN) Lenses," *Proceedings of the Innovative Processing and Synthesis of Ceramics, Glasses and Composites*, St. Louis, MS, pp. 191–201.

[174] Kumar, A., Nune, K. C., Murr, L. E., and Misra, R. D. K., 2016, "Biocompatibility and Mechanical Behaviour of Three-Dimensional Scaffolds for Biomedical Devices: Process–Structure–Property Paradigm," Int. Mater. Rev., **61**(1), pp. 20–45.

[175] Hsu, T., and Lai, W., 2010, "Manufacturing Parts Optimization in the Three-dimensional

Printing Process by the Taguchi Method," J. Chinese Inst. Eng., **33**(1), pp. 121–130.

[176] Butscher, A., Bohner, M., Hofmann, S., Gauckler, L., and Müller, R., 2011, "Structural and Material Approaches to Bone Tissue Engineering in Powder-Based Three-Dimensional Printing," Acta Biomater., **7**(3), pp. 907–920.

[177] Utela, B., Storti, D., Anderson, R., and Ganter, M., 2008, "A Review of Process Development Steps for New Material Systems in Three Dimensional Printing (3DP)," J. Manuf. Process., **10**(2), pp. 96–104.

[178] Spath, S., and Seitz, H., 2014, "Influence of Grain Size and Grain-Size Distribution on Workability of Granules with 3D Printing," Int. J. Adv. Manuf. Technol., **70**(1–4), pp. 135–144.

[179] ASTM International, 2015, "B527-15: Standard Test Method for Tap Density of Metal Powders and Compounds."

[180] ISO, 2011, "ISO 3953:2011 Metallic Powders — Determination of Tap Density."

[181] German, R. M., 2014, *Sintering : From Empirical Observations to Scientific Principles*, Butterworth-Heinemann.

[182] Hwang, H. J., Yasuoka, M., Sando, M., Toriyama, M., and Niihara, K., 1999, "Fabrication, Sinterability, and Mechanical Properties of Lead Zirconate Titanate/Silver Composites," J. Am. Ceram. Soc., **82**(9), pp. 2417–2422.

[183] Saboori, A., Novara, C., Pavese, M., Badini, C., Giorgis, F., and Fino, P., 2017, "An Investigation on the Sinterability and the Compaction Behavior of Aluminum/Graphene Nanoplatelets (GNPs) Prepared by Powder Metallurgy," J. Mater. Eng. Perform., **26**(3), pp. 993–999.

[184] Callister, W. D., and Rethwisch, D. G., 2009, *Materials Science and Engineering: An*

Introduction, Wiley, Danvers.

[185] Gildenhaar, R., Knabe, C., Gomes, C., Linow, U., Houshmand, A., and Berger, G., 2011, "Calcium Alkaline Phosphate Scaffolds for Bone Regeneration 3D-Fabricated by Additive Manufacturing," Key Eng. Mater., **493**, pp. 849–854.

[186] Cho, G.-C., Dodds, J., and Santamarina, J. C., 2006, "Particle Shape Effects on Packing Density, Stiffness, and Strength: Natural and Crushed Sands," J. Geotech. Geoenvironmental Eng., **132**(5), pp. 591–602.

[187] Yu, A. B., Bridgwater, J., and Burbidge, A., 1997, "On the Modelling of the Packing of Fine Particles," Powder Technol., **92**(3), pp. 185–194.

[188] Cai, K., Román-Manso, B., Smay, J. E., Zhou, J., Osendi, M. I., Belmonte, M., and Miranzo, P., 2012, "Geometrically Complex Silicon Carbide Structures Fabricated by Robocasting," J. Am. Ceram. Soc., **95**(8), pp. 2660–2666.

[189] Haeri, S., Wang, Y., Ghita, O., and Sun, J., 2017, "Discrete Element Simulation and Experimental Study of Powder Spreading Process in Additive Manufacturing," Powder Technol., **306**, pp. 45–54.

[190] Shanjani, Y., and Ehsan, T., 2008, "Material Spreading and Compaction in Powder-Based Solid Freeform Fabrication Methods: Mathematical Modeling," *Solid Freeform Fabrication Symposium*, Austin, TX, pp. 399–410.

[191] Roy, N. K., and Cullinan, M. A., 2015, "μ-SLS of Metals: Design of the Powder Spreader, Powder Bed Actuators and Optics for the System," *Solid Freeform Fabrication Symposium*, Austin, TX, pp. 134–155.

[192] Apelt, D., Theiss, F., El-Warrak, A. O., Zlinszky, K., Bettschart-Wolfisberger, R., Bohner, M., Matter, S., Auer, J. A., and Von Rechenberg, B., 2004, "In Vivo Behavior of Three

Different Injectable Hydraulic Calcium Phosphate Cements," Biomaterials, **25**, pp. 1439–1451.

[193] Bredt, J. F., Anderson, T. C., and Russell, D. B., 2006, "Three Dimensional Printing Material System and Method."

[194] Vacanti, J. P., Cima, L. G., and Cima, M. . I., 2001, "Vascularized Tissue Regeneration Matrices Formed By Solid Free Form Fabrication Techniques."

[195] Meier, C., Weissbach, R., Weinberg, J., Wall, W. A., and Hart, A. J., 2019, "Critical Influences of Particle Size and Adhesion on the Powder Layer Uniformity in Metal Additive Manufacturing," J. Mater. Process. Technol., **266**, pp. 484–501.

[196] Katashinskii, V. P., and Shtern, M. B., 1983, "Stressed-Strained State of Powder Being Rolled in the Densification Zone. I. Mathematical Model of Rolling in the Densification Zone," Sov. Powder Metall. Met. Ceram., **22**(11), pp. 882–885.

[197] Jenni, M., Schimmer, L., and Zauner, R., 2008, "Quantitative Study of Powder Binder Separation of Feedstocks," PIM Int., **2**(4), pp. 50–55.

[198] ASTM International, 2013, "B212-13: Standard Test Method for Apparent Density of Free-Flowing Metal Powders Using the Hall Flowmeter Funnel."

[199] ASTM International, 2014, "B329-14: Standard Test Method for Apparent Density of Metal Powders and Compounds Using the Scott Volumeter."

[200] ASTM International, 2013, "B417 2013: Standard Test Method for Apparent Density of Non-Free-Flowing Metal Powders Using the Carney Funnel."

[201] ASTM International, 2014, "B703-10: Standard Test Method for Apparent Density of Metal Powders and Related Compounds Using the Arnold Meter."

[202] Elliott, A. M., Nandwana, P., Siddel, D., and Compton, B. G., 2016, "A Method for

Measuring Powder Bed Density in Binder Jet Additive Manufacturing Process and the Powder Feedstock Characteristics Influencing the Powder Bed Density," *Solid Freeform Fabrication Symposium*, Austin, TX, pp. 1031–1037.

[203] ISO, 2013, "ISO 18754:2013 Fine Ceramics (Advanced Ceramics, Advanced Technical Ceramics) – Determination of Density and Apparent Porosity."

[204] ASTM International, 2015, "C20-00: Standard Test Methods for Apparent Porosity, Water Absorption, Apparent Specific Gravity, and Bulk Density of Burned Refractory Brick and Shapes by Boiling Water."

[205] ASTM International, 2017, "C373-17: Standard Test Methods for Water Absorption and Associate Properties by Vacuum Methd for Pressed Ceramic Tiles."

[206] ASTM International, 2017, "B962-17: Standard Test Methods for Density of Compacted or Sintered Powder Metallurgy (PM) Products Using Archimedes' Principle."

[207] Abell, A. B., Willis, K. L., and Lange, D. A., 1999, "Mercury Intrusion Porosimetry and Image Analysis of Cement-Based Materials," J. Colloid Interface Sci., **211**(1), pp. 39–44.

[208] Tamari, S., 2004, "Optimum Design of the Constant-Volume Gas Pycnometer for Determining the Volume of Solid Particles," Meas. Sci. Technol., **15**(3), pp. 549–558.

[209] Sinka, I. C., Burch, S. F., Tweed, J. H., and Cunningham, J. C., 2004, "Measurement of Density Variations in Tablets Using X-Ray Computed Tomography," Int. J. Pharm., **271**(1–2), pp. 215–224.

[210] Rahaman, M. N., 2003, *Ceramic Processing and Sintering*, CRC Press, New York.

[211] Morikawa, H., Minato, I., Tomita, T., and Iwai, S., 1975, "Anhydrite: A Refinement," Acta Crystallogr., **B31**, pp. 2164–2165.

[212] Wang, P. Y., Li, H. J., Qi, L. H., Zeng, X. H., and Zuo, H. S., 2011, "Synthesis of Al-

TiAl3compound by Reactive Deposition of Molten Al Droplets and Ti Powders," Prog. Nat. Sci. Mater. Int., **21**(2), pp. 153–158.

[213] Yang, R. Y., Zou, R. P., and Yu, A. B., 2000, "Computer Simulation of the Packing of Fine Particles," Phys. Rev. E, **62**(3), pp. 3900–3908.

[214] Litster, J. D., and Ennis, B. J., 2004, *The Science and Engineering of Granulation Process*, Springer Science, Dordrecht.

[215] Stuer, M., Zhao, Z., and Bowen, P., 2012, "Freeze Granulation: Powder Processing for Transparent Alumina Applications," J. Eur. Ceram. Soc., **32**(11), pp. 2899–2908.

[216] Saluja, V., Amorij, J. P., Kapteyn, J. C., de Boer, A. H., Frijlink, H. W., and Hinrichs, W. L. J., 2010, "A Comparison between Spray Drying and Spray Freeze Drying to Produce an Influenza Subunit Vaccine Powder for Inhalation," J. Control. Release, **144**(2), pp. 127–133.

[217] Du, W., Miao, G., Liu, L., Pei, Z., and Ma, C., 2019, "Binder Jetting Additive Manufacturing of Ceramics: Feedstock Powder Preparation by Spray Freeze Granulation," *ASME 2019 14th International Manufacturing Science and Engineering Conference*, Errie, PA, pp. 1–6.

[218] Du, W., Miao, G., Liu, L., Pei, Z., and Ma, C., 2019, "Binder Jetting Additive Manufacturing of Ceramics: Comparison of Flowability and Sinterability between Raw and Granulated Powders," *ASME 2019 14th International Manufacturing Science and Engineering Conference*, Errie, PA, pp. 1–8.

[219] Stovall, T., de Larrard, F., and Buil, M., 1986, "Linear Packing Density Model of Grain Mixtures," Powder Technol., **48**(1), pp. 1–12.

[220] Mühler, T., Gomes, C. M., Heinrich, J., and Günster, J., 2015, "Slurry-Based Additive

Manufacturing of Ceramics," Int. J. Appl. Ceram. Technol., **12**(1), pp. 18–25.

[221] Hu, K., Wei, Y., Lu, Z., Wan, L., and Li, P., 2018, "Design of a Shaping System for Stereolithography with High Solid Loading Ceramic Suspensions," 3D Print. Addit. Manuf., **5**(4), pp. 311–318.

[222] Mamatha, S., Biswas, P., Ramavath, P., Das, D., and Johnson, R., 2018, "3D Printing of Complex Shaped Alumina Parts," Ceram. Int., **44**(16), pp. 19278–19281.

[223] Breval, E., Cheng, J. P., Agrawal, D. K., Gigl, P., Dennis, M., Roy, R., and Papworth, A. J., 2005, "Comparison between Microwave and Conventional Sintering of WC/Co Composites," Mater. Sci. Eng. A, **391**(1–2), pp. 285–295.

[224] Barsoum, M. W., 2002, *Fundamentals of Ceramics*, CRC Press, New York.

[225] Ainsley, C., and Gong, H., 1999, "Precision Sintering of Slip Cast Components," J. Mater. Process. Technol., **95**(1–3), pp. 201–209.

[226] Grant, L. O., Alameen, M. B., Carazzone, J. R., Fred, C., Iii, H., and Cordero, Z. C., 2018, "Mitigating Distortion During Sintering of Binder Jet Printed Ceramics," *Solid Freeform Fabrication Symposium*, Austin, TX, pp. 135–142.

[227] Vermeiren, E., 2002, "The Advantages of All-Round Pressure," Met. Powder Rep., **57**(2), pp. 18–21.

[228] Koizumi, M., and Nishihara, M. (Masao), 1991, *Isostatic Pressing: Technology and Applications*, Springer Science & Business Medi, New York.

[229] Balakrishnan, A., Pizette, P., Martin, C. L., Joshi, S. V., and Saha, B. P., 2010, "Effect of Particle Size in Aggregated and Agglomerated Ceramic Powders," Acta Mater., **58**(3), pp. 802–812.

[230] Boltachev, G. S., and Volkov, N. B., 2010, "Size Effect in Nanopowder Compaction,"

Tech. Phys. Lett., **36**(9), pp. 823–826.

[231] “ExOne | ACT Whitepaper” [Online]. Available: https://www.exone.com/en-US/ExOne-Triple-ACT-Whitepaper. [Accessed: 18-Jan-2020].

3. MIXING POWDERS OF DIFFERENT SIZES: EFFECT OF PARTICLE SIZE DISTRIBUTION ON DENSITY IN BINDER JETTING ADDITIVE MANUFACTURING*

3.1. Introduction

Additive manufacturing (AM), also known as 3D printing, can be described as a process of joining materials with a primary objective of making objects from 3D model data using a layer-by-layer principle [1,2]. Binder jetting is one of the most advantageous technologies to produce large complex-shaped parts due to its capability of processing various materials [3–5], no need for explicit support structure [6], and high scalability [7,8]. Since the first paper on binder jetting [9], a number of studies have been reported on processing of different materials such as ceramics [3] and metals [4], and fabrication of different products such as load-bearing parts [10–13] and biomedical parts [14–16].

The particle size distribution of feedstock powder affects the powder packing density and the sintered density [17]. Particle size distribution can be tuned by mixing different-sized powders. For example, Sun et al. studied the effects of particle size distribution on the bulk density of sintered samples [18]. Glass-ceramic powders with two size ranges (45–100 μm and 0–25 μm) were mixed in fractions of 90:10, 80:20, 70:30, and 60:40, respectively. The mixture with the fraction of 60:40 achieved the highest sintered density of 1.60 g/cm^3. Bai et al. also investigated the effect of particle size distribution [19]. A bimodal mixture from powders with particle sizes of 30 and 5 μm and a mixing ratio of 73:27 achieved an improved tap density (by 8.3%) and green density (by ~8%) compared with those from the component powder with a particle size of 5 μm. However, no research has been done to investigate the theoretically achievable packing density by

*Reprinted with permission from "Binder Jetting Additive Manufacturing: Effect of Particle Size Distribution on Density" by Du, W., Roa, J., Hong, J., Liu, Y., Pei, Z., and Ma, C., 2021. Journal of Manufacturing Science and Engineering, 143(9), p. 091002 (9 pages), Copyright [2021] by ASME.

mixing different-sized powders and compare it with experimentally obtained results. This work aims to fill this knowledge gap.

Particle packing is of interest in many fields, such as civil engineering [20]. For a mixture of different-sized component powders, analytical models have been developed to predict the mixture packing density using the size, volume fraction, and packing density of each component powder. Compared with numerical methods such as the discrete element method, an analytical method has its own advantages such as low computational cost and explicit solutions [21]. The linear packing model, proposed by Stovall et al. [22], is one of the most popular analytical models [23,24].

The objective of this research is to examine the effects of particle size distribution on density of a densely packed powder, powder bed density, and sintered density with both analytical and experimental methods. Firstly, the analytical linear packing model was employed to study the effects of various parameters (mixing fraction, component particle size ratio, and component packing density ratio) on the mixture packing density. Afterward, the analytical model was used to predict the mixture packing density from selected component powders (70, 10, and 2 μm powders) under the ideal conditions (i.e., the state of dense packing). Afterward, experimental studies were conducted to evaluate the actual conditions. Tap density, powder bed density, and sintered density of each component and mixture were measured and compared with the analytical results. Although ceramic is selected as the model material and binder jetting is selected as the model AM technology, this method of mixing different-sized powders maintains its potentiality for other materials (such as metals and composites) and other AM technologies (such as powder bed fusion).

3.2. Analytical Method

The analytical linear packing model assumes that all component powders and mixtures are composed of non-deformable particles under the state of dense packing [22]. In the case of a mixture with *n* component powders (the component powders are ranked such that $d_i \geq d_{i+1}$, where d_i is the diameter of the *i*th component), the mixture packing density is given by [16]

$$\gamma = \min(\gamma_1, \gamma_2, \cdots, \gamma_n) \tag{1}$$

where γ_i is a specific mixture packing density when the *i*th component is "dominant" [22] and given by

$$\gamma_i = \frac{\beta_i}{1 - \sum_{j=1}^{i-1}\left[1 - \beta_i + b_{i,j}\beta_i\left(1 - \frac{1}{\beta_j}\right)\right]y_j - \sum_{j=i+1}^{n}\left[1 - a_{i,j}\frac{\beta_i}{\beta_j}\right]y_j} \tag{2}$$

where β_i and y_i are the packing density and volume fraction of the *i*th component, respectively, and $a_{i,j}$ and $b_{i,j}$ are interaction functions which are called loosening and wall effect parameters, respectively. In the linear packing model, the loosening effect is referred to as a phenomenon that fine particles loosen the packing of coarse particles when squeezing themselves into the space that is near the contact point between two coarse particles and making coarse particles more dispersed. The wall effect describes how coarse particles disrupt the packing of fine particles at wall-like boundaries of coarse particles [23]. Both these effects decrease the packing density. Interaction functions derived from a curve fitting of experimental results by de Larrard [24] are

$$a_{i,j} = \sqrt{1 - \left(1 - \frac{d_j}{d_i}\right)^{1.02}} \tag{3}$$

$$b_{i,j} = 1 - \left(1 - \frac{d_j}{d_i}\right)^{1.5} \tag{4}$$

3.2.1. Parametric study on binary mixing

3.2.1.1. Effect of mixing fraction on mixture packing density

Mixing fraction is an important parameter that affects the mixture packing density. In a binary mixing, the mixing fraction can be described with the volume fraction of either the coarse or fine powder, y_1 or y_2 in Equation (2). In the parametric study on binary mixing, the coarse powder fraction was used, which was varied from 0 vol.% to 100 vol.% (corresponding to 100 vol.% to 0 vol.% for the fine powder fraction) with an increment of 0.01 vol.%. The component particle size ratio, d_2/d_1 in Equations (3) and (4), was set as 0.1. The packing density of both the coarse and fine raw powders, β_1 and β_2 in Equation (2), was set to 63.7%. This packing density value is common for a densely packed powder [25,26].

3.2.1.2. Effect of component particle size ratio on mixture packing density

The effect of component particle size ratio (fine to coarse), d_2/d_1 in Equations (3) and (4), was studied by varying it from 1/2, 1/4, 1/8, 1/16, to 1/32. This parametric study was performed over the full range of the coarse powder fraction, i.e., 0 vol.% to 100 vol.% with an increment of 0.01 vol.%. The packing density of both coarse and fine raw powders, β_1 and β_2 in Equation (2), was set to 63.7%.

3.2.1.3. Effect of component packing density ratio on mixture packing density

Component packing density of coarse and fine raw powders, β_1 and β_2 in Equation (2), respectively, is another important parameter that affects the mixture packing density. To simplify the analysis, a component packing density ratio (fine to coarse) was defined, β_2/β_1. The coarse powder packing density (β_1) was set to 63.7%. The component packing density ratio was varied from 0.5 to 1.0 by changing the fine powder packing density (β_2) accordingly. This parametric study was performed over the full range of the coarse powder fraction, i.e., 0 vol.% to 100 vol.% with an increment of 0.01 vol.%. The component particle size ratio (d_2/d_1) was set to 1/3.

3.2.1.4. Relationship between critical component packing density ratio and component particle size ratio

Component particle size ratio could have double-edged effects on the mixture packing density. A smaller component particle size ratio could strengthen the filling effect of the fine powder and thus lead to a higher mixture packing density. However, a smaller component particle size ratio is usually associated with a lower packing density of the fine powder given the same coarse powder, which could lead to a lower mixture packing density. Therefore, the effectiveness of the mixing method, i.e., whether it improves the packing density, depends on the component packing density ratio. Given a component particle size ratio, if the component packing density ratio is below a certain threshold, defined as the critical component packing density ratio, the mixing method does not improve the packing density, regardless of the mixing fraction. The objective of this parametric study is to determine the relationship between the critical component packing density ratio and the component particle size ratio. In this study, the packing density of the coarse powder (β_1) was set to 63.7%.

3.2.1.5. Optimal mixing fraction and maximum mixture packing density

Lastly, the model was used to predict the optimal mixing fraction and the maximum mixture packing density. In this study, the component particle size ratio was varied from 0.001 to 0.5 with an increment of 0.0005. The component packing density ratio was varied from 0.5 to 1.0 with an increment of 0.1.

3.2.2. Case study on ternary mixing

Due to the large number of parameters involved in ternary mixing than in binary mixing, ternary mixing was analytically investigated as a case study for the powders used in the experiments. Tap density of the selected component powders were measured (described in Section

3.3) and used as the inputs of the analytical model. A ternary plot was used to illustrate the packing density values at all compositions.

3.3. Experimental Methods

3.3.1. Powder preparation

Three spherical alumina powders (Inframat, Manchester, CT) of different particle sizes (2, 10, and 70 μm, respectively) were selected as component powders. To prepare multimodal mixtures, the component powders were weighted using a balance with an accuracy of 0.1 mg (AGCN200, Torbal, Oradell, NJ) and mixed using ball milling (Jar Rolling Mills, Paul O. Abbe, Wood Dale, IL) with parameters listed in Table 1. Alumina balls, same as the powder material, were employed to avoid contamination. Small balls and low milling speed were used to avoid breaking the particles.

Table 3.1 Parameters used in ball milling

Parameter	Value
Ball-to-powder weight ratio	1:10
Ball diameter (mm)	2
Normalized mill rotation speed (%)	30
Milling time (h)	1

3.3.2. Characterization of powder morphology

The morphology of all component powders and mixtures was characterized using scanning electron microscopy (SEM, TESCAN VEGA II LSU, Brno-Kohoutovice, Czech).

3.3.3. Measurement of tap density

Tap density is considered as a good estimation for the density of a densely packed powder [27,28]. Tap density was measured by following an ASTM standard [29]. A tap density meter (DY-100A, Hongtuo, China) was used. In each measurement, 100 g of powder was tapped with a 3-mm stroke for 3000 cycles. After tapping, the powder mass was divided by the powder volume

to obtain the absolute tap density, which was then divided by the theoretical density of alumina (3.97 g/cm^3 [30]) to obtain the relative tap density.

3.3.4. Measurement of powder bed density

Powder bed density was determined by spreading ten layers of powder using a lab-designed setup (as shown in Figure 1) and measuring the mass and volume of the spread layers. This method has been widely used in other studies [31,32]. The layer thickness was 130 μm. The forward rotating roller had a diameter of 5 cm and a smooth glass surface. The process started with powder spreading with the roller. After one powder layer was spread, the lead screw was rotated to lower the build platform for another powder layer. No binder was applied in this measurement to avoid its interference with the measurement of powder bed density. The total height of the powder bed was measured by a caliper (with an accuracy of 10 μm). Afterward, all powder inside the chamber of the setup was carefully collected, and the mass of the collected powder was measured by a balance with an accuracy of 0.1 mg (AGCN200, Torbal, Oradell, NJ). The volume of the powder layers was calculated based on the inner diameter of the chamber and the total height of the powder bed. The total mass of the collected powder was divided by the total volume to obtain the powder bed density. This process was repeated three times for each powder.

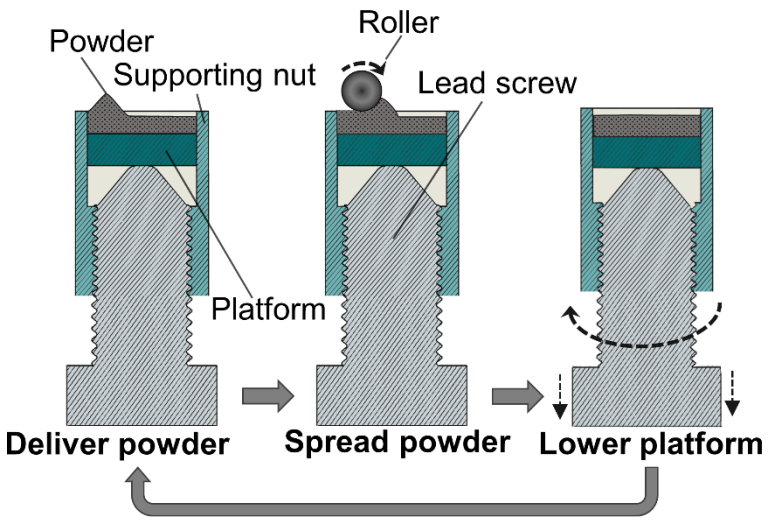

Figure 3.1 Powder spreading process with a lab-designed setup

3.3.5. Printing and sintering

Printing experiments were carried out using the lab-designed setup, as illustrated in Figure 2. The process started with powder spreading using the forward rotating roller with a diameter of 5 cm and a smooth glass surface to form the first foundation layer. Then the lead screw was rotated to lower the build platform. The layer thickness was 130 μm. Totally, two foundation layers were spread without jetting any binder. Afterward, the first powder layer for printing was spread, and then the powder bed was covered by a mask with an opening corresponding to the cross section of the desired shape, which was a circle with a diameter of 10 mm in this case. The printing binder was an aqueous solution containing 3 wt.% polyvinyl alcohol (molecule weight of 31,000), and 0.33 g of binder was applied for each powder layer. Then the mask was removed and the platform was lowered by a distance equal to the layer thickness (130 μm). This process was repeated until an entire disk-shaped green sample was printed. The print was repeated three times for each powder.

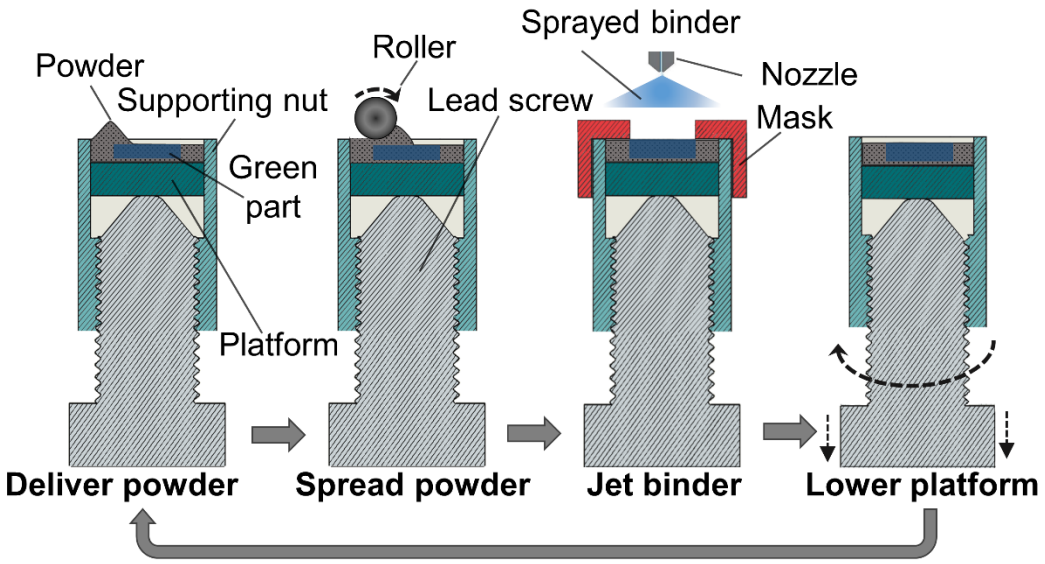

Figure 3.2 Binder jetting additive manufacturing process with a lab-designed setup

After printing, the samples were cured in a low-temperature furnace (KSL-1100X-S-UL-LD, MTI Corporation, Richmond, CA) at 200 °C for 2 h to evaporate the water in the binder and join the particles. After cooling, the green samples were carefully extracted from the powder bed and placed in a high-temperature furnace (KSL-1700X-A2-UL, MTI Corporation, Richmond, CA) for debinding and sintering. The furnace temperature was increased to 350 °C at a ramp-up rate of 5 °C/min, followed by debinding from 350 °C to 550 °C at a ramp-up rate of 1 °C/min. Then the samples were heated up to 1600 °C at 5 °C/min and sintered for 2 h, followed by cooling to the room temperature. All these post-processing procedures were performed in air.

3.3.6. Measurement of sintered density

Density of sintered samples was measured with the Archimedes' method. After a dry mass (m_d) measurement, each sample was carefully lowered onto a pan suspended in a beaker of deionized water to determine its wet mass (m_w). The mass measurements were done using a balance with an accuracy of 0.1 mg (AGCN200, Torbal, Oradell, NJ). The dry and wet masses were then used to calculate the density of the samples using the following equation:

$$\rho_{sp} = \rho_{wt} \frac{m_d}{m_d - m_w} \quad (5)$$

where ρ_{sp} is the sintered density and ρ_{wt} is the water density at the experimental temperature. If a sample has a high porosity, the water infiltrates the sample and thus the above method overestimates the density. Therefore, all samples were coated with an extremely thin layer of wax to prevent the water from infiltrating the samples.

3.3.7. Characterization of sintered microstructure

The microstructure of sintered samples was characterized using SEM (TESCAN VEGA II LSU, Brno-Kohoutovice, Czech).

3.4. Analytical Results and Discussion

3.4.1. Parametric study on binary mixing

3.4.1.1. Effect of mixing fraction on mixture packing density

The modeling results of the effect of mixing fraction are shown in Figure 3. The mixture packing density increases first and then decreases as the coarse powder fraction increases. A maximum value of the mixture packing density (i.e., maximum mixture packing density) exists for a certain coarse powder fraction (i.e., the optimal fraction of coarse powder). This trend can be explained from the perspective of either the fine powder or the coarse powder. On one hand, the increase of the fine powder fraction (from right to left for the X-axis in Figure 3) lets more fine particles fill into the voids among the coarse particles and consequently increases the packing density, which is the so-called filling effect of the fine powder [22,33]. However, after all voids are filled, the introduction of more fine particles decreases the packing density due to the loosening effect of the fine powder [22,33]. On the other hand, the increase of the coarse powder fraction (from left to right for the X-axis in Figure 3) allows a single coarse particle to replace multiple fine particles and completely fill the voids among them, consequently increasing the packing density,

which is the so-called occupying effect of the coarse powder [22,33]. However, after available voids are occupied by coarse particles, the packing density decreases due to the wall effect of the coarse powder [22,33].

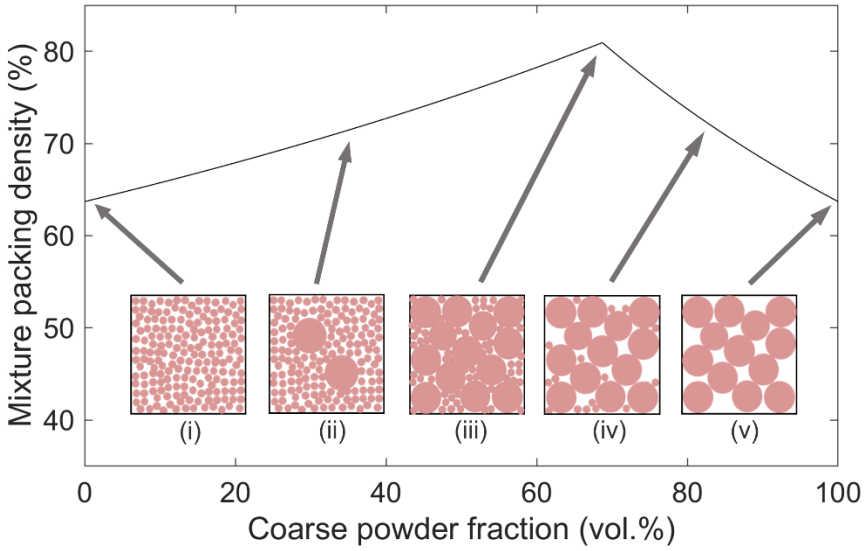

Figure 3.3 Bimodal mixture packing density dependent on coarse powder fraction when the component particle size ratio is 0.1 and the packing density of the fine and coarse powders is 63.7%

3.4.1.2. Effect of component particle size ratio on mixture packing density

The modeling results of the effect of component particle size ratio are shown in Figure 4. For the same coarse powder fraction in Figure 4, a smaller particle size ratio leads to a larger mixture packing density. As the particle size ratio decreases (i.e., the fine particles become smaller considering the same coarse powder), the fine particles have less geometric constrain and thus can fill more space among the coarse particles (e.g., near the contact point between two coarse particles).

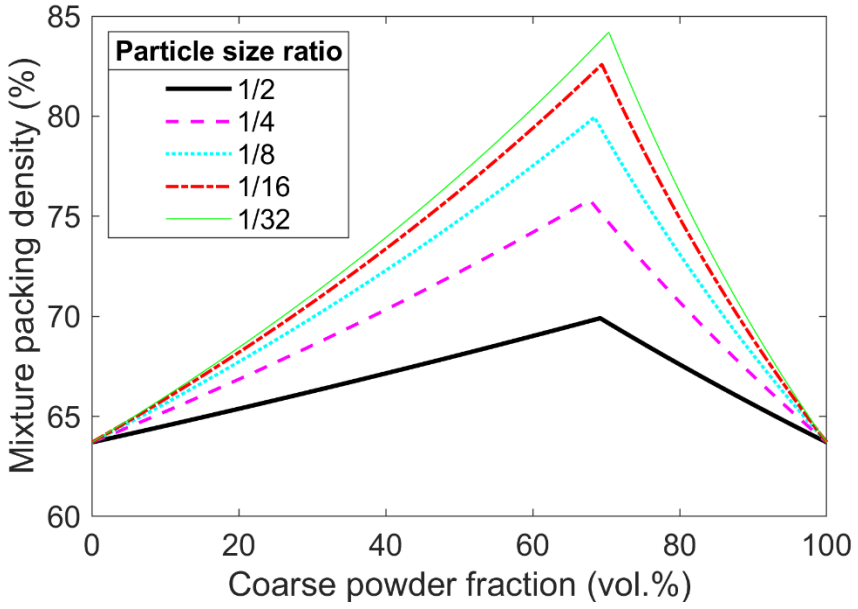

Figure 3.4 Bimodal mixture packing density dependent on component particle size ratio when the packing density of the fine and coarse powders is 63.7%

3.4.1.3. Effect of component packing density ratio on mixture packing density

The modeling results of the effect of component packing density ratio are illustrated in Figure 5. Since the fine powder packing density is varied while the coarse powder packing is kept at the same, all curves have different starting points but the same ending point. When the packing density ratio decreases, the mixture packing density decreases. This is because fewer fine particles can be inserted into the voids among the coarse particles.

Interestingly, when the packing density ratio is low (i.e., 0.5), the mixture packing density increases monotonically as the coarse powder fraction increases (i.e., as the fine powder fraction decreases). It means that when the fine powder packing density is too low, adding any amount of fine powder into the coarse powder will loosen its packing.

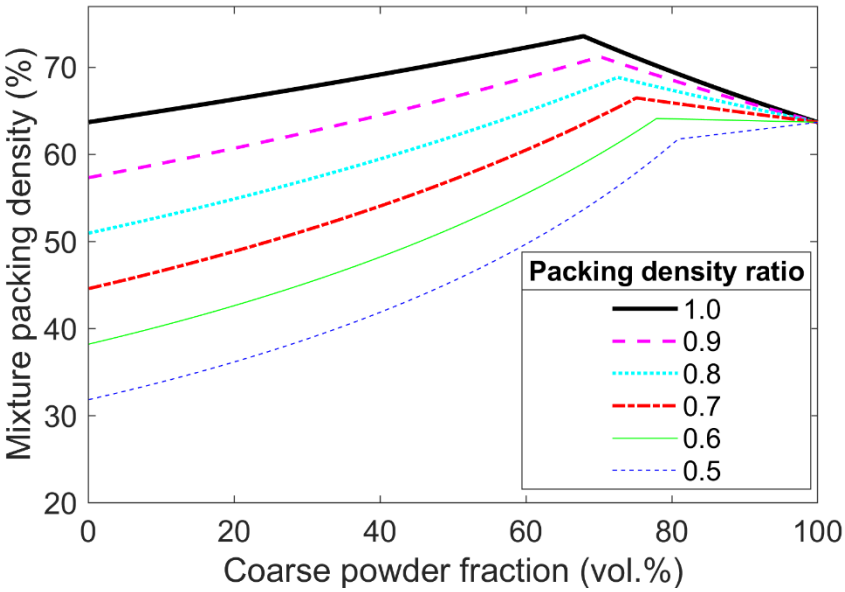

Figure 3.5 Bimodal mixture packing density dependent on component packing density ratio when the component particle size ratio is 1/3

3.4.1.4. Relationship between critical component packing density ratio and component particle size ratio

The relationship between the critical component packing density ratio and the component particle size ratio is shown in Figure 6. Before mixing, this figure can be used to determine if the mixing method improves the packing density in comparison with the coarse powder, given a combination of particle size ratio and packing density ratio. After measuring the packing densities and particle sizes of two component powders, a point in Figure 6 can be located. Depending on whether the point is located to the left or right of the curve, it can be determined whether the mixing method improves the packing density or not.

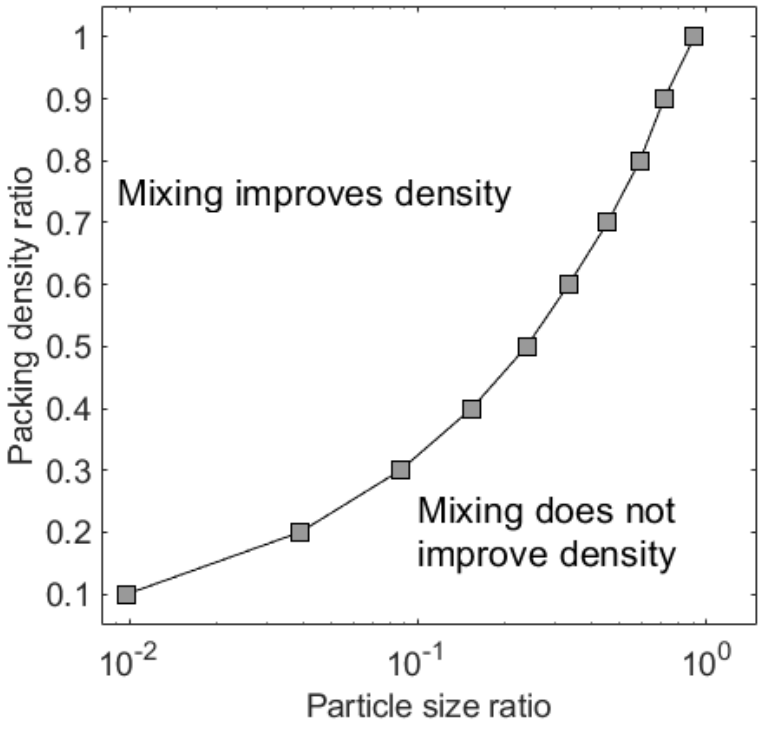

Figure 3.6 Relationship between critical component packing density ratio and component particle size ratio

3.4.1.5. Optimal mixing fraction and maximum mixture packing density

The dependence of the optimal fraction of coarse powder on the component particle size ratio and packing density ratio is shown in Figure 7(a). The optimal fraction of coarse powder decreases as the packing density ratio increases. This is due to the higher packing density of the fine powder and consequently more fine particles that can be packed into the voids among coarse particles, leading to the decrease of the optimal fraction of coarse powder.

In Figure 7(a), although all curves follow a similar overall trend, the optimal fraction of coarse powder behaves slightly differently between the small (0.5–0.7) and large (0.8–1.0) component packing density ratios at a high (0.25–0.5) component particle size ratio. At a small packing density ratio and a high particle size ratio, the optimal fraction is 100 vol.%. This means the coarse powder has a higher packing density than any bimodal mixture. It further indicates that the mixing method

does not improve the packing density if the fine powder has a similar particle size but a lower packing density than the coarse powder, which agrees with the results in Figure 6.

The effects of the component particle size ratio and component packing density ratio on the maximum mixture packing density are illustrated in Figure 7(b). The maximum mixture packing density is a monotonically decreasing function of the particle size ratio. This is due to the more geometric constrain of the fine particles. For the same particle size ratio, the maximum mixture packing density increases as the packing density ratio increases. This is due to the higher packing density of the fine powder. Similar to Figure 7(a), the maximum mixture packing density is 63.7% when the particle size ratio is large (0.25–0.5) and the packing density ratio is small (0.5–0.7), indicating that mixing method does not improve the packing density under these conditions.

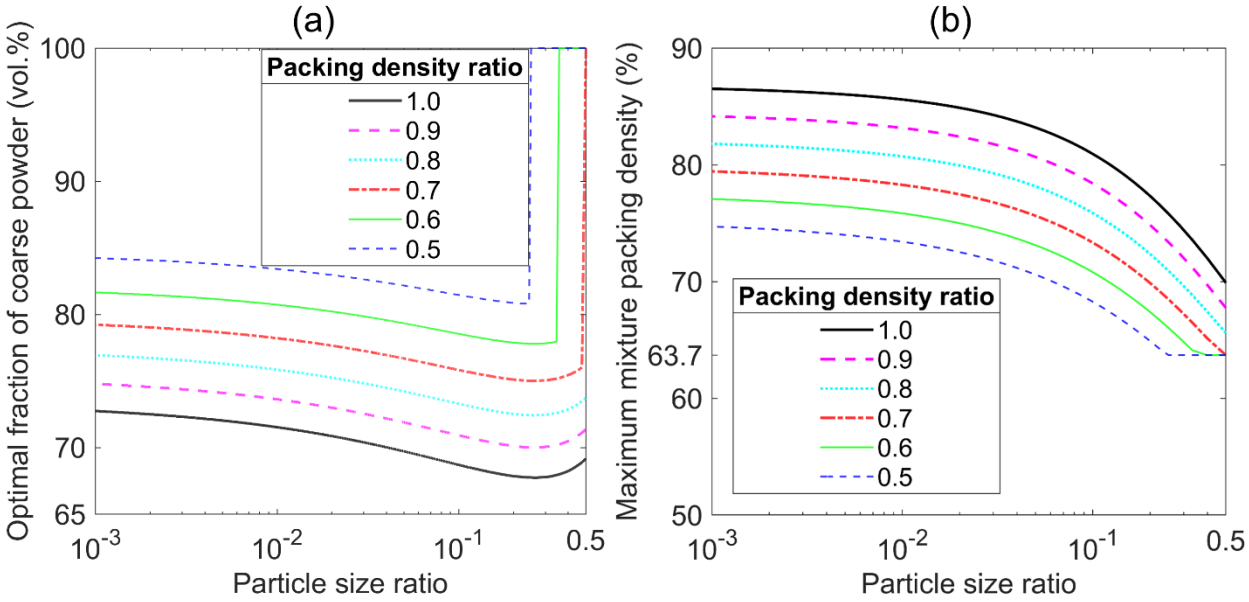

Figure 3.7 (a) Optimal fraction of coarse powder and (b) maximum mixture packing density of bimodal mixture dependent on component particle size ratio and packing density ratio

3.4.2. Case study on ternary mixing

Tap density of three component powders is listed in Table 2. The fine powders (10 μm and 2 μm) have a slightly lower tap density than the coarse powder (70 μm) because they have higher inter-particle cohesion [27], which makes them slightly more difficult to be densely compacted.

Table 3.2 Tap density of component powders

Powder particle size (μm)	Absolute tap density (g/cm^3)	Relative tap density (%)
70	2.47	62.2
10	2.42	61.0
2	2.42	61.0

Figure 8 shows a ternary plot containing the modeled packing density of bimodal (i.e., 10/2, 70/10, 70/2) and trimodal (i.e., 70/10/2) mixtures. Each point in the ternary plot represents a composition of the three component powders. The left, right and bottom sides are volume fractions of the component powders of 70 μm, 10 μm, and 2 μm, respectively. The left, right and top vertexes represent the full fraction (100 vol.%) for the component powders of 2 μm, 10 μm, and 70 μm, respectively. Fractions for a specific mixture can be determined by drawing a line through the mixture point parallel to the opposite side of component vertex and intersecting the component axis. The trimodal mixture that achieves the highest packing density is marked as a dot inside the plot as an example. The fraction of the 70-μm powder is determined by drawing a parallel line to the bottom side. The intersection of the left side and the parallel line is the fraction, which is 61.3 vol.%. Similarly, the fractions of 10-μm and 2-μm component powders are determined, which are 21.1 vol.% and 17.6 vol.%, respectively. Moreover, three sides of the triangle represent three bimodal mixtures (i.e., trimodal mixtures with a zero fraction of the corresponding vertex component), and their modeled results are plotted along the sides. The bimodal mixtures that achieve the highest packing densities are also marked as red dots. The optimal mixing fraction and the maximum packing density for the bimodal and trimodal mixtures are listed in Table 3.

The packing density of a trimodal mixture has a similar dependence on the mixing faction to that of a bimodal mixture (increases first and then decreases) if one component fraction is kept constant and the other two component fractions are varied, as shown by the grey dashed lines inside the ternary plot in Figure 8. Furthermore, a trimodal mixture does not always have a higher packing density than a bimodal mixture. For example, the trimodal mixtures near the three corners of the ternary plot have a lower packing density than the three dots on the edges. However, it can be concluded that the multimodal mixture always has a higher packing density than at least one of its component powders. In a proper mixing fraction range, the packing density of the multimodal mixture is higher than that of any of its component powders.

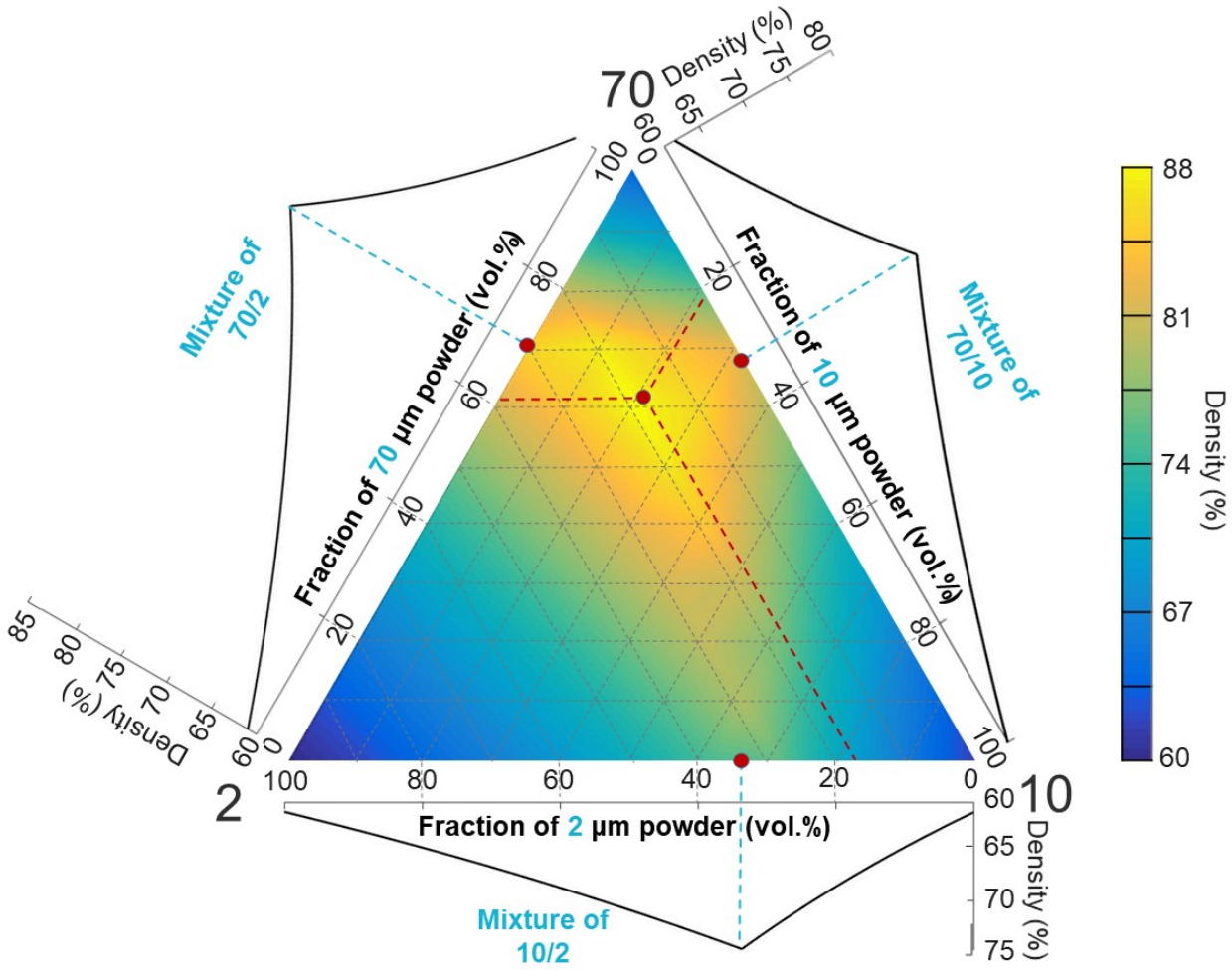

Figure 3.8 Modeled trimodal mixture packing density dependent on fractions of three component powders (70, 10, and 2 µm)

Table 3.3 Analytical results from case study

Bimodal or trimodal mixture	Optimal mixing fraction (vol.%)	Maximum mixture packing density (%)
10/2	66.3:33.7	74.8
70/10	67.7:32.3	77.4
70/2	70.0:30.0	82.6
70/10/2	61.3:21.1:17.6	85.7

3.5. Experimental Results and Discussion

3.5.1. Powder morphology

Figure 9 shows the particle morphology of three component powders. The shapes are primarily spherical, and the sizes are not perfectly uniform. In this paper, the average sizes were used since the size variation within each component powder was much smaller than the differences across these three component powders.

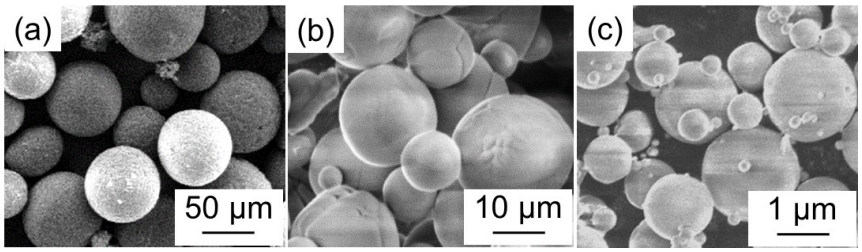

Figure 3.9 Micrographs of component powders: (a) 70 μm, (b) 10 μm, and (c) 2 μm

Figure 10 shows the SEM images of four multimodal mixtures whose compositions are listed in Table 3. The fine particles can be found in the voids among the coarse particles.

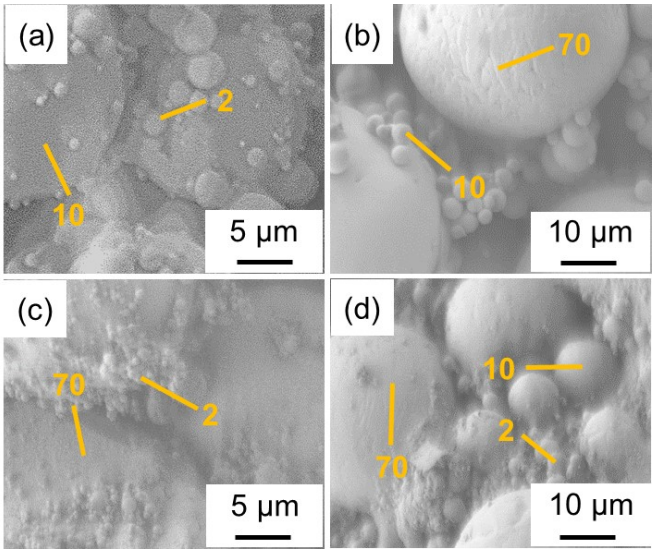

Figure 3.10 Micrographs of multimodal mixtures: (a) 10/2, (b) 70/10, (c) 70/2, and (d) 70/10/2

3.5.2. Tap density

The tap density results of three bimodal mixtures with different mixing fractions are shown in Figure 11. The trend from the experimental results agrees well with that from the analytical prediction in Figure 3. As the coarse powder fraction increases, the tap density increased first and

then decreased. It can also be concluded that a smaller component particle size ratio leads to a larger mixture tap density, which agrees with the analytical prediction in Figure 4.

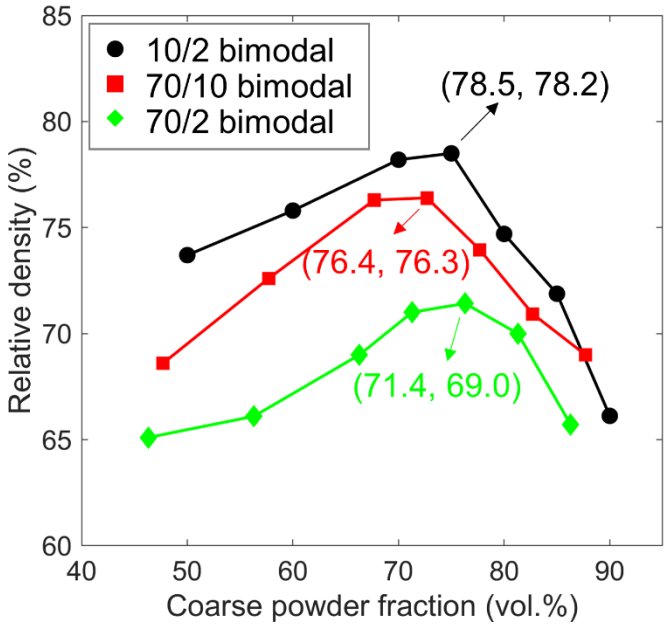

Figure 3.11 Experimental results of tap density for bimodal mixtures

Figure 12 shows the interpolation of the tap density for the trimodal (and bimodal) powders (marked as dots). Approaches to determining the mixing fractions for a specific point on the plot are descripted in Section 4.2. The overall trend from the experimental results agrees well with that from the analytical prediction in Figure 8. When one component fraction is unchanged and the other two are varied, the tap density of the trimodal mixture shows a similar trend as that of bimodal mixture. For example, when the fraction of 10 μm powder is maintained at 20 vol.% and the fraction of 70 μm powder increased from 40 vol.% to 50 vol.% and then to 60 vol.%, the tap density increased from 75.3% to 79.0% and then decreased to 78.2%. The maximum tap density from all tested trimodal mixtures is 81.6%, which is larger than that of all bimodal mixtures.

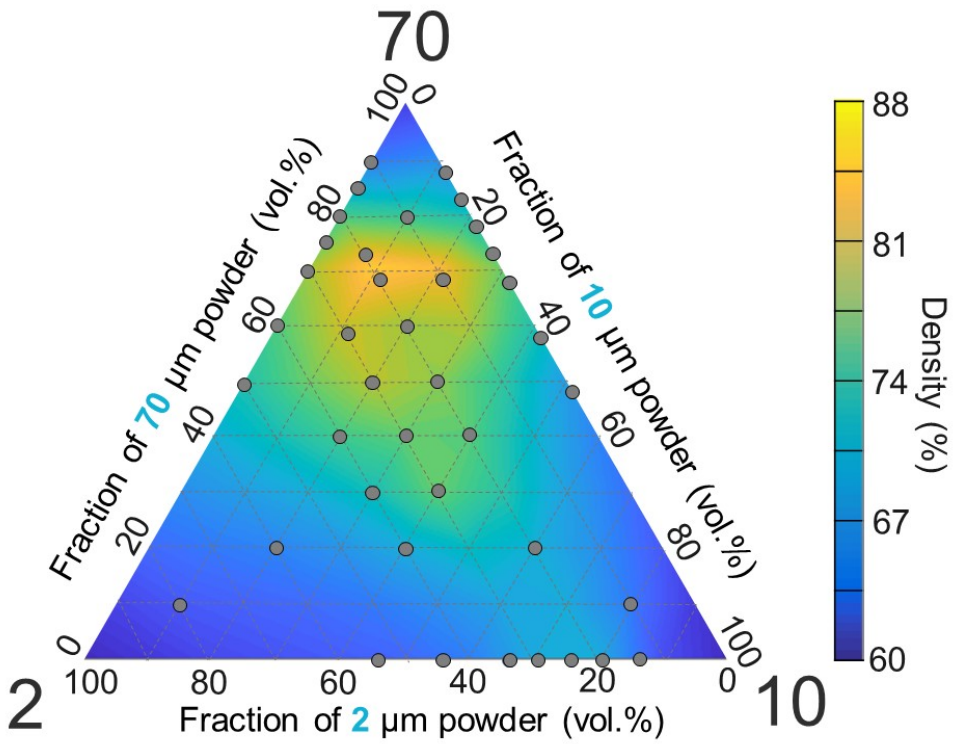

Figure 3.12 Tap density of trimodal (and bimodal) mixtures at different fractions of three component powders (70, 10, and 2 µm)

Figure 13 shows the deviation of the bimodal mixture packing density predicted by the analytical model from the experimentally measured tap density. For each bimodal mixture, the deviation has relatively large positive values at a low coarse powder fraction, indicating an overestimation by the analytical model. A possible reason is the effect of the fine powder, which is more loosely packed after tapping. As the coarse powder fraction increases, the effect of the fine powder becomes less significant, leading to smaller deviation values.

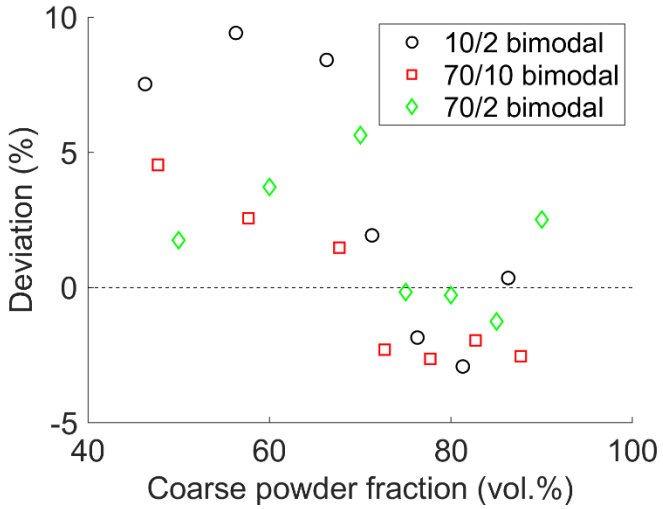

Figure 3.13 Deviation of bimodal mixture packing density predicted by the analytical model from measured tap density

Similarly, Figure 14 shows the deviation of predicted mixture packing density from the experimentally measured tap density for the trimodal mixture. Approaches to determining the mixing fractions for a specific point on the plot are descripted in Section 4.2. The ternary plot shows a large portion area of red (i.e., dark) color, indicating that the analytical results are larger than those of the experimental ones. The area close to the bottom line (i.e., mixtures with a relatively small fraction of 70-μm powder and a relatively large fraction of 2-μm powder) shows higher deviation values than other areas.

The mismatch associated with the fine powders (powders with particle sizes of 10 and 2 μm) may be because the analytical model does not consider inter-particle cohesion and satellite particles. In this case, the discrete element method will be advantageous due to its microscopic nature [21]. This method will be considered in the future work.

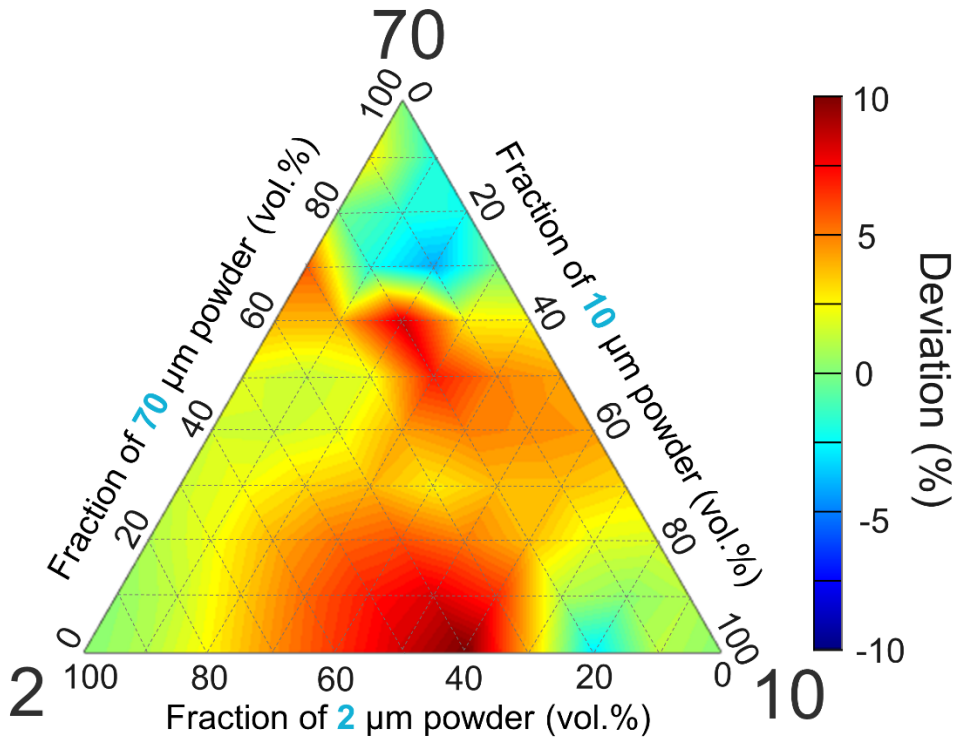

Figure 3.14 Deviation of trimodal mixture packing density predicted by the analytical model from measured tap density

3.5.3. Powder bed density and sintered density

Powder bed density and sintered density for different component powders and multimodal mixtures are shown in Table 4 and Figure 15. Standard deviation for the sintered density of 70-µm powder is not shown because the samples were very brittle after sintering and only one sample was available for the density measurement. The powder bed density achieved by multimodal mixtures is higher than that by their component powders in most cases. There are two exceptions: (1) the powder bed density of the 70/10 bimodal mixture is lower than that of 70-µm powder and (2) the powder bed density of the 10/2 bimodal mixture is lower than that of 10-µm powder. A possible reason is that the reduced flowability of the mixtures led to a nonuniform spreading of the powder bed and consequently a lower powder bed density. The trimodal mixture achieves the

largest powder bed density (60.1%) among all of the investigated powders and mixtures. However, the powder bed density is still lower than the tap density.

Sintered density achieved by multimodal mixtures is higher than that by their corresponding component powders in most cases. Although sintering improved the density, the finally achieved density was still significantly lower than the full density. A reason is that the powder bed density is far below the modeled packing density and the tap density. It indicates that the powder spreading process could be significantly improved to reach the ideal case. It also means that new models are needed to directly model the powder spreading process and predict the powder bed density, for example, with the discrete element method. Another reason could be that these powders have a low sinterability.

Table 3.4 Mixing fraction, powder bed density, and sintered density

Powder or mixture	Mixing fraction (vol.%)	Powder bed density (%)	Sintered density (%)
2	/	39.7 ± 0.9	46.8 ± 1.0
10	/	51.1 ± 0.7	57.5 ± 0.3
70	/	58.2 ± 0.7	60.5
10/2	66.3:33.7	45.2 ± 0.9	50.7 ± 0.9
70/10	67.7:32.3	53.6 ± 1.2	64.8 ± 0.8
70/2	70.0:30.0	59.5 ± 0.9	64.3 ± 3.7
70/10/2	61.3:21.1:17.6	60.1 ± 0.1	66.1 ± 0.8

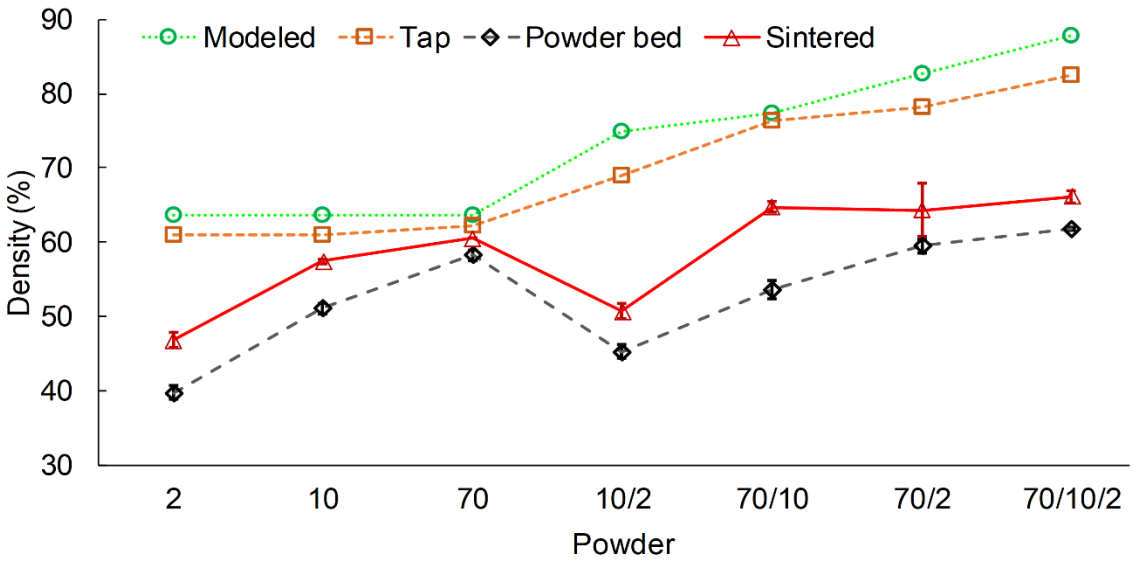

Figure 3.15 Various densities achieved by component powders and multimodal mixtures

3.5.4. Sintered microstructure

Figures 16 and 17 show the microstructure of sintered samples from component powders and multimodal mixtures, respectively. In a multimodal mixture, the voids among coarse particles are filled with fine particles, which has increased the powder bed density and the sintered density. For example, in the case of the 70/10/2 trimodal mixture, the 10-µm particles fill the voids among the 70-µm particles and 2-µm particles fill the remaining voids between 70-µm and 10-µm particles, which has led to the highest powder bed density and sintered density among all powders in this work.

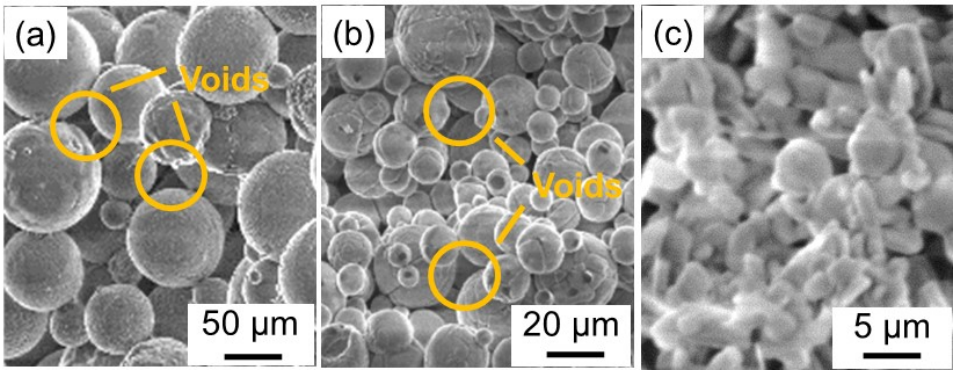

Figure 3.16 Microstructure of sintered samples from component powders: (a) 70 μm, (b) 10 μm, and (c) 2 μm.

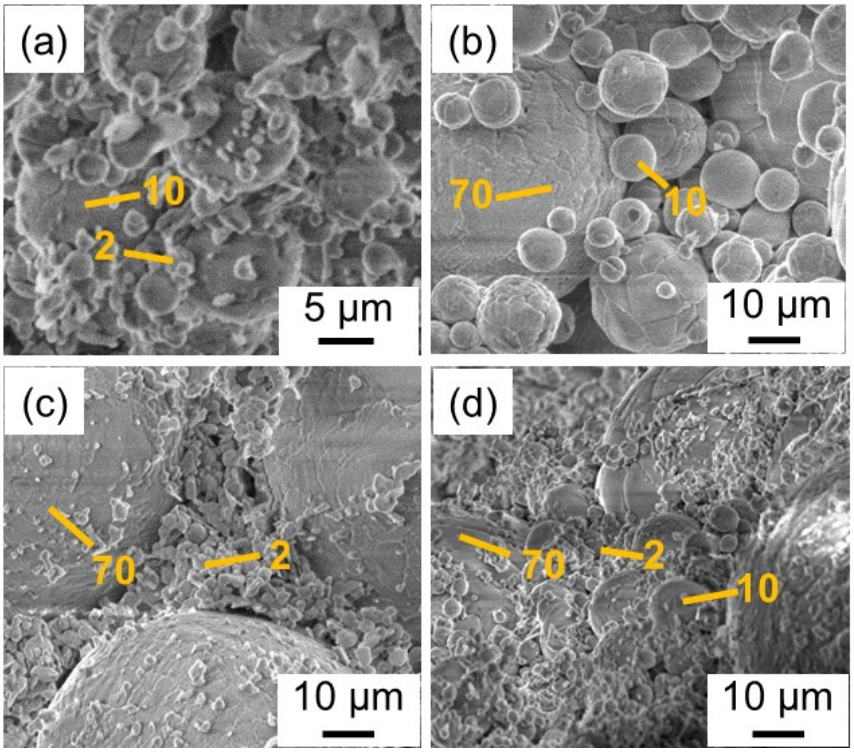

Figure 3.17 Microstructure of sintered samples from multimodal mixtures: (a) 10/2, (b) 70/10, (c) 70/2, and (d) 70/10/2.

3.6. Conclusions

This work investigated the effects of particle size distribution on density of a densely packed powder, powder bed density, and sintered density in binder jetting. Analytical results showed that there existed an optimal mixing fraction to achieve the maximum mixture packing density. Both a lower component particle size ratio (fine to coarse) and a larger component packing density ratio

(fine to coarse) led to a larger maximum mixture packing density. Before mixing, the critical component packing density ratio can be used to decide whether the mixing method is effective. The dependence of the optimal mixing fraction and maximum mixture packing density on the component particle size ratio and component packing density ratio was plotted and can be used as theoretical tools to select parameters for the mixing method. Experimental results of tap density were consistent with the aforementioned analytical predictions. In addition, experimental measurements showed that the powder bed density and thus the sintered density were improved by multimodal mixtures compared with component powders in most cases. However, there is still large room to improve the powder bed density and thus the sintered density.

3.7. References

[1] ASTM International/International Standard, 2015, "ISO/ASTM 52900:2015 - Additive Manufacturing — General Principles — Terminology."

[2] Ziaee, M., and Crane, N. B., 2019, "Binder Jetting: A Review of Process, Materials, and Methods," Additive Manufacturing, **28**, pp. 781–801.

[3] Du, W., Ren, X., Pei, Z., and Ma, C., 2020, "Ceramic Binder Jetting Additive Manufacturing: A Literature Review on Density," Journal of Manufacturing Science and Engineering, **142**(4), p. 040801 (19 pages).

[4] Li, M., Du, W., Elwany, A., Pei, Z., and Ma, C., 2020, "Metal Binder Jetting Additive Manufacturing: A Literature Review," Journal of Manufacturing Science and Engineering, **142**(9), p. 090801 (17 pages).

[5] Ma, C., Pei, Z., Ren, X., and Du, W., 2019, "Hierarchical Compositions for the Additive Manufacturing of Materials."

[6] Miao, G., Du, W., Moghadasi, M., Pei, Z., and Ma, C., 2020, "Ceramic Binder Jetting

Additive Manufacturing: Effects of Granulation on Properties of Feedstock Powder and Printed and Sintered Parts," Additive Manufacturing, **36**, p. 101542.

[7] Zocca, A., Colombo, P., Gomes, C. M., and Günster, J., 2015, "Additive Manufacturing of Ceramics: Issues, Potentialities, and Opportunities," Journal of the American Ceramic Society, **98**(7), pp. 1983–2001.

[8] "ExOne | Binder Jetting Technology" [Online]. Available: https://www.exone.com/en-US/case-studies/what-is-binder-jetting. [Accessed: 21-Sep-2019].

[9] Sachs, E., Cima, M., and Cornie, J., 1990, "Three-Dimensional Printing: Rapid Tooling and Prototypes Directly from a CAD Model," CIRP Annals - Manufacturing Technology, **39**(1), pp. 201–204.

[10] Sachs, E., Cima, M., Williams, P., Brancazio, D., and Cornie, J., 1992, "Three Dimensional Printing: Rapid Tooling and Prototypes Directly from a CAD Model," Journal of Engineering for Industry, **114**(4), pp. 481–488.

[11] Díaz-Moreno, C. A., Lin, Y., Hurtado-Macías, A., Espalin, D., Terrazas, C. A., Murr, L. E., and Wicker, R. B., 2019, "Binder Jetting Additive Manufacturing of Aluminum Nitride Components," Ceramics International, **45**(11), pp. 13620–13627.

[12] Maleksaeedi, S., Eng, H., Wiria, F. E., Ha, T. M. H., and He, Z., 2014, "Property Enhancement of 3D-Printed Alumina Ceramics Using Vacuum Infiltration," Journal of Materials Processing Technology, **214**(7), pp. 1301–1306.

[13] Du, W., Ren, X., Ma, C., and Pei, Z., 2019, "Ceramic Binder Jetting Additive Manufacturing: Particle Coating for Increasing Powder Sinterability and Part Strength," Materials Letters, **234**, pp. 327–330.

[14] Miyanaji, H., Zhang, S., Lassell, A., Zandinejad, A. A., and Yang, L., 2016, "Optimal

Process Parameters for 3D Printing of Porcelain Structures," Procedia Manufacturing, **5**, pp. 870–887.

[15] Butscher, A., Bohner, M., Doebelin, N., Galea, L., Loeffel, O., and Müller, R., 2013, "Moisture Based Three-Dimensional Printing of Calcium Phosphate Structures for Scaffold Engineering," Acta Biomaterialia, **9**(2), pp. 5369–5378.

[16] Vorndran, E., Moseke, C., and Gbureck, U., 2015, "3D Printing of Ceramic Implants," MRS Bulletin, **40**(2), pp. 127–136.

[17] Moghadasi, M., Du, W., Li, M., Pei, Z., and Ma, C., 2020, "Ceramic Binder Jetting Additive Manufacturing: Effects of Particle Size on Feedstock Powder and Final Part Properties," Ceramics International, **46**(10), pp. 16966–16972.

[18] Sun, C., Tian, X., Wang, L., Liu, Y., Wirth, C. M., Günster, J., Li, D., and Jin, Z., 2017, "Effect of Particle Size Gradation on the Performance of Glass-Ceramic 3D Printing Process," Ceramics International, **43**(1), pp. 578–584.

[19] Bai, Y., Wagner, G., and Williams, C. B., 2017, "Effect of Particle Size Distribution on Powder Packing and Sintering in Binder Jetting Additive Manufacturing of Metals," Journal of Materials Science and Engineering, **139**(8), p. 081019 (6 pages).

[20] Kwan, A. K. H., Wong, V., and Fung, W. W. S., 2015, "A 3-Parameter Packing Density Model for Angular Rock Aggregate Particles," Powder Technology, **274**, pp. 154–162.

[21] Miao, G., Du, W., Pei, Z., and Ma, C., 2019, "Binder Jetting Additive Manufacturing of Ceramics: Analytical and Numerical Models for Powder Spreading Process," *ASME 2019 14th International Manufacturing Science and Engineering Conference, MSEC 2019*, American Society of Mechanical Engineers (ASME), Erie, PA, p. V001T01A002 (7 pages).

[22] Stovall, T., de Larrard, F., and Buil, M., 1986, "Linear Packing Density Model of Grain Mixtures," Powder Technology, **48**(1), pp. 1–12.

[23] Kwan, A. K. H., and Fung, W. W. S., 2009, "Packing Density Measurement and Modelling of Fine Aggregate and Mortar," Cement and Concrete Composites, **31**(6), pp. 349–357.

[24] de Larrard, F., 1999, *Concrete Mixture Proportioning: A Scientific Approach*, E & FN Spon, London.

[25] Scott, G. D., 1960, "Packing of Spheres: Packing of Equal Spheres," Nature, **188**(4754), pp. 908–909.

[26] German, R. M., 1989, *Particle Packing Characteristics*, Metal Powder Industries Federation, Princeton.

[27] Yu, A. B., Bridgwater, J., and Burbidge, A., 1997, "On the Modelling of the Packing of Fine Particles," Powder Technology, **92**(3), pp. 185–194.

[28] Abdullah, E. C., and Geldart, D., 1999, "The Use of Bulk Density Measurements as Flowability Indicators," Powder Technology, **102**(2), pp. 151–165.

[29] ASTM International, 2015, "B527-15: Standard Test Method for Tap Density of Metal Powders and Compounds."

[30] Rahaman, M. N., 2003, *Ceramic Processing and Sintering*, CRC Press, New York.

[31] Melcher, R., Travitzky, N., Zollfrank, C., and Greil, P., 2011, "3D Printing of Al2O3/Cu-O Interpenetrating Phase Composite," Journal of Materials Science, **46**(5), pp. 1203–1210.

[32] Gu, H., Gong, H., Dilip, J. J. S., Pal, D., Hicks, A., Doak, H., and Stucker, B., 2014, "Effects of Powder Variation on the Microstructure and Tensile Strength of Ti6Al4V Parts Fabricated by Selective Laser Melting," *Proceedings of the 25th Annual International*

Solid Freeform Fabrication Symposium, Austin, TX, pp. 470–483.

[33] Kwan, A. K. H., Chan, K. W., and Wong, V., 2013, "A 3-Parameter Particle Packing Model Incorporating the Wedging Effect," Powder Technology, **237**, pp. 172–179.

4. MIXING POWDERS OF DIFFERENT SIZES: PERFORMANCES OF THREE MODELS IN PREDICTING PACKING DENSITIES AND OPTIMAL MIXING FRACTIONS OF MIXTURES OF MICROPOWDERS WITH DIFFERENT SIZES

4.1. Introduction

Mixing powders with different sizes is a common method to prepare powders with multimodal particle size distributions. By controlling the particle sizes and mixing fractions of component powders, the powder mixtures can achieve different packing densities. Consequently, this method can be useful in various applications, such as to increase the powder bed density in additive manufacturing [1–3] and to decrease the porosity of concrete mixtures in construction engineering [4,5]. Instead of an trial and error approach to finding the mixing fractions to achieve the peak or a specific powder packing density, analytical models have been developed to predict the packing density of a powder mixture using certain information such as the size, fraction, and packing density of each component powder [6,7]. The original linear packing model was proposed by Stovall et al. [8]. Several enhanced linear packing models, such as de Larrard's [9], Yu's [10], and Kwan's models [11,12], were developed to improve the prediction performances by accounting for different particle effects.

Prediction performances of these models can be evaluated in terms of two aspects. The first is deviation of predicted density from measured density at different mixing fractions. It is useful when the model is used to guide the selection of mixing fractions to achieve a specific powder packing density. The second is deviation of predicted optimal mixing fraction from the mixing fraction for the measured peak powder packing density (i.e., peak density). It is useful when the model is used to guide the selection of optimal mixing fraction to achieve the peak density.

Table 1 lists several reported studies to compare the densities predicted by linear packing models against the densities measured experimentally. Kwan et al. [5] mixed four rock powders with particle size ranges of 75–150, 150–300, 300–600, and >600 μm, and then compared model-predicted packing densities (by de Larrard's and Yu's models) against the experimentally measured densities. Chan et al. [13] compared model-predicted packing densities (by de Larrard's, Yu's, and Kwan's models) against publicly available experimentally measured densities of binary mixtures (prepared from sand, polyethylene, and glass with sizes ranging from 74 μm to 20 mm). Du et al. [1] compared model-predicted packing densities (by de Larrard's model) against experimentally measured densities of mixtures from three component powders of alumina each having a nominal size of 2, 10, and 70 μm, respectively. However, no study has been reported about comparing different linear packing models against experimentally measured densities for such fine micropowders. Moreover, no study has been reported for any powder mixture about the deviation of predicted optimal mixing fraction from the mixing fraction for the measured peak density.

Table 4.1 Reported studies of linear packing models in the literature

Model	Material	Particle size	Application	Reference
de Larrard's [9] and Yu's [10]	Rock and cement	75 μm – 1.8 mm	Construction Engineering	Kwan et al., 2009 [5]
de Larrard's [9], Yu's [10], and Kwan's [11,12]	Sand, polyethylene, and glass	74 μm – 20 mm	Not specified	Chan et al., 2014 [13]
de Larrard's [9]	Alumina	2, 10, and 70 μm	Additive manufacturing	Du et al., 2021 [1]

This paper, for the first time, reports a study that compares the prediction performances of three packing models using experimental data from fine micropowders. In this paper, firstly, three

linear packing models (de Larrard's model [9], Yu's model [10], and Kwan's model [11,12]) were introduced. Packing densities for various powder mixing systems at different fractions of component powders, as well as optimal mixing fractions for the peak powder packing density, were calculated from these models. Various mixing fractions were selected to prepare binary and ternary powder mixtures, and the packing density for each powder mixture was measured. The prediction performances of these three models were assessed against experimental data.

4.2. Theoretical Framework

The three enhanced packing models assessed in this study are de Larrard's model [9], Yu's model [10], and Kwan's model [11,12]. These models are based on the assumption that all component powders and powder mixtures are under the state of dense packing and composed of non-deformable particles [8]. In the case of a powder mixture with *n* components (the components are ranked such that $d_i \geq d_{i+1}$, where d_i is the diameter of the *i*th component), the model-predicted packing density (γ) is given by [16]:

$$\gamma = \min(\gamma_1, \gamma_2, \cdots, \gamma_i, \cdots, \gamma_n) \quad (1)$$

where γ_i is the model-predicted packing density of the powder mixture assuming the *i*th component is "dominant" [8]. Here a dominant component means that its particles are tightly packed against each other, while the other smaller component particles fill voids of the dominant component particles, and the other larger component particles contact dominant particles only [5]. Moreover, all modeled powder packing densities in this paper are relative densities.

Adding a powder with a different size to an existing powder with a specific size can either increase or decrease its packing density. The added powder can increase the density by occupying the voids between finer particles, which is called the occupying effect [14], as illustrated in Figure 1(a), or by filling the voids between the coarser particles, which is called the filling effect, as

illustrated in Figure 1(b). These two effects are included in the original linear packing model by Equation 2 (and therefore in all three enhanced linear packing models).

The added powder can also decrease the powder packing density by three different effects. The first one is called wall effect of the coarse powder [12] when coarse particles disrupt the packing of fine particles at wall-like boundaries of coarse particles, as illustrated in Figure 1(a). The second is called loosening effect of fine powder [12] when fine particles are squeezed between the coarse particles, as illustrated in Figure 1(b). The third is called wedging effect [11] when coarse particles are close to each other and the space between them is not enough for a fine particle to occupy (if fine powder is dominant, as illustrated in Figure 1(a)), or when fine particles trapped between coarse particles preventing coarse particles from contacting each other (if coarse powder is dominant, as illustrated in Figure 1(b)). All these three effects can be included in the model by using interaction functions [13]. Different interaction functions can be fitted using the experimental data.

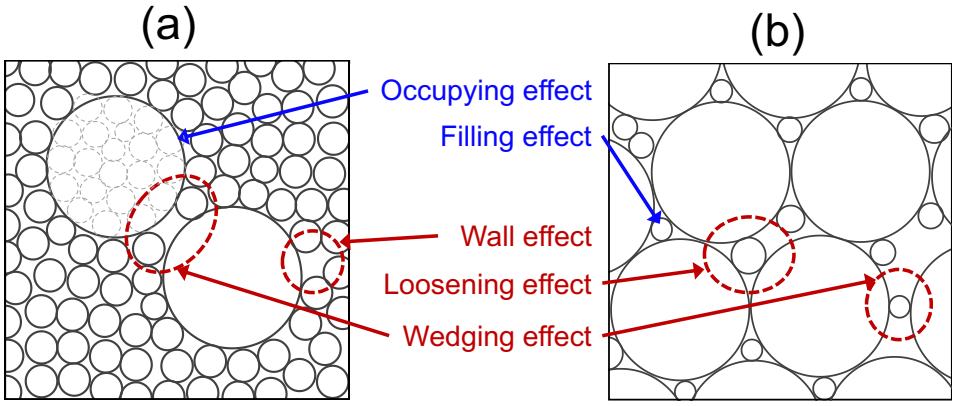

Figure 4.1 Illustrations of (a) occupying, wall, and wedging effects when fine powder is dominant (dashed circles in the coarse particle are imagined fine particles assuming the coarse particle is not present), and (b) filling, loosening, and wedging effects when coarse powder is dominant

In the following part of Section 2, three enhanced linear packing models are introduced. All models consider wall effect and loosening effect (by different interaction functions of these two effects). Kwan's model also considers wedging effect (by a third interaction function).

4.2.1. Two-parameter models (de Larrard's model and Yu's model) for both binary and ternary mixtures

A two-parameter model incorporates two effects, i.e. wall effect and loosening effect [9,10]. In a two-parameter model, the model-predicted packing density (γ_i) assuming the *i*th component is dominant is given by the following equation [5]:

$$\gamma_i = \frac{\beta_i}{1 - \sum_{j=1}^{i-1}\left[1 - \beta_i + b_{i,j}\beta_i\left(1 - \frac{1}{\beta_j}\right)\right]y_j - \sum_{j=j+1}^{n}\left[1 - a_{i,j}\frac{\beta_i}{\beta_j}\right]y_j} \tag{2}$$

where β_j and y_j are the packing density and volumetric fraction of the *j*th component, respectively. $a_{i,j}$ and $b_{i,j}$ are two interaction functions that reflect loosening and wall effects, respectively.

The interaction functions in **de Larrard's model** are [9]:

$$a_{i,j} = \sqrt{1 - \left(1 - \frac{d_j}{d_i}\right)^{1.02}} \tag{3}$$

$$b_{i,j} = 1 - \left(1 - \frac{d_j}{d_i}\right)^{1.5} \tag{4}$$

The interaction functions in **Yu's model** are [10]:

$$a_{i,j} = 1 - \left(1 - \frac{d_j}{d_i}\right)^{3.3} - 2.8 \cdot \frac{d_j}{d_i} \cdot \left(1 - \frac{d_j}{d_i}\right)^{2.7} \tag{5}$$

$$b_{i,j} = 1 - \left(1 - \frac{d_j}{d_i}\right)^{2} - 0.4 \cdot \frac{d_j}{d_i} \cdot \left(1 - \frac{d_j}{d_i}\right)^{3.7} \tag{6}$$

The final model-predicted packing density is determined by Equation (1).

4.2.2. Three-parameter model (Kwan's model)

A three-parameter model incorporates three effects, i.e. wall effect, loosening effect, and wedging effect [11].

4.2.2.1. Three-parameter model for binary mixture

The model-predicted packing density (γ_i) assuming *i*th component is dominant is given by the following equations [11]:

$$\frac{1}{\gamma_i} = \left(\frac{y_i}{\beta_i} + \frac{y_j}{\beta_j}\right) - \left(1 - b_{i,j}\right)\left(1 - \beta_j\right) \cdot \frac{y_j}{\beta_j} \cdot \left[1 - c_{i,j}(2.6^{y_j} - 1)\right] \tag{7}$$

$$\frac{1}{\gamma_j} = \left(\frac{y_i}{\beta_i} + \frac{y_j}{\beta_j}\right) - \left(1 - a_{i,j}\right) \cdot \frac{y_i}{\beta_i} \cdot \left[1 - c_{i,j}(3.8^{y_j} - 1)\right] \tag{8}$$

where the loosening effect, wall effect, and wedging effect interaction functions are [11]:

$$a_{i,j} = 1 - \left(1 - \frac{d_j}{d_i}\right)^{3.3} - 2.6 \cdot \frac{d_j}{d_i} \cdot \left(1 - \frac{d_j}{d_i}\right)^{3.6} \tag{9}$$

$$b_{i,j} = 1 - \left(1 - \frac{d_j}{d_i}\right)^{1.9} - 2 \cdot \frac{d_j}{d_i} \cdot \left(1 - \frac{d_j}{d_i}\right)^{6} \tag{10}$$

$$c_{i,j} = 0.322 \cdot tanh(11.9 \cdot s) \tag{11}$$

The final model-predicted packing density is determined by Equation (1).

4.2.2.2. Three-parameter model for ternary mixture

When the first component (the powder with the largest particle size) is dominant, the packing density of the ternary mixture is given by the following equation [12]:

$$\frac{1}{\gamma_1} = \frac{1}{\beta_T} - \left(1 - b_{1,2}\right)\left(1 - \beta_2\right) \cdot \frac{y_2}{\beta_2} \cdot \left[1 - c_{1,2}\left(2.6^{(y_2 + y_3)} - 1\right)\right] - \left(1 - b_{1,3}\right)\left(1 - \beta_3\right) \cdot \frac{y_3}{\beta_3} \cdot \left[1 - c_{1,3}\left(2.6^{(y_2 + y_3)} - 1\right)\right] \tag{12}$$

When the second component (the powder with the intermediate particle size) is dominant, the packing density of the ternary mixture is given by the following equation [12]:

$$\frac{1}{\gamma_2} = \frac{1}{\beta_T} - \left(1 - a_{1,2}\right) \cdot \frac{y_1}{\beta_1} \cdot \left[1 - c_{1,2}(3.8^{y_1} - 1)\right] - \left(1 - b_{2,3}\right)(1 - \beta_3) \cdot \frac{y_3}{\beta_3}$$

$$\cdot \left[1 - c_{2,3}(2.6^{y_3} - 1)\right] \quad (13)$$

When the third component (the powder with the smallest particle size) is dominant, the packing density of the ternary mixture is given by the following equation [12]:

$$\frac{1}{\gamma_3} = \frac{1}{\beta_T} - \left(1 - a_{1,3}\right) \cdot \frac{y_1}{\beta_1} \cdot \left[1 - c_{1,3}(3.8^{y_1} - 1)\right] - \left(1 - a_{2,3}\right) \cdot \frac{y_2}{\beta_2} \cdot \left[1 - c_{2,3}(3.8^{y_2} - 1)\right] \quad (14)$$

The interaction functions are the same as Equations (9)–(11), and the final model-predicted packing density is given by Equation (1).

4.3. Experimental Method

4.3.1. Characterization of particle morphology

Three alumina powders with nominal particle sizes of 2, 10, and 70 μm, respectively, were purchased from Inframat Corporation and used as component powders in this study. Particle morphologies of these component powders were characterized by scanning electron microscopy (SEM, TESCAN VEGA II LSU, Brno-Kohoutovice, Czech), and are shown in Figure 2. The shapes of powder particles are primarily spherical. The particle size within each powder is not perfectly uniform, but the size variation is much smaller than the size differences across the three powders.

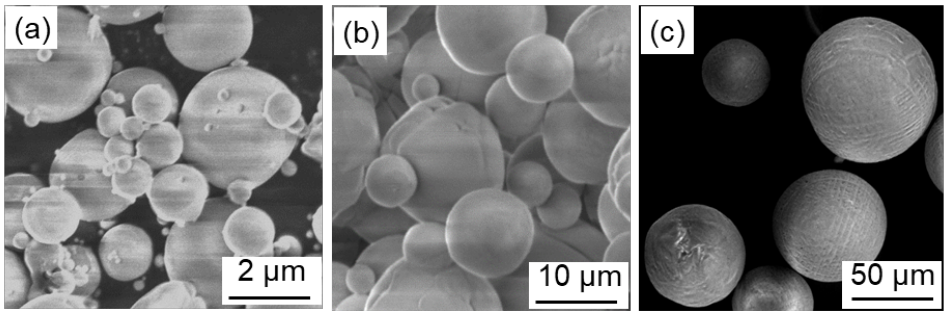

Figure 4.2 Particle morphologies of component powders: (a) 2 μm, (b) 10 μm, and (c) 70 μm

4.3.2. Preparation of powder mixtures

Three binary mixing systems and one ternary mixing system were prepared from the three component powders with sizes of 2, 10, and 70 μm. These mixing systems are denoted by 10/2, 70/2, 70/10, and 70/10/2 in this study. Various mixing fractions were selected to prepare different powder mixtures for each mixing system. All mixing fractions in this paper are based on the true (solid) volume of each powder. Since all component powders are composed of the same material (i.e., alumina), volumetric fractions are the same as mass fractions. A scale with an accuracy of 0.1 mg (AGCN200, Torbal, Oradell, NJ) was used to measure the fraction of each component powder. Measured component powders were mixed by ball milling (Jar Rolling Mills, Paul O. Abbe, Wood Dale, IL) for 1 h, using alumina balls with a diameter of 2 mm. The amount of balls was 10% of the powder mixture by mass. A low milling speed (~60 RPM) was used.

4.3.3. Measurement of tap density

The packing density of all component powders and powder mixtures is evaluated by tap density, a good estimation for the packing density of a densely packed powder [15,16]. The tap density of each powder was measured by a tap density meter (DY-100A, HongTuo, Dongguan, Guangdong, China) following an ASTM standard [17]. Specifically, the mass of each powder for tap density measurement was 100 g. Each measurement included 3000 tapping cycles with a 3-mm stroke. After tapping, the absolute tap density was calculated by dividing the mass by the volume of the powder inside the cylinder. The absolute tap density was then divided by the theoretical density of alumina (3.97 g/cm^3 [18]) to obtain the relative tap density. All experimentally measured packing densities in this paper are relative tap densities. The tap densities of component powders of 2, 10, and 70 μm are 61.0%, 61.0%, and 62.2%, respectively.

4.4. Results and Discussion

4.4.1. Experimental and modeling results

Experimentally measured densities and model-predicted densities from the three enhanced linear packing models for the three binary mixing systems are presented in Table 2 and Figure 3. As shown in Figure 3, the increase in the coarse powder fraction initially increased and then decreased the packing density of the powder mixtures. The increase in the fine powder fraction also initially increased and then decreased the packing density of the powder mixtures. The general trends of the relation between packing density and mixing fraction from the experiments and models match well.

Table 4.2 Experimentally measured and model-predicted packing densities for three binary mixing systems

Binary mixing system	Fraction of 2 μm powder (vol.%)	Fraction of 10 μm powder (vol.%)	Fraction of 70 μm powder (vol.%)	Experimentally measured density (%)	Predicted density by de Lard's model (%)	Predicted density by Yu's model (%)	Predicted density by Kwan's model (%)
10/2	53.7	46.3	/	68.7	65.1	70.0	69.4
10/2	43.7	56.3	/	70.0	66.1	72.3	71.6
10/2	33.7	66.3	/	71.0	69.0	74.8	73.9
10/2	28.7	71.3	/	71.4	71.0	72.4	75.1
10/2	23.7	76.3	/	71.6	71.4	70.1	74.9
10/2	18.3	81.3	/	69.4	70.0	68.0	71.5
10/2	13.7	86.3	/	67.1	65.7	65.9	68.3
70/2	50.0	/	50.0	74.5	73.7	75.0	74.9
70/2	40.0	/	60.0	77.6	75.8	78.6	78.5
70/2	30.0	/	70.0	80.8	78.2	82.6	82.5
70/2	25.0	/	75.0	81.1	78.5	78.4	82.4
70/2	20.0	/	80.0	76.6	74.7	74.5	77.4
70/2	15.0	/	85.0	72.5	71.9	71.0	72.9
70/2	10.0	/	90.0	68.8	66.1	67.8	69.0
70/10	/	52.3	47.7	70.5	68.6	71.7	71.3
70/10	/	42.3	57.7	72.1	72.6	74.5	73.9
70/10	/	32.3	67.7	73.5	76.3	77.4	76.8
70/10	/	27.3	77.7	74.0	76.4	74.6	78.3
70/10	/	22.3	77.7	74.2	74.0	72.0	77.0
70/10	/	17.3	82.7	71.4	70.9	69.5	73.1
70/10	/	12.3	87.7	68.7	69.0	67.2	69.6

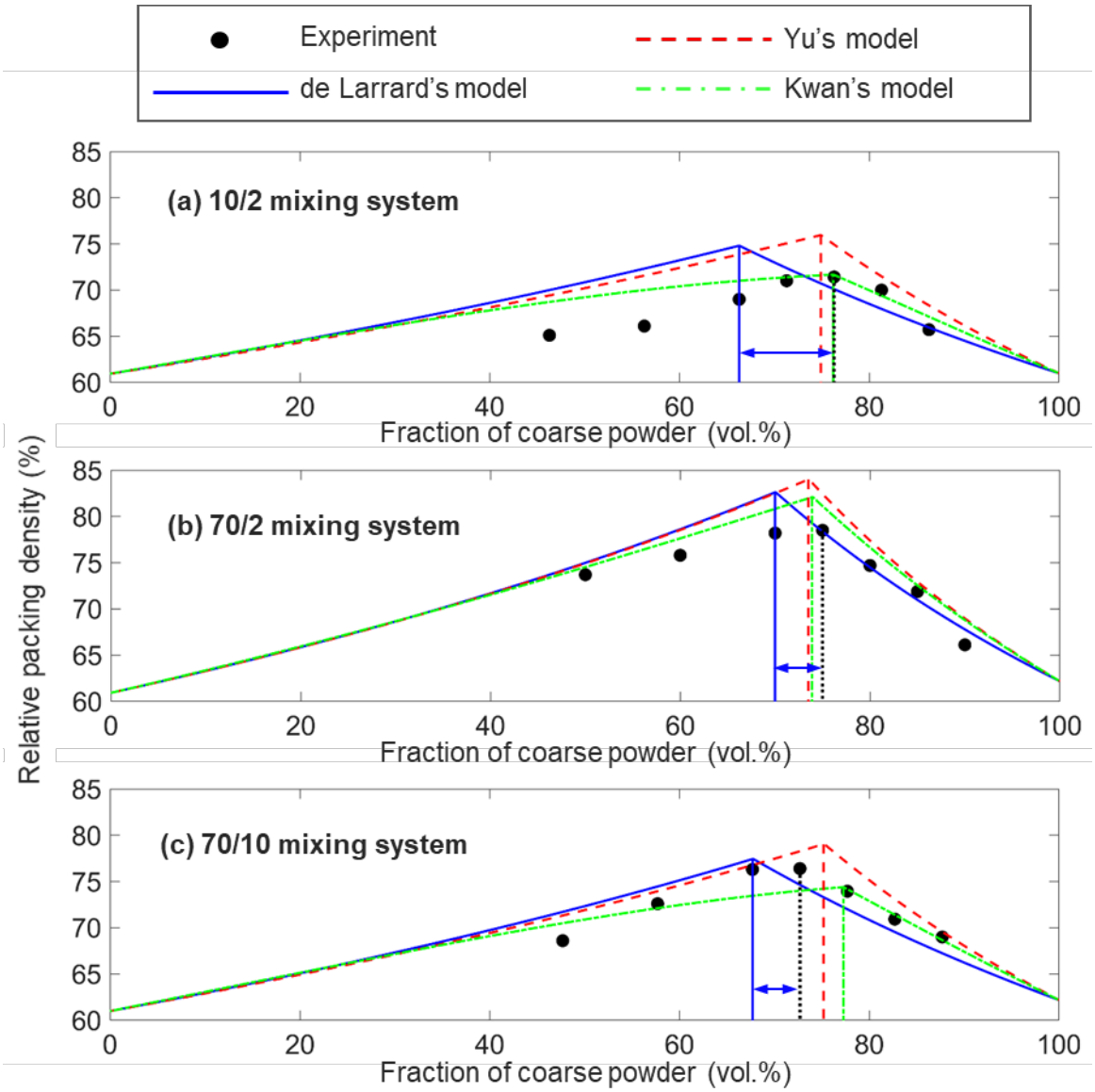

Figure 4.3 Experimentally measured and model-predicted packing densities for three binary mixing systems: (a) mixing system of 10 µm and 2 µm powders, (b) mixing system of 70 µm and 2 µm powders, and (c) mixing system of 70 µm and 10 µm powders (the double arrows show the derivations of optimal mixing fraction for de Larrard's model as examples)

Experimentally measured densities and model-predicted densities from the three enhanced packing models for the ternary mixing system are presented in Table 3 and Figure 4. The method to read the ternary plot can be found in the authors' previously published paper [1]. Based on both experimental and modeling results, the highest packing density can be achieved at relatively low fractions of 2 and 10 µm powders and a relatively high fraction of 70 µm powder. The general

trends of the relation between packing density and mixing fraction from the experiments and models match well.

Table 4.3 Experimentally measured and model-predicted packing densities for the ternary mixing system

Fraction of 2 μm powder (vol.%)	Fraction of 10 μm powder (vol.%)	Fraction of 70 μm powder (vol.%)	Experimentally measured density (%)	Predicted density by de Lard model (%)	Predicted density by Yu's model (%)	Predicted density by Kwan's model (%)
10	10	80	74.1	72.6	76.3	75.2
10	80	10	66.7	66.7	68.4	67.8
20	20	60	78.2	84.7	84.3	80.6
20	30	50	77.7	83.1	83.0	79.0
20	40	40	76.1	79.7	81.8	77.5
20	60	20	71.1	73.7	78.0	74.5
30	20	50	79.0	80.5	80.1	77.9
30	30	40	76.4	79.5	79.0	76.4
30	40	30	76.6	78.6	77.9	75.1
40	20	40	75.3	76.7	76.4	75.1
40	30	30	73.1	75.8	75.3	73.8
40	40	20	70.8	74.9	74.3	72.7
60	20	20	67.5	70.1	69.8	69.6
80	10	10	64.4	65.2	65.1	65.2

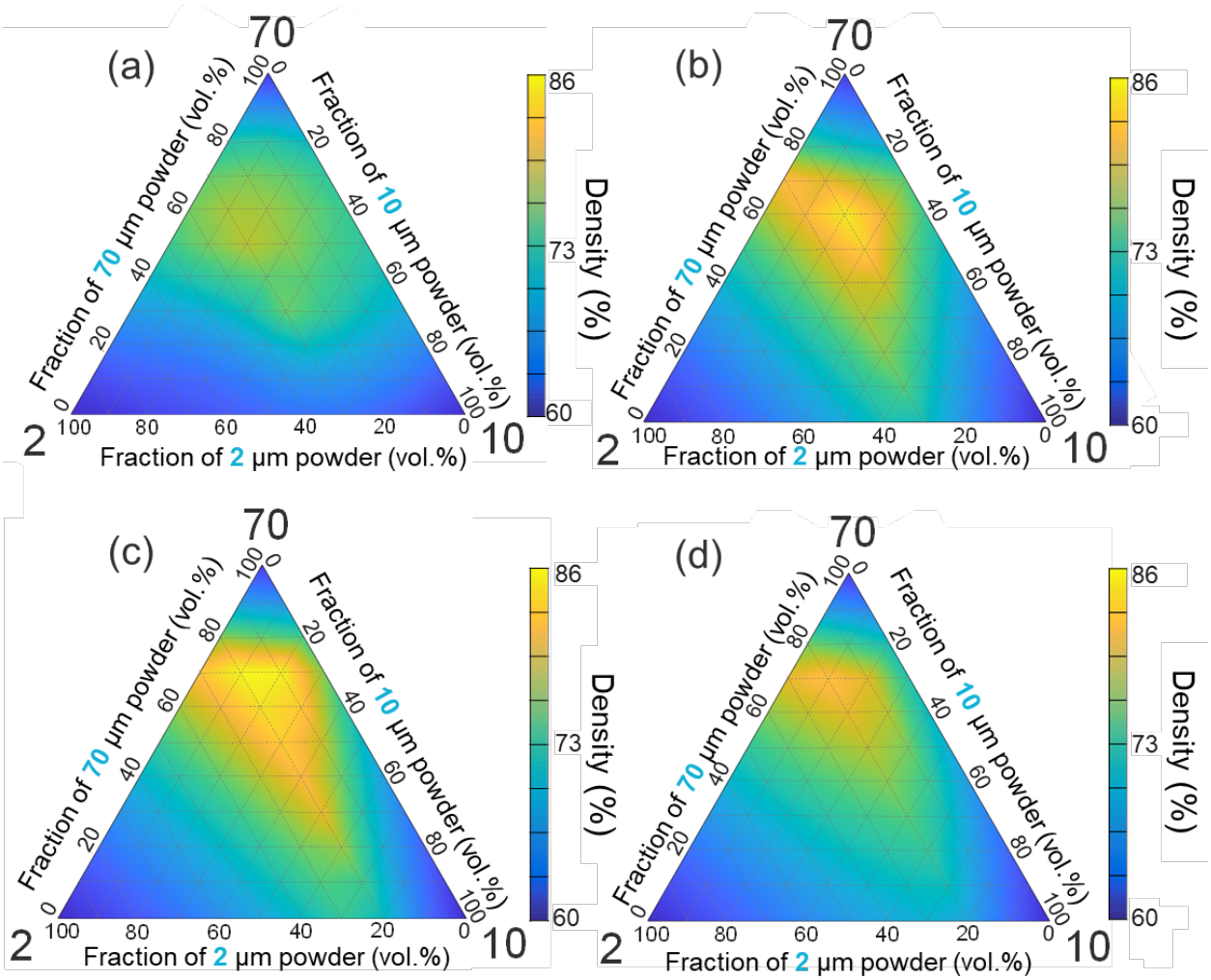

Figure 4.4 Packing densities for the ternary mixing system from (a) experiments, (b) de Larrard's model, (c) Yu's model, and (d) Kwan's model

4.4.2. Performances of three enhanced linear packing models

4.4.2.1. Deviation of predicted density from measured density at different mixing fractions

The deviation of predicted density from measured density (Dev_γ) at a specific mixing fraction was calculated based on the following equation:

$$Dev_\gamma = \frac{\gamma_p - \gamma_m}{\gamma_m} \tag{15}$$

where γ_p and γ_m are the model-predicted and experimentally measured packing densities, respectively.

Figures 5 and 6 show the deviations of predicted density for binary and ternary mixing systems, respectively. A positive deviation value indicates that the model-predicted density is higher than the experimentally measured one. de Larrard's model has both higher and lower predications than experimental values for all three binary mixing systems. Yu's model predictions are consistently higher than the experimental values. Kwan's model predictions are consistently higher than the experiment values for the 70/2 mixing system, but sometimes higher and sometimes lower than the experiment values for the other two mixing systems.

There are more positive deviation values than negative ones in both Figures 5 and 6, indicating that the model-predicted results are higher than the experimental ones. Predictions by Kwan's model (maximum deviation is 5.9%) have smaller positive deviations than those by de Larrard's and Yu's models (maximum deviations are 9.4% and 9.6%, respectively). Possible reasons include the consideration of the wedging effect in Kwan's model [11] that leads to lower density predictions (closer to the experimental results).

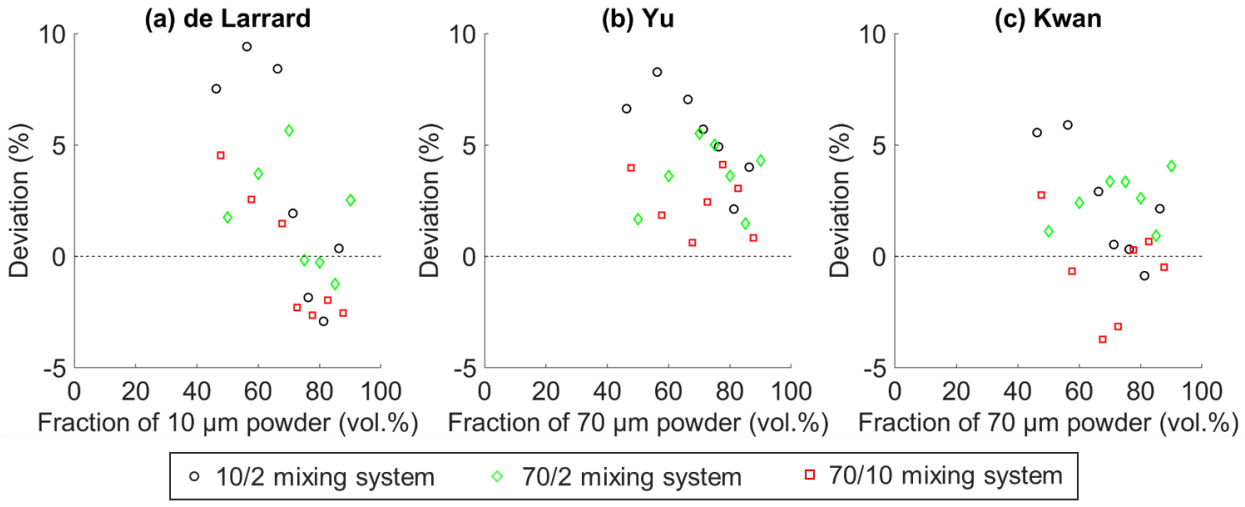

Figure 4.5 Deviations of predicted density for three binary mixing systems from three models: (a) de Larrard's, (b) Yu's, and (c) Kwan's

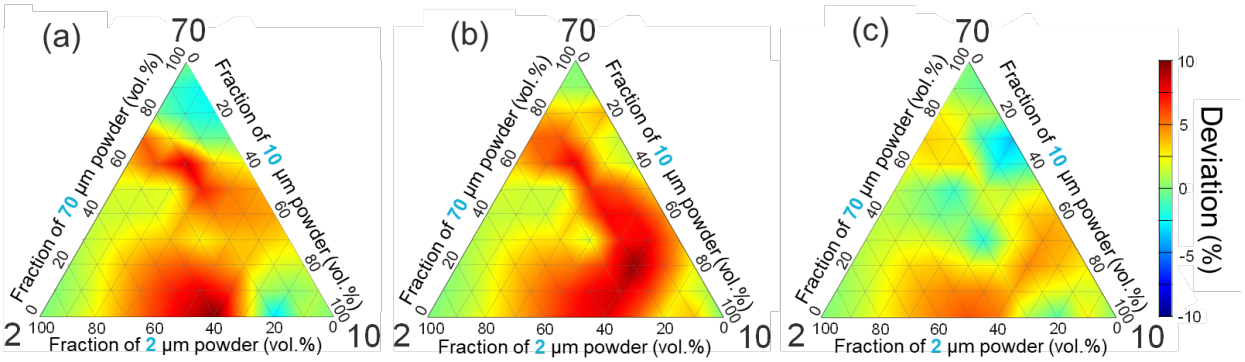

Figure 4.6 Deviations of predicted density for the ternary mixing system from three models: (a) de Larrard's, (b) Yu's, and (c) Kwan's

Mean absolute error (MAE) is a measure of the degree of deviation [19]. It was used in this study to evaluate the overall deviation of a model for a mixing system. For a specific model (i.e., de Larrard's, Yu's, or Kwan's), its MAE (e) for a mixing system (i.e., $e_{10/2}$, $e_{70/2}$, $e_{70/10}$, or $e_{70/10/2}$) is given by:

$$e = \frac{\sum_{i=1}^{n} |\gamma_{M_i} - \gamma_{E_i}|}{n} \tag{16}$$

where γ_{M_i} is the model-predicted density and γ_{E_i} is the experimentally measured density of the ith powder mixture. Here n is the number of powder mixtures in the corresponding mixing system that were experimentally studied (i.e., number of rows in Tables 2 and 3 for each mixing system).

To evaluate the overall performance of a model for all mixing systems, the average MAE (e_{avg}) of the model was calculated based on the MAE values of all four mixing systems, which was given by:

$$e_{avg} = \frac{e_{10/2} + e_{70/2} + e_{70/10} + e_{70/10/2}}{4} \tag{17}$$

The MAE values from Eq. (16) and Eq. (17) are shown in Table 4. Kwan's model has the smallest MAE values of 2.6%, 1.7% , and 1.8% for the mixing systems of 10/2, 70/10, and 70/10/2,

respectively. For the mixing system of 70/2, Yu's model has the smallest MAE value of 2.2%. Overall, Kwan's model has the smallest average MAE of 2.2% among all three models.

Table 4.4 Mean absolute error (MAE, e) values of three enhanced linear packing models

MAE	de Larrard (%)	Yu (%)	Kwan (%)
$e_{10/2}$	4.6	5.5	2.6
$e_{70/2}$	2.2	3.6	2.6
$e_{70/10}$	2.6	2.4	1.7
$e_{70/10/2}$	3.8	4.2	1.8
e_{avg}	3.3	3.9	2.2

4.4.2.2. Deviation of predicted optimal mixing fraction from the mixing fraction for the measured peak density

In this section, the deviation of predicted optimal mixing fraction for all three binary mixing systems is calculated. The deviation of predicted optimal mixing fraction was determined by the following equation:

$$Dev_y = y_M - y_E \tag{18}$$

where y_M and y_E are the model-predicted and experimentally determined values of optimal mixing fraction of the coarse powder corresponding to the peak density, respectively. In each subfigure of Figure 3, the black vertical line corresponds to the value of y_E, and the other three vertical lines correspond to three values of y_M for three models, respectively. In each subfigure, the blue vertical line (i.e., model-predicted optimal mixing fraction by de Larrard's model) is always the furthest from the black vertical line (i.e., experimentally determined optimal mixing fraction), meaning that de Larrard's model has the largest absolute deviation values. The double arrows show the deviations of optimal mixing fraction (i.e., Dev_y) for the de Larrard's model as examples.

Table 5 lists the model-predicted optimal mixing fractions from all three models and the corresponding experimental results for the three binary mixing systems. Figure 7 illustrates deviations of model-predicted optimal mixing fraction for all three binary mixing systems. Positive and negative deviation values mean larger and smaller model-predicted optimal mixing fraction than the mixing fraction for the measured peak density, respectively. For binary mixing systems of 10/2 and 70/2, all three models underpredicted the optimal mixing fractions of the coarse powder. For the binary mixing system of 70/10, de Larrard's model underpredicted the optimal mixing fractions of the coarse powder and the other two models overpredicted it.

For assessing performances of different models in terms of optimal mixing fraction, the absolute values of deviations calculated from Equation 18, i.e., $|Dev_y|$, is used. When absolute deviation values across different models were compared, Kwan's model outperformed the other two models for mixing systems of 10/2 and 70/2, and Yu's model outperformed the other two models for the mixing system of 70/10.

Table 4.5 Optimal mixing fractions of the coarse powder predicted from three models and experiments for three binary mixing systems

Binary mixing system	de Larrard's	Yu's model	Kwan's model	Experiment
10/2	66.3	74.9	76.2	76.3
70/2	67.7	75.2	77.3	72.7
70/10	70.0	73.5	73.9	75.0

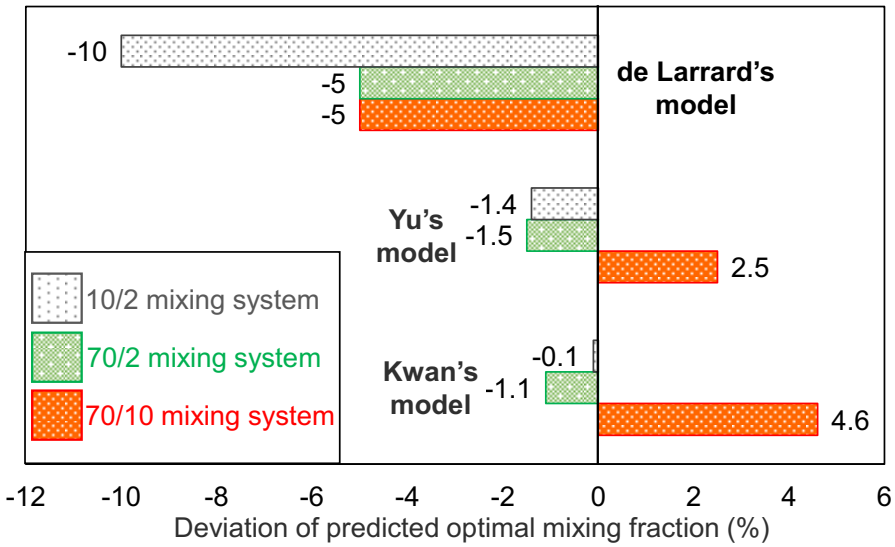

Figure 4.7 Deviations of model-predicted optimal mixing fraction of the coarse powder from the mixing fraction for the measured peak density of three binary mixing systems

4.5. Conclusions

This paper assessed the performances of three enhanced linear packing models in predicting packing densities and optimal mixing fractions of mixtures of micropowders with different sizes. The results on deviation of predicted powder packing density showed that Kwan's model achieved the best overall prediction performance (with a 2.2% average mean absolute error) among all three models. The results on deviation of predicted optimal mixing fraction showed that Kwan's model outperformed the other two models for the mixing system of 10 and 2 μm powders (with a -0.1% deviation value) and the mixing system of 70 and 2 μm powders (with a deviation value of -1.1%), and that Yu's model outperformed the other two models for the mixing system of 70 and10 μm powders (with a deviation value of 2.5%). This assessment study of prediction performances of three linear packing models provides a guidance for preparing micropowder mixtures.

4.6. References

[1] Du, W., Roa, J., Hong, J., Liu, Y., Pei, Z., and Ma, C., 2021, "Binder Jetting Additive Manufacturing: Effect of Particle Size Distribution on Density," Journal of Manufacturing

Science and Engineering, **143**(9), p. 091002 (9 pages).

[2] Bai, Y., Wagner, G., and Williams, C. B., 2017, "Effect of Particle Size Distribution on Powder Packing and Sintering in Binder Jetting Additive Manufacturing of Metals," Journal of Materials Science and Engineering, **139**(8), p. 081019 (6 pages).

[3] Du, W., Ren, X., Pei, Z., and Ma, C., 2020, "Ceramic Binder Jetting Additive Manufacturing: A Literature Review on Density," Journal of Manufacturing Science and Engineering, **142**(4), p. 040801 (19 pages).

[4] Kwan, A. K. H., Wong, V., and Fung, W. W. S., 2015, "A 3-Parameter Packing Density Model for Angular Rock Aggregate Particles," Powder Technology, **274**, pp. 154–162.

[5] Kwan, A. K. H., and Fung, W. W. S., 2009, "Packing Density Measurement and Modelling of Fine Aggregate and Mortar," Cement and Concrete Composites, **31**(6), pp. 349–357.

[6] Du, W., Ren, X., Chen, Y., Ma, C., Radovic, M., and Pei, Z., 2018, "Model Guided Mixing of Ceramic Powders with Graded Particle Sizes in Binder Jetting Additive Manufacturing," *ASME 2018 13th International Manufacturing Science and Engineering Conference*, College Station, TX, p. V001T01A014 (9 pages).

[7] Furnasz, C. C., 1931, "Grading Aggregates I-Mathematical Relations for Beds of Broken Solids of Maximum Density," Industrial & Engineering Chemistry, **23**(9), pp. 1052–1058.

[8] Stovall, T., de Larrard, F., and Buil, M., 1986, "Linear Packing Density Model of Grain Mixtures," Powder Technology, **48**(1), pp. 1–12.

[9] de Larrard, F., 1999, *Concrete Mixture Proportioning: A Scientific Approach*, E & FN Spon, London.

[10] Yu, A. B., Zou, R. P., and Standish, N., 1996, "Modifying the Linear Packing Model for

Predicting the Porosity of Nonspherical Particle Mixtures," Industrial & Engineering Chemistry Research, **35**(10), pp. 3730–3741.

[11] Kwan, A. K. H., Chan, K. W., and Wong, V., 2013, "A 3-Parameter Particle Packing Model Incorporating the Wedging Effect," Powder Technology, **237**, pp. 172–179.

[12] Wong, V., and Kwan, A. K. H., 2014, "A 3-Parameter Model for Packing Density Prediction of Ternary Mixes of Spherical Particles," Powder Technology, **268**, pp. 357–367.

[13] Chan, K. W., and Kwan, A. K. H., 2014, "Evaluation of Particle Packing Models by Comparing with Published Test Results," Particuology, **16**, pp. 108–115.

[14] Du, W., Singh, M., and Singh, D., 2020, "Binder Jetting Additive Manufacturing of Silicon Carbide Ceramics: Development of Bimodal Powder Feedstocks by Modeling and Experimental Methods," Ceramics International, **46**(12), pp. 19701–19707.

[15] Wong, H. H. C., and Kwan, A. K. H., 2008, "Packing Density of Cementitious Materials: Part 1—Measurement Using a Wet Packing Method," Materials and Structures, **41**(4), pp. 689–701.

[16] Yu, A. B., Bridgwater, J., and Burbidge, A., 1997, "On the Modelling of the Packing of Fine Particles," Powder Technology, **92**(3), pp. 185–194.

[17] Abdullah, E. C., and Geldart, D., 1999, "The Use of Bulk Density Measurements as Flowability Indicators," Powder Technology, **102**(2), pp. 151–165.

[18] ASTM International, 2015, "B527-15: Standard Test Method for Tap Density of Metal Powders and Compounds."

[19] Rahaman, M. N., 2003, *Ceramic Processing and Sintering*, CRC Press, New York.

[20] Willmott, C., and Matsuura, K., 2005, "Advantages of the Mean Absolute Error (MAE)

over the Root Mean Square Error (RMSE) in Assessing Average Model Performance," Climate Research, **30**(1), pp. 79–82.

5. COATING POWDER PARTICLES FOR INCREASING POWDER SINTERABILITY AND PART STRENGTH*

5.1. Introduction

Ceramic materials have outstanding properties, such as extraordinary hardness, excellent resistance to wear and heat, etc. Therefore, high added-value ceramic components can be applied in a wide range of fields such as aerospace, electronics, and health care. However, it is very costly to fabricate ceramic parts of a complex shape using conventional manufacturing techniques. For conventionally fabricated ceramic parts with a complex geometry, the tooling can contribute to up to 80% of the overall cost [1]. Conventional techniques have other disadvantages including excessive cost in prototypes and difficulty to make design changes [2]. All of these disadvantages have impeded the applications of advanced ceramic materials in the industry.

Binder jetting is an additive manufacturing process in which a liquid bonding agent is selectively deposited to join powder materials [3]. It has demonstrated its considerable potential in fabricating ceramic parts to avoid the substantial tooling cost, in addition to its advantage of minimal geometrical limitation. Currently, the relative density of ceramic parts resultant from binder jetting additive manufacturing is quite low, making the mechanical properties far from satisfactory [2,3]. The main reason comes from the low sinterability of current powder feedstock since a large particle size (10-100 μm) with a high flowability is required to deposit a smooth layer of powder for binder jetting.

---

*Reprinted with permission from "Ceramic Binder Jetting Additive Manufacturing: Particle Coating for Increasing Powder Sinterability and Part Strength" by Du, W., Ren, X., Ma, C., and Pei, Z., 2019. Materials Letters, 234, p. pp. 327–330, Copyright [2021] by Elsevier B.V.

The driving force of sintering is the reduction of the surface energy of a powder compact by the replacement of solid-air interface with solid-solid interface [4]. Increasing the surface area or the specific surface energy can enhance the driving force and consequently promote the sintering. Amorphous material has a higher specific surface energy and thus larger sintering driving force, leading to an enhanced necking. In this paper, a new powder surface modification method, i.e. particle coating is reported to assist with sintering, and consequently increase the strength of the printed and sintered parts. Specifically, coarse crystalline alumina particles were coated with amorphous alumina, forming a core-shell structure. The coarse crystalline core can help to maintain the high flowability and the amorphous shell can promote sintering due to its high activity [4].

5.2. Materials and Methods

Pechini-type sol-gel process was used to synthesize the amorphous phase material, which is schematically shown in Figure 5.1 [5]. A precursor solution was prepared by mixing aluminum nitrate nonahydrate ($Al(NO_3)_3 \cdot 9H_2O$, ≥98%, BeanTown Chemical, USA) and citric acid ($C_6H_8O_7$, VWR Life Science, USA) with a mole ratio of 1:2 in deionized water. Ethylene glycol ($(CH_2OH)_2$, VWR Life Science, USA) was then added in the solution with the same mole amount of citric acid. The solution was stirred until all the materials were dissolved. Spherical alumina powders of two different sizes (10 and 70 μm, Inframat Corporation, USA) were added into the mixture, respectively. The solution was then heat-treated to dehydrate the mixture into a gel. The gel was calcined in air at 700 °C for 3 h to burn out the sacrificial elements (C, H, and N) and obtain core-shell alumina particles. The obtained powders from the 10 and 70 μm seed powders were sieved through #500 and #170 screens, respectively. The coated powders were dry-pressed at 100 MPa into cylindrical disks of Φ12.7 mm in a stainless steel die. The green disks were then sintered at

1600 °C for 2 h and cooled in the furnace. Samples were prepared from the raw powders as well for comparison.

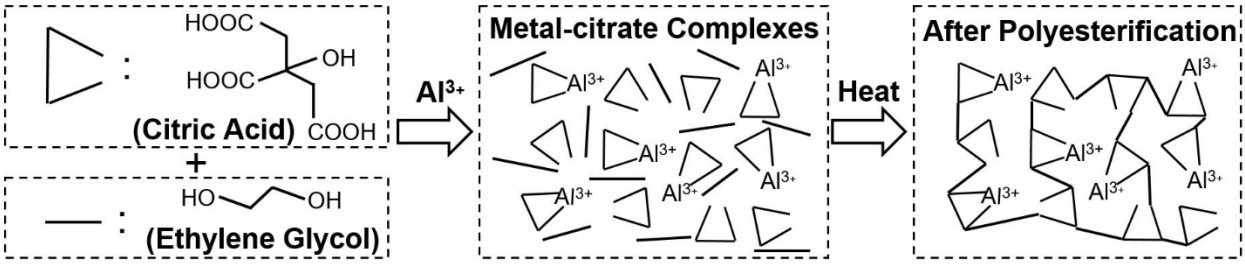

Figure 5.1 Basic principle of Pechini-type sol-gel process [5]

To verify the presence of the amorphous phase material, the calcined powder was tested by thermal gravimetric analysis (TGA) and differential scanning calorimetry (DSC) using combined TGA/DSC equipment (Q1000, TA Instruments, USA) with a heating rate of 10 °C/min and a temperature up to 1400 °C. Scanning electron microscopy (SEM, TESCAN VEGA II LSU, Brno-Kohoutovice, Czech Republic) was used to examine the morphology of the raw and coated powders and the microstructure of the fracture surfaces of the sintered samples. Compressive testing was carried out on a universal testing machine (STM-100KN-E, United Testing Systems Inc., USA).

5.3. Results and Discussion

The weight change and the heat flow for the coated powder from the TGA/DSC experiment is shown in Figure 5.2. The weight loss from 200 to 600 °C indicates the removal of sacrificial elements, while the spike of the heat flow at around 850 °C indicates the crystallization stage of the amorphous material. A small amount of weight loss continues to occur after crystallization, resulting from burning out remaining sacrificial elements. These TGA/DSC results confirmed the presence of the amorphous phase in the prepared powder.

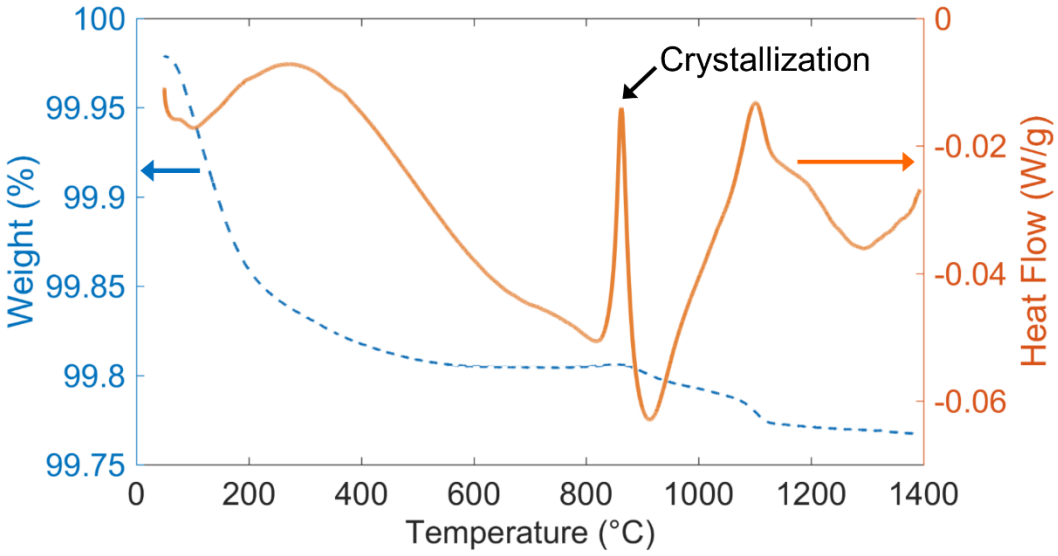

Figure 5.2 The changes of the weight and heat flow with temperature from the TGA/DSC of the coated powder

The morphologies of the raw and coated powders for the two different particle sizes (10 and 70 μm) are shown in the top row of Figure 5.3. After the powder surface modification, the coarse crystalline particle was coated with a large number of fine particles (the white dots on the surface). These fine particles are the amorphous alumina introduced by the sol-gel process. Moreover, the spherical shapes of two crystalline powders were retained after powder surface modification.

The fracture surfaces of the sintered parts are shown in the middle row of Figure 5.3. The parts from raw powders of both 10 and 70 μm have limited sintering densification due to their relatively low sinterability. No obvious necking was generated between particles and a large number of pores still exist in the part. For the parts from the coated powders, the amorphous material promoted the sintering by fusing the raw particles.

The necking between sintered particles for various powders is shown in the bottom row of Figure 5.3. Generally, a sintering process includes three stages (initial, intermediate, and final): necking formation, pore shrinkage, and pore closing, respectively [4]. For the raw particles of both 10 and 70 μm, the sinterability is low due to the large particle size. Only limited necking between

particles formed during the initial sintering stage and there were no further densification from the intermediate and final sintering stages [6], as Figures 5.3a and 5.3c show. For the 10 and 70 μm coated powders, however, enhanced necking was generated due to the introduction of the amorphous phase, as Figure 5.3b and 5.3d show.

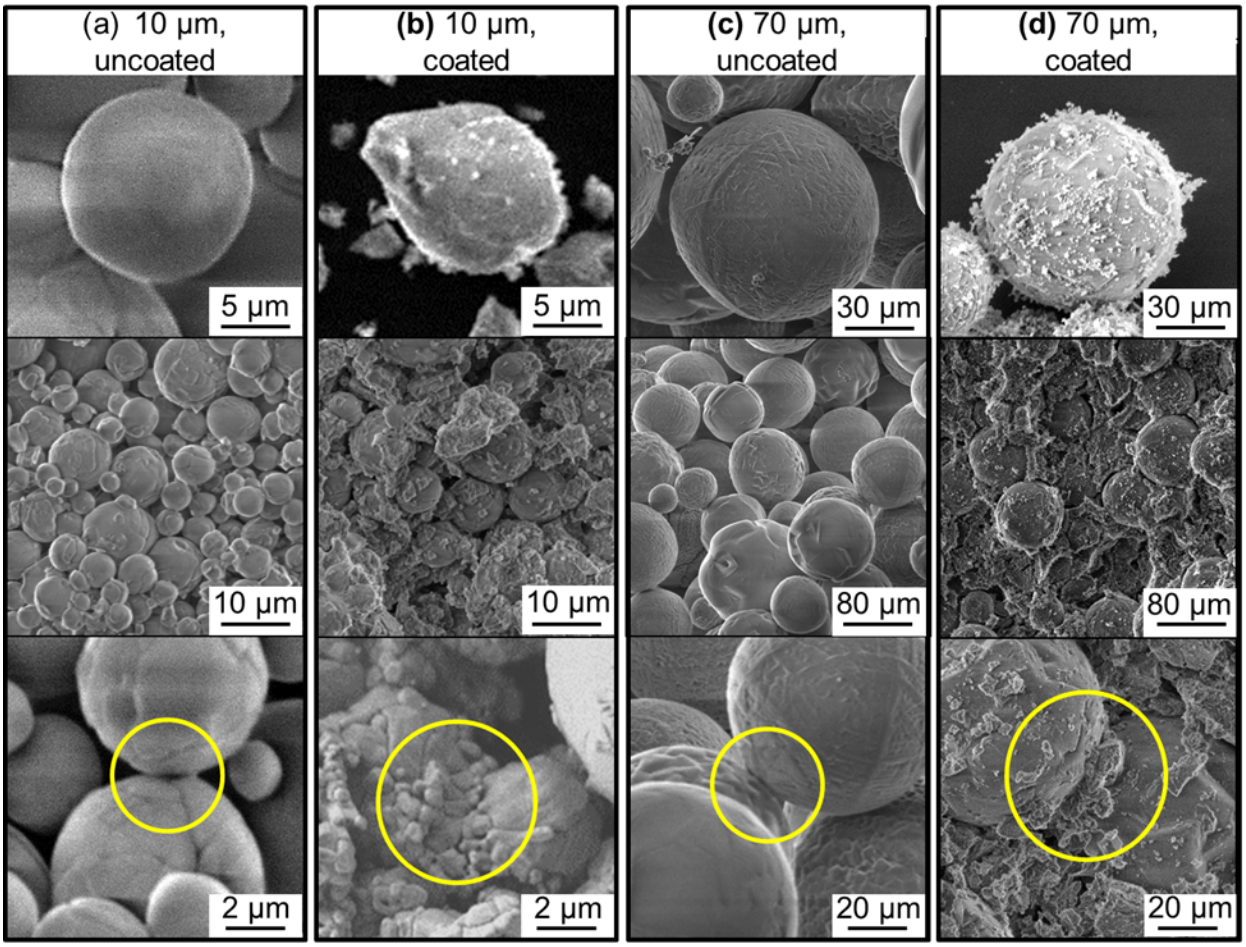

Figure 5.3 The morphologies of the particles (top row), the fracture surfaces of the fabricated parts (middle row), and the necking between sintered particles (bottom row) for (a) 10 μm raw, (b) 10 μm coated, (c) 70 μm raw, and (d) 70 μm coated powders.

Figure 5.4a shows the diameter shrinkages for different powders. After sintering, the diameter shrinkage of the samples from 10 and 70 μm raw powders are 1.3% and 0.6%, respectively, while those from 10 and 70 μm coated powders are 13.0% and 8.6%, respectively. The shrinkage for the

parts from both coated powders is significantly increased (by a factor of 10 for the 10 μm powder and 14 for the 70 μm one).

The compressive strength results are shown in Figure 5.4b. For the parts from 10 and 70 μm raw powders, the sintered compressive strengths were 18.7 and 0.7 MPa, respectively, while those for the 10 and 70 μm coated powders were 25.1 and 3.2 MPa, respectively. The sample from the 10 μm raw powder achieved larger strength than that from 70 μm, which was attributed to its smaller particle size and higher sinterability. Both coated powders led to significantly enhanced compressive strength compared with the raw powder counterparts, which was attributed to the better necking and the bond formed between particles with the help from the coated amorphous phase. The amorphous shells have higher specific surface energy and thus exhibit higher mobility during the sintering process. Therefore, they fuse with each other at the elevated temperature, forming a three-dimensional network that connects the crystalline cores, as shown in Figure 5.3. Eventually, the amorphous network turns into the thermally stable crystalline phase because of the high sintering temperature and becomes integrated with the crystalline cores. The bonding is strong between the three-dimensional network and the connected particles due to the fact that the amorphous shells and the crystalline cores are made of the same material (i.e., alumina). It is of great interest to confirm the proposed strengthen mechanism because it will help further improve the strength and extend this approach to other materials and processes.

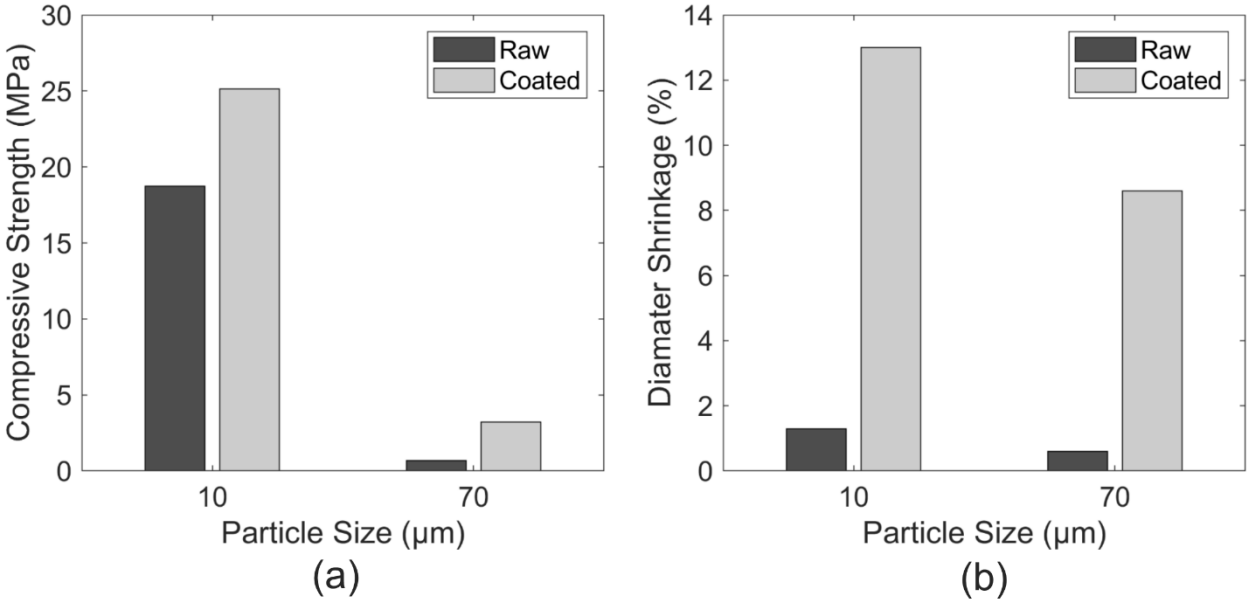

Figure 5.4 The diameter shrinkage (a) and the compressive strength (b) of the samples from raw and coated powders of different sizes

Although the sinterability and compressive strength were significantly improved, the mechanical properties do not meet the requirements of many load-bearing applications. The reason for the inferior mechanical properties is the low resultant relative density of the samples (48% for the 10 μm coated powder and 44% for the 70 μm coated powder), which may be due to the non-uniform coating. In addition, the particle coating method was demonstrated by a pressing and sintering route. The ultimate goal is to apply this method to binder jetting additive manufacturing, i.e., using a printing and sintering route. Therefore, future work includes investigating the strengthening mechanism, improving the quality of the powder, and applying the coated powder to binder jetting additive manufacturing process.

5.4. Conclusions

Crystalline alumina particles (10 and 70 μm) were successfully coated with an amorphous alumina phase using a sol-gel process. The sintered samples from the coated powders demonstrated enhanced necking, increased diameter shrinkage, and improved compressive

strength, compared with those from the raw powders. In summary, the particle coating method is effective in increasing the powder sinterability and part compressive strength and is promising in ceramic binder jetting additive manufacturing.

5.5. References

[1] Klocke, F., 1997, "Modern Approaches for the Production of Ceramic Components," J. Eur. Ceram. Soc., **17**(2–3), pp. 457–465.

[2] Du, W., Ren, X., Ma, C., and Pei, Z., 2017, "Binder Jetting Additive Manufacturing of Ceramics: A Literature Review," *ASME 2017 International Mechanical Engineering Congress and Exposition*, Tampa, FL, pp. 1–12.

[3] Du, W., Ren, X., Chen, Y., Ma, C., Radovic, M., and Pei, Z., 2018, "Model Guided Mixing of Ceramic Powders with Graded Particle Sizes in Binder Jetting Additive Manufacturing," *ASME 2018 13th International Manufacturing Science and Engineering Conference*, College Station, TX, pp. 1–9.

[4] Ring, T. A., 1996, *Fundamentals of Ceramic Powder Processing and Synthesis*, Academic Press, London.

[5] Lin, J., Yu, M., Lin, C., and Liu, X., 2007, "Multiform Oxide Optical Materials via the Versatile Pechini-Type Sol-Gel Process: Synthesis and Characteristics," J. Phys. Chem. C, **111**(16), pp. 5835–5845.

[6] Kang, S.-J. L., 2005, *Sintering : Densification, Grain Growth, and Microstructure*, Elsevier Butterworth-Heinemann, Burlington.

6. GRANULATING NANOPARTICLES TO MICRON-SIZED GRANULES: EFFECTS OF PREPARATION PARAMETERS IN SPRAY FREEZE DRYING ON POWDER PROPERTIES*

6.1. Introduction

Ceramic materials have outstanding properties, such as extraordinary hardness, excellent resistance to wear, heat, and corrosion, and exceptional biocompatibility [1]. However, it is very costly to fabricate ceramic parts of complex shapes using conventional manufacturing techniques. For complex ceramic parts, tooling can contribute to up to 80 % of the overall cost if traditional processing routes are taken [2]. Compared with that, additive manufacturing (AM), also known as 3D printing, has many advantages, including flexible and customized design, elimination of special fabrication tooling, and efficient usage of raw materials. Therefore, AM of ceramic materials has attracted a lot of research interest [3]. Among all AM technologies, binder jetting is considered the most promising for printing ceramic materials because it is easy to scale up and it does not require support [4].

A high density of a ceramic part is usually desirable for the load-bearing applications, such as artificial human joints [5]. However, the achieved density of the printed parts from binder jetting is relatively low even after sintering [1]. Currently, the bulk density [6] of ceramic parts by this process ranges from 40% to 68% [7–12], far below the requirement for load-bearing applications. The main cause comes from the contradicting requirements for the particle size of the feedstock powder: a large particle size (>5 μm) is required for a high flowability while a small particle size

*Reprinted with permission from "Binder Jetting Additive Manufacturing of Ceramics: Feedstock Powder Preparation by Spray Freeze Granulation" by Du, W., Miao, G., Liu, L., Pei, Z., and Ma, C., 2019. ASME 2019 14th International Manufacturing Science and Engineering Conference, Errie, PA, V001T01A006 (6 pages), Copyright [2021] by ASME.

(<1 μm) for a high sinterability. Granulation has been attempted to address this contradiction [1]. By granulating fine particles into coarse granules, the granulated powder will maintain the high sinterability of the fine particles and increase the flowability by the increased size. Among many different granulation methods reported in the literature, spraying drying (SD) is the most common one [13–19]. However, some of its disadvantages impeded its application. For example, spray-dried granules usually show a hollow structure due to the rapid mass transport of the binder liquid from the center to the shell of the granule during the evaporation drying, which leads to inhomogeneous microstructures of the part [20]. The hard shell of SD granules will make them difficult to break and thus result in inter-granule porosity [20,21].

Another granulation method, called spray freeze drying (SFD), has attracted interest for the ceramic material preparation [20–25]. As this technology uses a drying route of freezing-sublimation, the mass transport is slow and controlled during the drying step, which makes the microstructure of the granules homogeneous. For example, Raghupathy *et al*. [20] prepared granulated zirconia powder by both spraying drying and spray freeze drying. Although both powders achieved similar flow rates, crushable granules with a low granule strength were obtained only from spray freeze drying, which is beneficial to the microstructure homogeneity of dry-pressed and sintered parts. Ghanizadeh *et al*. [23] prepared granulated alumina powder and characterized its flow rate. Green and sintered densities (densities of the part after curing and sintering, respectively) were measured for dry-pressed disk samples to investigate the effect of the sintering profile on the grain growth.

Despite some existing studies on spray freeze drying of ceramic materials, the effects of the spraying pressure and slurry feed rate on the flowability and sinterability of the granulated powder have not been studied. This study aims at filling this knowledge gap by carrying out experiments

based on a full factorial design. The granule size and morphology were characterized, and the flow rate of the obtained powder and the density of dry-pressed and sintered disk samples were studied. Finally, discussion was created based on the results.

6.2. Experimental Methods

6.2.1. Slurry preparation

Nano-sized alumina slurry (100 nm, 20 wt. %, Department of Specialty Grains & Powders, Saint-Gobain Ceramic Materials, MA, USA) was used to ensure a high sinterability of the feedstock material. The slurry was frozen in a freezer and then dried in a freeze drier (FreeZone 2.5 L, Labconco, MO, USA) under 1.5 mbar for 12 h to obtain the dry powder. The dried alumina was mixed with deionized water using a ball mill (Laboratory Jar Rolling Mill, Paul O. Abbe, IL, USA) to prepare 20 vol. % slurry for spraying. The ball milling parameters are shown in Table 6.1.

6.2.2. Granulated powder preparation

Nano-sized alumina slurry (100 nm, 20 wt. %, Department of Specialty Grains & Powders, Saint-Gobain Ceramic Materials, MA, USA) was used to ensure a high sinterability of the feedstock material. The slurry was frozen in a freezer and then dried in a freeze drier (FreeZone 2.5 L, Labconco, MO, USA) under 1.5 mbar for 12 h to obtain the dry powder. The dried alumina was mixed with deionized water using a ball mill (Laboratory Jar Rolling Mill, Paul O. Abbe, IL, USA) to prepare 20 vol. % slurry for spraying. The ball milling parameters are shown in Table 6.1.

Spray freeze drying includes spray freezing and freeze drying. Figure 6.1 shows the machine set up (LS-2, PowderPro AB, Sweden) for the spray freezing. A peristaltic pump feeds the slurry into an atomizing nozzle that is above the liquid surface and connected with compressed air. The slurry is atomized into droplets, which are sprayed into liquid nitrogen in the spraying container.

The frozen granules are then put on a tray in the drying chamber of the freeze drier to sublimate the water in the granules.

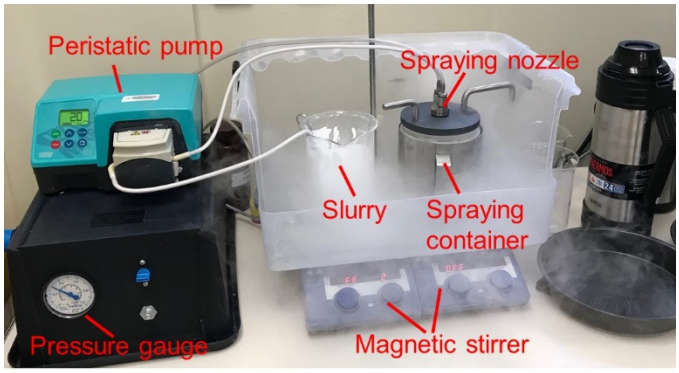

Figure 6.1 PowderPro LS-2 freeze granulator

To investigate the effects of the granulation parameters (spraying pressure and feed rate), two levels of each parameter were tested to form a full factorial design, as shown in Table 6.1. Therefore, there were four trials with different combinations of the spraying pressure and feed rate. The freeze drying parameters, as listed in Table 6.1, were kept fixed across all trials.

Table 6.1 The parameters for the slurry preparation, spray freezing, and freeze drying

Slurry preparation	Alumina concentration (vol. %)	20
	Ball-to-slurry mass ratio	1:1
	Milling time (h)	12
Spray freezing	Pressure (bar)	0.1 and 0.4
	Feed rate (L/h)	0.5 and 1
Freeze drying	Drying chamber pressure (mbar)	1.5
	Tray temperature (°C)	20
	Collector temperature (°C)	-50
	Drying time (h)	12

6.2.3. Material characterization

To prepare the sample for the morphology of the raw particles, the diluted slurry was dripped onto the surface of a silicon wafer and was left at room temperature to be slowly dried. The

morphology of the raw particles was characterized by scanning electron microscopy (SEM, JSM-7500F, JEOL, Japan). After granulation, the morphology of the obtained granules was characterized by another SEM (TESCAN VEGA II LSU, Brno-Kohoutovice, Czech Republic). The granule size was studied by sieve analysis. An eight-inch sieve set with opening sizes of 25, 53, 75, 90, and 250 μm was used.

As a feedstock powder with a particle size smaller than 25 μm or larger than 250 μm is rarely used in binder jetting, granulated powders within size ranges of 25–53, 53–75, 75–90, and 90–250 μm from all four trials were used for the measurement of flowability and sinterability. Flowabilities of the raw and granulated (25–250 μm) powders were tested by measuring the flow rate, i.e., the weight of falling granules through a funnel with an opening of Φ2.54 mm (DF-1-02, Hongtuo Instrument, China) in one second.

For the sinterability test, these powders were dry-pressed at 100 MPa into disks of Φ12.7 mm by a hydraulic cold press (Carver Laboratory Press, Model C, Fred S. Carver Inc., IN, USA). The pressed disks were then sintered at 1600 °C for 2 h and cooled to room temperature in a bench-top muffle furnace (KSL-1700X-A1-UL, MTI Corp., CA, USA). A disk sample from the raw powder was prepared as well for comparison. Sinterabilities of the raw and granulated powders were tested by measuring the relative sintered density of the disk samples using a density kit (Torbal AGCN200, Scientific Industries Inc., NJ, USA). The sintered density was measured based on the ISO standard [6]. Specifically, dry mass (m_1) was measured after sintering and cooling. Then the sample was boiled in deionized water for 2 h and then cooled to the room temperature. The mass of the sample in water (m_2) was measured by the density kit and then the sample was wiped by a wet cloth to remove the water on the surface, followed by the measurement of the mass of the

wiped sample (m_3). The relative sintered bulk density (ρ) of the sample was calculated based on the following equation:

$$\rho = \frac{\rho_{wt}}{\rho_{th}} \times \frac{m_1}{m_3 - m_2} \times 100\% \quad (1)$$

where ρ_{wt} is the water density at the temperature when taking the measurement and ρ_{th} is the theoretical density of the alpha-phase alumina (3.97 g/cm^3).

6.3. Results and Discussion

Figure 6.2 shows the SEM of the raw powder in the spraying slurry. The particle has an irregular shape and its size is around 100 nm.

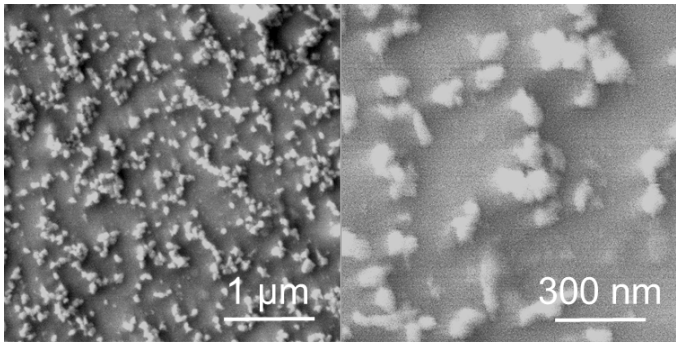

Figure 6.2 SEM of the raw 100 nm powder

The SEM of the granulated powders from different trials is shown in Figure 6.3. The shape of the granules is spherical. Granules from Trials 2–4 evidently present a satellite structure, i.e., small granules firmly attach to a larger one. Based on a comparison between Trial 1 and Trial 3, higher spraying pressure leads to a greater extent of satellite structures. Similarly, a comparison between Trial 2 and Trial 4 leads to the same result. Based on a comparison between Trial 3 and Trial 4, higher feed rate leads to a greater extent of satellite structures. Similarly, a comparison between Trial 1 and Trial 2 leads to the same result. In summary, the spraying pressure and feed rate significantly affect the extent of satellite structure. Higher spraying pressure and higher feed rate lead to a greater extent of satellite structure, resulting in the greatest extent of satellite structure

for the powder from Trial 4. One of the reasons is that higher spraying pressure creates more fine droplets, and higher feed rate increases the amount of the sprayed droplets in a unit time, both of which lead more collisions between the sprayed droplets in the spraying container and consequently a great extent of satellite structure in the granulated powder.

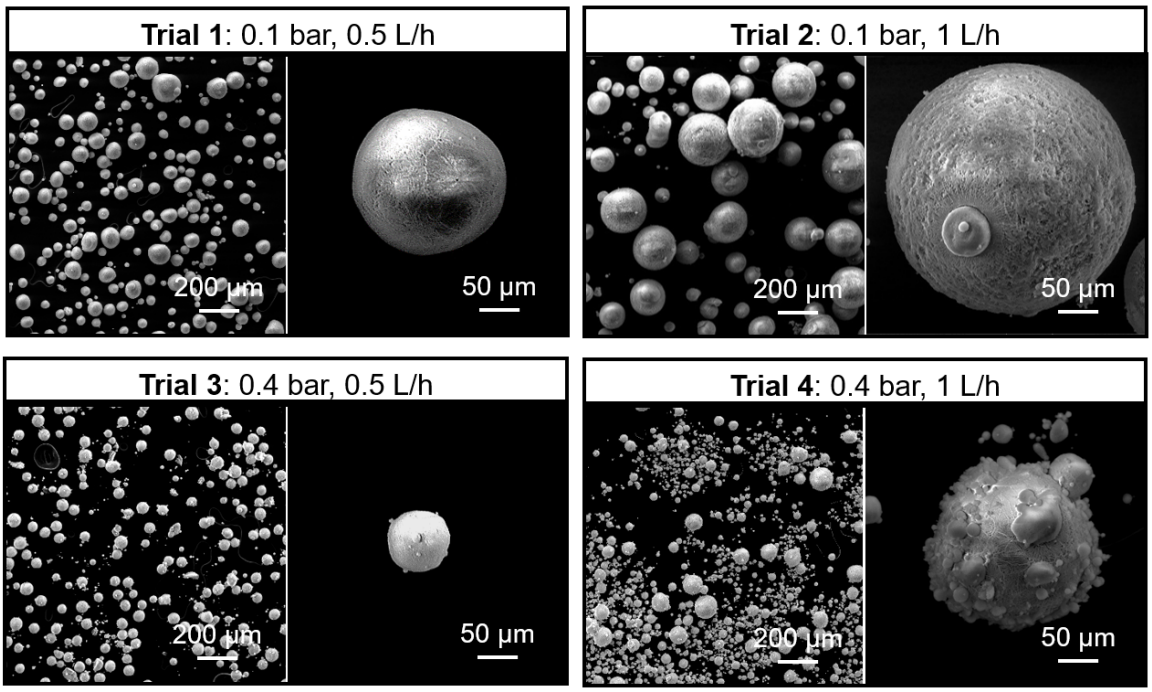

Figure 6.3 SEM of granules from all four trials

Figure 6.4 shows the results of the sieve analysis of all four trials. The dominant size ranges are 90–250, >250, 25–53, and 90–250 µm for Trials 1–4, respectively. The sieve analysis result agrees well with the SEM characterization. Based on the sieve analysis result in Figure 6.4, it can be concluded that higher spraying pressure leads to smaller granule size at the same feed rate. At the same feed rate of 0.5 L/h, for example, the increase of the spraying pressure (Trial 1 to Trial 3) led to a decrease of the dominant size range from 90–250 µm to 25–53 µm. On the other hand, higher feed rate leads to larger granule size at the same spraying pressure. At the same spraying pressure of 0.4 bar, for example, the increase of the feed rate (Trial 3 to Trial 4) led to an increase of the dominant granule size range from 25–53 to 90–250 µm. In summary, the spraying pressure

and feed rate significantly affect the granule size. Higher spraying pressure and lower feed rate lead to smaller granule size, resulting in the smallest dominant size range of 25–53 μm for the granulated powder from Trial 3.

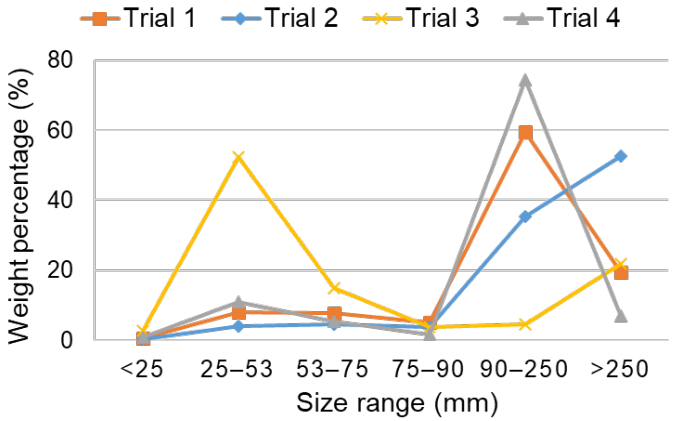

Figure 6.4 Weight percentages of different size ranges of the granulated powder from different experiments

Table 6.2 shows the flow rates of the raw and granulated powders and the sintered densities of the disk samples from these powders. In some cases, the powder has a too low flowability to fall through the funnel opening and no value was obtained for the flow rate test. To explain the flow rate results, it is needed to examine the forces that are applied to the granules. Among all the forces, gravity is dominant for large granules while interparticle forces, such as van der Waals and electrostatic forces, are dominant for small granules. Therefore, large granules tend to flow easily while small ones not due to interparticle friction and agglomeration [26]. As shown in Table 6.2, it can be concluded that granule size significantly affects its flowability. For the granulated powder within the same trial, the flowability increases (or stay the same) as the size increases. Another factor that affects the flowability of the granulated powder is the extent of the satellite structure, which will decrease the flowability due to the increased inter-granule friction. As shown in Figure 6.3, the granulated powder from Trial 1 has the least extent of satellite structure. Within the same size range, the flow rate of the granulated powder from Trial 1 is larger than (or equal to) that of

granulated powders from all other trials. On the other hand, granulated powder from Trial 4 has the greatest extent of satellite structure. Within the same size range, the flow rate of the granulated powder from Trial 4 is less than (or equal to) that of granulated powders from all other trials.

Table 6.2 Flowability and sinterability test results of raw and granulated powders

Trial	Size (μm)	Flow rate (g/s)	Relative sintered density (%)
Raw	0.1	/	93.4
1	25–53	0.06	96.7
	53–75	0.19	95.0
	75–90	0.24	98.0
	90–250	0.24	96.2
2	25–53	/	97.0
	53–75	0.19	94.6
	75–90	0.20	96.1
	90–250	0.24	91.6
3	25–53	/	93.5
	53–75	0.09	97.2
	75–90	0.10	94.6
	90–250	0.21	96.2
4	25–53	/	96.2
	53–75	0.08	95.7
	75–90	0.10	94.9
	90–250	0.10	96.9

Sinterability is another important factor of the feedstock material for the binder jetting process. Under the same conditions, a material with high sinterability leads to high sintered density of the printed part [1], and a sintered density of larger than 90% usually indicates a good sinterability. After granulation, the high sinterability of the raw alumina powder was maintained (or even increased in most cases) in the spray-freeze-dried granulated powders. Reasons for the increase of the sintered density include the flowability improvement after granulation and subsequently more dense packing of the granules of the disk sample after pressing.

6.4. Conclusions

Experimental trials based on a full factorial design of spraying pressure and slurry feed rate were carried out to study their effects on the granule size, flowability, and sinterability of the granulated powder. Size analysis results show that high spraying pressure and low feed rate lead to small granule size. Morphology analysis revealed the satellite structure in the granulated powder, whose extent increased as the spraying pressure and feed rate increased. Larger granule size and less extent of satellite structure led to a higher flow rate and better flowability. Moreover, sintered densities of the disk samples from most of the granulated powders are higher than that of the raw powder. This study could guide the feedstock powder preparation process for ceramic binder jetting additive manufacturing by spraying freeze drying.

6.5. References

[1] Du, W., Ren, X., Ma, C., and Pei, Z., 2017, "Binder Jetting Additive Manufacturing of Ceramics: A Literature Review," *ASME 2017 International Mechanical Engineering Congress and Exposition*, Tampa, FL, pp. 1–12.

[2] Klocke, F., 1997, "Modern Approaches for the Production of Ceramic Components," J. Eur. Ceram. Soc., **17**(2–3), pp. 457–465.

[3] Deckers, J., Vleugels, J., and Kruth, J. P., 2014, "Additive Manufacturing of Ceramics: A Review," J. Ceram. Sci. Technol., **5**(4), pp. 245–260.

[4] Du, W., Ren, X., Ma, C., and Pei, Z., 2019, "Ceramic Binder Jetting Additive Manufacturing: Particle Coating for Increasing Powder Sinterability and Part Strength," Mater. Lett., **234**, pp. 327–330.

[5] Du, W., Ren, X., Chen, Y., Ma, C., Radovic, M., and Pei, Z., 2018, "Model Guided Mixing of Ceramic Powders with Graded Particle Sizes in Binder Jetting Additive Manufacturing," *ASME 2018 13th International Manufacturing Science and Engineering*

Conference, College Station, TX, pp. 1–9.

[6] ISO, 2013, "ISO 18754:2013 Fine Ceramics (Advanced Ceramics, Advanced Technical Ceramics) – Determination of Density and Apparent Porosity."

[7] Mehrban, N., Bowen, J., Vorndran, E., Gbureck, U., and Grover, L. M., 2013, "Structural Changes to Resorbable Calcium Phosphate Bioceramic Aged in Vitro," Colloids Surfaces B Biointerfaces, **111**, pp. 469–478.

[8] Sheydaeian, E., Vlasea, M., Woo, A., Pilliar, R., Hu, E., and Toyserkani, E., 2017, "Effect of Glycerol Concentrations on the Mechanical Properties of Additive Manufactured Porous Calcium Polyphosphate Structures for Bone Substitute Applications," J. Biomed. Mater. Res. - Part B Appl. Biomater., **105**(4), pp. 828–835.

[9] Dcosta, D. J., Sun, W., Lin, F., and Ei-Raghy, T., 2002, "Freeform Fabrication of Ti3SiC2 Powder-Based Structures: Part II - Characterization and Microstructure Evaluation," J. Mater. Process. Technol., **127**(3), pp. 352–360.

[10] Shanjani, Y., Amritha De Croos, J. N., Pilliar, R. M., Kandel, R. A., and Toyserkani, E., 2010, "Solid Freeform Fabrication and Characterization of Porous Calcium Polyphosphate Structures for Tissue Engineering Purposes," J. Biomed. Mater. Res. - Part B Appl. Biomater., **93**(2), pp. 510–519.

[11] Tarafder, S., Balla, V. K., Davies, N. M., Bandyopadhyay, A., and Bose, S., 2013, "Microwave-Sintered 3D Printed Tricalcium Phosphate Scaffolds for Bone Tissue Engineering," J. Tissue Eng. Regen. Med., **7**(8), pp. 631–641.

[12] Suwanprateeb, J., Sanngam, R., and Suwanpreuk, W., 2008, "Fabrication of Bioactive Hydroxyapatite/Bis-GMA Based Composite via Three Dimensional Printing," J. Mater. Sci. Mater. Med., **19**(7), pp. 2637–2645.

[13] Warnke, P. H., Seitz, H., Warnke, F., Becker, S. T., Sivananthan, S., Sherry, E., Liu, Q., Wiltfang, J., and Douglas, T., 2010, "Ceramic Scaffolds Produced by Computer-Assisted 3D Printing and Sintering: Characterization and Biocompatibility Investigations," J. Biomed. Mater. Res. - Part B Appl. Biomater., **93**(1), pp. 212–217.

[14] Becker, S. T., Bolte, H., Krapf, O., Seitz, H., Douglas, T., Sivananthan, S., Wiltfang, J., Sherry, E., and Warnke, P. H., 2009, "Endocultivation: 3D Printed Customized Porous Scaffolds for Heterotopic Bone Induction," Oral Oncol., **45**(11), pp. e181–e188.

[15] Castilho, M., Moseke, C., Ewald, A., Gbureck, U., Groll, J., Pires, I., Teßmar, J., and Vorndran, E., 2014, "Direct 3D Powder Printing of Biphasic Calcium Phosphate Scaffolds for Substitution of Complex Bone Defects," Biofabrication, **6**(1), pp. 1–12.

[16] Fierz, F. C., Beckmann, F., Huser, M., Irsen, S. H., Leukers, B., Witte, F., Degistirici, Ö., Andronache, A., Thie, M., and Müller, B., 2008, "The Morphology of Anisotropic 3D-Printed Hydroxyapatite Scaffolds," Biomaterials, **29**(28), pp. 3799–3806.

[17] Seitz, H., Deisinger, U., Leukers, B., Detsch, R., and Ziegler, G., 2009, "Different Calcium Phosphate Granules for 3-D Printing of Bone Tissue Engineering Scaffolds," Adv. Eng. Mater., **11**(5), pp. 41–46.

[18] Seidenstuecker, M., Kerr, L., Bernstein, A., Mayr, H., Suedkamp, N., Gadow, R., Krieg, P., Hernandez Latorre, S., Thomann, R., Syrowatka, F., and Esslinger, S., 2017, "3D Powder Printed Bioglass and β-Tricalcium Phosphate Bone Scaffolds," Materials (Basel)., **11**(13), pp. 1–21.

[19] Suwanprateeb, J., Sanngam, R., and Panyathanmaporn, T., 2010, "Influence of Raw Powder Preparation Routes on Properties of Hydroxyapatite Fabricated by 3D Printing Technique," Mater. Sci. Eng. C, **30**(4), pp. 610–617.

[20] Raghupathy, B. P. C., and Binner, J. G. P., 2011, "Spray Granulation of Nanometric Zirconia Particles," J. Am. Ceram. Soc., **94**(1), pp. 42–48.

[21] Moritz, T., and Nagy, A., 2002, "Preparation of Super Soft Granules from Nanosized Ceramic Powders by Spray Freezing," J. Nanoparticle Res., **4**(5), pp. 439–448.

[22] Binner, J., and Vaidhyanathan, B., 2008, "Processing of Bulk Nanostructured Ceramics," J. Eur. Ceram. Soc., **28**(7), pp. 1329–1339.

[23] Ghanizadeh, S., Ramanujam, P., Vaidhyanathan, B., and Binner, J., 2016, "Spray Freeze Granulation of Submicrometre α-Alumina Using Ultrasonication," J. Ceram. Sci. Technol., **7**(4), pp. 455–461.

[24] Zhang, Y., Binner, J., Rielly, C., and Vaidhyanathan, B., 2014, "Comparison of Spray Freeze Dried Nanozirconia Granules Using Ultrasonication and Twin-Fluid Atomisation," J. Eur. Ceram. Soc., **34**(4), pp. 1001–1008.

[25] Liu, W., and Zhipeng, X., 2015, "Spray Freeze Granulation of Submicron Alumina and Its Sintering Behavior via Spark Plasma Sintering," Sci. Sinter., **47**(3), pp. 279–288.

[26] Yang, J., Sliva, A., Banerjee, A., Dave, R. N., and Pfeffer, R., 2005, "Dry Particle Coating for Improving the Flowability of Cohesive Powders," Powder Technol., **158**(1–3), pp. 21–33.

7. GRANULATING NANOPARTICLES TO MICRON-SIZED GRANULES: COMPARING FLOWABILITY AND SINTERABILITY AMONG NANOPOWDER, MICROPOWDER, AND GRANULATED POWDER*

7.1. Introduction

Additive manufacturing, also known as 3D printing, has many advantages, including the elimination of special tooling, flexible and customizable design, and efficient usage of raw materials. Binder jetting is one of the seven additive manufacturing technologies defined by ASTM and ISO [1]. When binder jetting is used to fabricate a part, a powder bed is first formed, then a green part is created by selectively jetting a liquid binder onto the powder bed, and finally the green part is densitified by sintering [1]. Advantages of binder jetting include complimentary support and ease of debinding [2,3]. The feedstock powders used in binder jetting include nanopowder (or submicron powder) [4–7], micropowder [8–14], and granulated powder [7,15–23]. Granulated powder is often prepared from nanopowder, and the granule size is usually in the micrometer range [21–23].

Flowability, the ability of a powder to freely flow, is crucial for uniform powder spreading and thus homogeneous microstructure in green and sintered parts [2]. A flowability comparison can help select a suitable feedstock powder to avoid spreading-induced defects in the powder bed and consequently in green and sintered parts. Flowability is a result of a complex combination of material properties. Particle size is a critical variable that determines the powder flowability [2]. There are some studies in the literature on comparing the flowability among different feedstock powders. For example, Miao et al. [7] investigated the effect of granulation on the powder

*Reprinted with permission from "Comparison of Flowability and Sinterability among Different Binder Jetting Feedstock Powders: Nanopowder, Micropowder, and Granulated Powder" by Du, W., Miao, G., Pei, Z., and Ma, C., 2021. Journal of Micro- and Nano-Manufacturing, 2021, 9(2): 021008 (8 pages), Copyright [2021] by ASME.

flowability. By comparing the raw nanopowder and granulated powder using various flowability metrics, it was concluded that the granulated powder had a higher flowability than the raw nanopowder. In other studies, flowability was compared across micropowders with different particle sizes [8–14]. Flowability was also compared across granulated powders from different granulation processes [15,16], such as spray drying and milling in Suwanprateeb et al.'s study [15]. Moreover, the effects of granule composition on various flowability metrics of granulated powder were reported [17–21]. However, knowledge gaps exist in the literature for the flowability of binder jetting feedstock powders. First, the flowability of granulated powder has not been compared with that of micropower of a similar size. In addition, the hierarchical (intragranular and intergranular) packing structure of granules has not been considered in the flowability comparison.

Sinterability, the ability of the powder to be densely sintered, is often used to compare the sintering performance of different powders under similar packing conditions [2,3]. A sinterability comparison can help select a suitable feedstock powder to achieve a desired printed and sintered density. Sinterability is usually characterized from pressed samples to ensure similar packing conditions across different powders. For example, a granulated powder was prepared by spray drying from a tricalcium phosphate powder mixed with a polyvinyl butyral powder as a binder [18]. The effect of fraction of binder added to the granulated powder on its sinterability was studied by pressing and sintering. Using the same approach (i.e., pressing and sintering), the effects of granulation parameters and granule size on the sinterability of granulated powder prepared by spray freeze drying were studied [22]. However, sinterability has not been compared across different types of binder jetting feedstock powders, i.e., nanopowder, micropowder, and granulated powder.

This research aims to fill the aforementioned three knowledge gaps about flowability and sinterability of the feedstock powders used in binder jetting. In this study, a granulated powder with a granule size of ~70 μm was prepared by spray freeze drying from a nanopowder with a particle size of ~100 nm. The granulated powder, the nanopowder, and a third micropowder with a particle size of 70 μm were compared using various flowability and sinterability metrics. The hierarchical packing structure of granules was considered when comparing its apparent density (AD) and tap density (TD) with those of other two powders. Conclusions were drawn based on the comparison results.

7.2. Methods

7.2.1. Materials

Alumina nanopowder (90-187085) was acquired from Allied High Tech, USA. Alumina micropowder (26R-8S70) was acquired from Inframat, USA. The particle morphology of these two powders was characterized by a scanning electron microscope (SEM, TESCAN VEGA II LSU, Brno-Kohoutovice, Czech Republic). The particle size distribution of the micropowder was acquired by analyzing its SEM images with ImageJ. The volume-weighted mean particle size of the micropowder was then obtained.

7.2.2. Preparation of granulated powder

Spray freeze drying [7,22] was chosen as the granulation method in this study. A slurry with a solid loading of 20 vol.% was prepared from the nanopowder described above. The preparation started with adding water and alumina milling balls into a high-density polyethylene bottle with a capacity of 1000 mL. To decrease the slurry viscosity, an ammonium salt of an acrylic polymer (Dispex AA 4040 NS, BASF, Ludwigshafen, Germany) was added as a dispersant, followed by a manual shaking to evenly mix the dispersant with the water. Half the designed amount of the

nanopowder was then added, and the mixture was ball-milled (Laboratory Jar Rolling Mill, Paul O. Abbe, Wood Dale, USA). Ball milling parameters have been reported in the authors' previous publication [7]. The remaining nanopowder was evenly separated into five portions, and each portion was added to the bottle once every hour during ball milling. After all nanopowder was added, ball milling continued for 12 h. Then a sieve with an opening size of 250 μm was used to filter the slurry into a beaker, after which the slurry was ready for spray freeze drying. The spray freeze drying consisted of two steps: spray freezing and freeze drying. The procedures have been reported in the authors' previous publication [7]. The parameters for spray freezing and freeze drying are listed in Table 1. After spray freeze drying, the granulated powder was sieved to obtain a granule size range of 53–90 μm by a sieve shaker (AS 200, Retsch GmbH, Haan, Germany). A scanning electron microscope (SEM, TESCAN VEGA II LSU, Brno-Kohoutovice, Czech Republic) was used to characterize the granulated powder. Afterward, the granule size distribution was analyzed with ImageJ. The volume-weighted mean granule size of the granulated powder was then obtained.

Table 7.1 Parameters for spray freeze drying

Step	Parameter	Value
Spray freezing	Compressed air pressure (bar)	0.3
Spray freezing	Slurry feed rate (L/h)	0.5
Freeze drying	Vacuum (mbar)	1.5
Freeze drying	Tray temperature (°C)	20
Freeze drying	Ice collector temperature (°C)	-50
Freeze drying	Drying time (h)	24

7.2.3. Flowability measurement

Seven different flowability metrics, as listed in Table 2, were measured for all three powders. All measurements were repeated three times for each powder.

Table 7.2 Flowability metrics and acronyms

Flowability metric	Acronym
Apparent density	AD
Tap density	TD
Volumetric flow rate	VFR
Mass flow rate	MFR
Hausner ratio	HR
Carr index	CI
Repose angle	RA

7.2.3.1. Apparent density and tap density

Apparent density (AD) is the density of freely settled powder. A Hall flowmeter (DF-1-02, HongTuo, Dongguan, China), as illustrated in Figure 1(a) [24], was used to obtain the AD of all powders. The Hall flowmeter includes two funnels, Hall funnel (with an opening diameter of 2.5 mm) and Carney funnel (with an opening diameter of 5.0 mm). The Hall funnel was used for AD measurements of the micropowder and granulated powder. As the nanopowder could not freely fall through the Hall funnel, the Carney funnel was used to measure its AD with other conditions kept the same [25]. For each AD measurement, the mass of the empty density cup was recorded firstly. Afterward, the funnel was filled with powder while the funnel opening was blocked. The powder was then let fall, filled the cup beneath the funnel, formed a cone in the cup, and eventually overflowed from the cup. The cone was gently wiped off with a spatula, followed by weighting the cup with the powder inside. The net powder mass inside the cup was divided by the cup volume (25 cm^3, as predefined in the standard [24]) to obtain the AD of each powder.

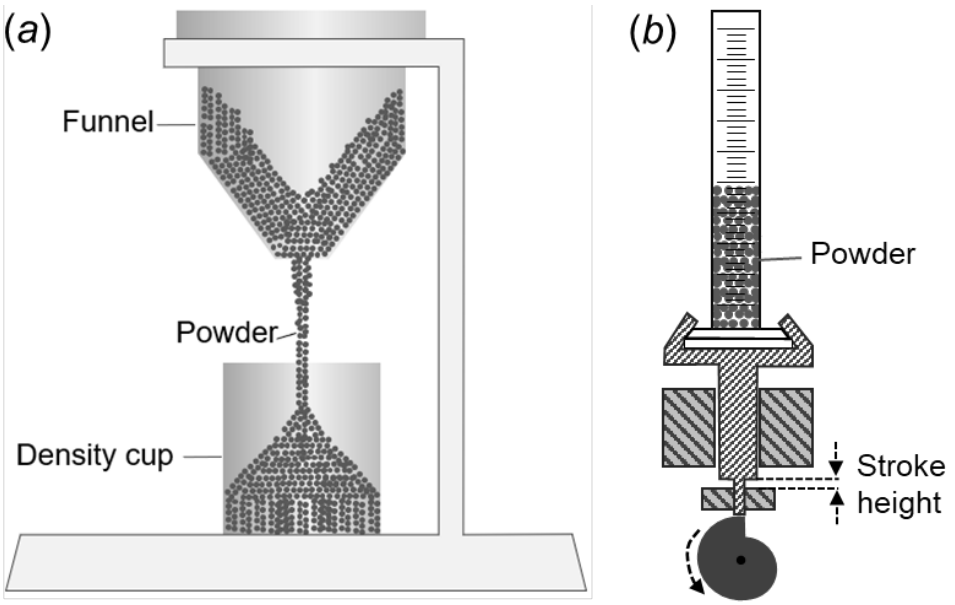

Figure 7.1 Schematics of (a) Hall flowmeter and (b) tap density meter

Tap density (TD) is the density of a powder that has been tapped, to settle contents, in a container under specified conditions [26]. As the nanopowder and granulated powder have a low density, 50 g of each powder (i.e., the powder mass specified by the standard for TD measurement [26]) had a larger volume than 100 mL (i.e., the volume of the graduated cylinder specified by the same standard [26]). Therefore, each of all three powders was filled into the cylinder to a certain volume. Specifically, each TD measurement started by weighting an empty graduated cylinder with a capacity of 100 mL. Afterward, 50 mL of powder was added into the cylinder. The cylinder with powder was then tapped 3000 times with a stroke height of 3 mm by a tap density meter (DY100-A, HongTuo, Dongguan, China), as schematically shown in Figure 1(b). The tapped volume of each powder was then recorded. The net powder mass inside the cylinder was divided by the tapped volume to obtain the TD of each powder.

7.2.3.2. Volumetric and mass flow rates

Volumetric and mass flow rates (VFR and MFR, respectively), i.e., the volume and mass of the powder falling through a funnel in unit time, respectively, were measured by the same Hall

flowmeter as shown in Figure 1(a). The measurement started with blocking the funnel opening with a piece of tape. Since both the nanopowder and granulated powder have a low density, 50 g of each powder, which is the specified powder mass in the measurement standard [27], has a larger volume than the funnel capacity. Therefore, when all three powders were measured, the funnel was filled to full instead of to a specified mass. To determine the net volume inside the funnel, the funnel was filled with water, followed by measuring the funnel mass with water in it. The net water mass was divided by the water density at the measurement temperature to calculate the net volume, which is the same as the net powder volume. The funnel was then filled with the powder until it overflowed from the periphery of the funnel. Afterward, the powder above the top surface was gently wiped off by a spatula, followed by weighting the funnel and the powder inside. Then the mass of empty funnel was subtracted from the mass of funnel with powder inside to determine the net powder mass. The time that the powder completely passed through the funnel was recorded. The net powder volume and mass inside the funnel were divided by the time to obtain the VFR and MFR, respectively.

7.2.3.3. Hausner ratio and Carr index

Hausner ratio (HR) and Carr index (CI) are two closely-related empirical metrics to assess the powder flowability. They are defined by the following equations [2]:

$$HR = \frac{\rho_t}{\rho_a} \tag{1}$$

$$CI = 100\left(1 - \frac{\rho_a}{\rho_t}\right) \tag{2}$$

where ρ_t and ρ_a are absolute TD and AD, respectively.

7.2.3.4. Repose angle

As illustrated in Figure 1(a), the Hall flow meter with the Hall funnel was used to measure the

repose angle (RA) of the micropowder and granulated powder [28] while the Hall flow meter with the Carney funnel for the nanopowder because it could not freely fall through the Hall funnel. The funnel opening was blocked first, followed by filling the funnel with powder. Afterward, the powder fell through the funnel, filled the cup beneath the funnel, formed a cone in the cup, and eventually overflowed from the cup. The diameter of the cone base (d) and the height of the cone (H) were measured by imaging the cone and processing the images with ImageJ. The following equation was used to calculate the RA (θ):

$$\theta = \tan^{-1}(2H/d) \tag{3}$$

7.2.4. Sinterability measurement

Sinterability has different definitions in the literature [29–31]. In this study, it is considered as one of the powder properties. Therefore, the sinterability measurement procedures were purposefully designed to press the powder into a disk to reach a high green density before sintering. In this way, the sintering process started from a favorable initial state, unleashing the full densification potential of the powder.

Three different sinterability metrics, as listed in Table 3, were employed for all three powders. All measurements were repeated three times for each powder.

Table 7.3 Sinterability metrics and acronyms

Sinterability metric	Acronym
Sintered bulk density	SBD
Volumetric shrinkage	VS
Densification ratio	DR

7.2.4.1. Sintered bulk density

Green disk samples were firstly prepared. For each sample, 1 g of powder was pressed at 100 MPa into a cylindrical disk of Φ12.7 mm by a hydraulic cold press (Carver Laboratory Press, Model C, Fred S. Carver Inc., Wabash, IL). The disk sample from the micropowder collapsed after pressing. Therefore, an aqueous solution containing 3 wt. % polyvinyl alcohol (PVA, 363138, Sigma-Aldrich, St. Louis, MO) was added to the micropowder as a binder. The micropowder and the binder solution were mixed at a mass ratio of 99.5:0.5. Since the PVA percentage is low, its effect on sintering of disk samples from the micropowder could be neglected. Then the mixture was put in an oven with a temperature of 60 °C for 0.5 h to evaporate the water, followed by pressing.

Sintering of all green disk samples from all three powders was conducted in a bench-top muffle furnace (KSL-1700X-A1-UL, MTI Corp., CA). The sintering temperature was 1600 °C, ramp rate was 5 °C/min, and sintering time was 2 h. The samples were cooled inside the furnace to room temperature after sintering.

Sintered bulk density (SBD) of the disk samples was measured with the Archimedes method based on an ISO standard [32] using a density measurement kit (Torbal AGCN200, Scientific Industries Inc., NY). A schematic of the measurement process is shown in Figure 2. Specifically, the dry mass of the sintered sample (m_{s1}) was firstly measured. Then the sample was boiled in deionized water for 2 h and then cooled to room temperature. This step allowed the open pores to be filled with water. The immersed mass of the sintered sample (m_{s2}) was measured. Afterward, the sample was wiped with a wet cloth to remove the water droplets on the surface. The cloth was previously saturated by water completely to avoid drawing out the water from the open pores of the sample. The soaked mass (i.e., the mass of the solid plus the water inside the open pores) of sintered sample (m_{s3}) was lastly measured. The bulk volume (i.e., the volume of the solid, the

closed pores, and the open pores) of the sintered sample (V_s) was calculated based on the following equation:

$$V_s = \frac{m_{s3} - m_{s2}}{\rho_{wt}} \tag{4}$$

where ρ_{wt} is the absolute water density at the temperature during the measurement. Finally, the relative sintered bulk density (ρ_s') was calculated with the following equation:

$$\rho_s' = \frac{m_{s1}}{V_s} \cdot \frac{1}{\rho_{th}} \times 100\% \tag{5}$$

where ρ_{th} is the theoretical density of alumina (i.e., 3.97 g/cm^3 [29]).

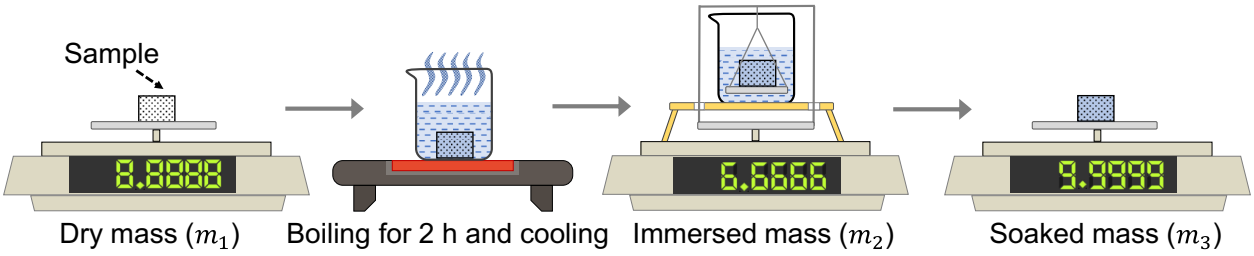

Figure 7.2 Procedures of the Archimedes method

7.2.4.2. Volumetric shrinkage and densification ratio

Green bulk volume and density were measured to determine the volumetric shrinkage and densification ratio. The diameter and thickness of the green disk samples were measured three times at different locations of the sample by a caliper (with an accuracy of 10 μm). Afterward, the green bulk volume (V_g) was calculated.

The volumetric shrinkage (S_V) is the sintering-induced volume reduction divided by the green bulk volume. It was calculated based on the following equation:

$$S_V = \left(\frac{V_g - V_s}{V_g}\right) \times 100\% \tag{6}$$

The mass (m_g) of the green disk samples was measured by a balance. The relative green bulk

density (ρ_g') of the samples was calculated based on the following equation:

$$\rho_g' = \frac{m_g}{V_g} \cdot \frac{1}{\rho_{th}} \times 100\% \quad (7)$$

The densification ratio (R_d) is the ratio of the sintering-induced density increase to the difference between the theoretical density and green bulk density. It was calculated based on the following equation:

$$R_d = \frac{\rho_s' - \rho_g'}{1 - \rho_g'} \times 100\% \quad (8)$$

7.3. Results and Discussion

7.3.1. Particle morphology and particle (granule) size of three powders

Figure 3(a) shows the SEM images of some particles from the nanopowder before ball milling. The nanopowder consisted of irregular agglomerates with a wide size range. After ball milling, the large agglomerates were crushed into nanoparticles, as shown in Figure 3(b). The particle size of the nanopowder is about 100 nm.

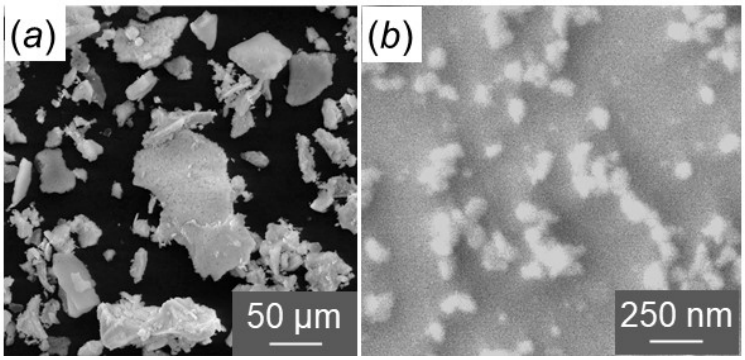

Figure 7.3 SEM images of nanopowder: (a) before ball milling and (b) after ball milling

Figure 4 shows morphology of the micropowder and granulated powder. Particles in both powders are almost perfectly spherical. Figure 5 shows the particle (granule) size distribution of

these two powders. The mean sizes for the micropowder and granulated powder are 77.4 μm and 69.2 μm, respectively.

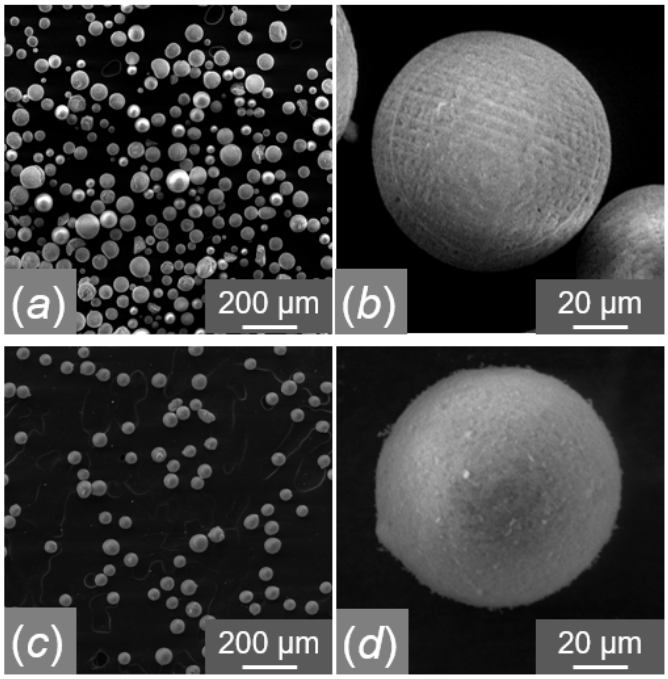

Figure 7.4 SEM images of some particles from (a) and (b) micropowder, and (c) and (d) granulated powder

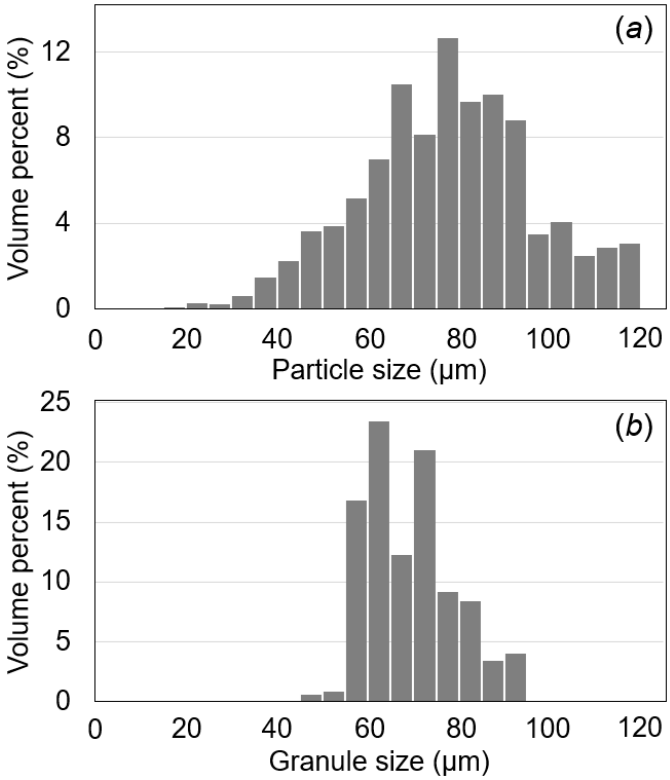

Figure 7.5 Particle (granule) size distribution of (a) micropowder and (b) granulated powder

7.3.2. Flowability

7.3.2.1. Apparent density and tap density

The measured absolute and relative values of apparent density (AD) and tap density (TD) of the three powders are listed in Table 4. The standard deviation was calculated based on three measurements for each powder. Both metrics are basic indexes of bulk density to indicate the powder flowability [33]. A powder with a low flowability has a low bulk density (i.e., low AD and TD). A powder with a high flowability, on the contrary, has a high bulk density (i.e., high AD and TD).

Table 7.4 Apparent density and tap density of three powders

Powder	Absolute apparent density (g/cm^3)	Relative apparent density (%)	Absolute tap density (g/cm^3)	Relative tap density (%)
Nanopowder	0.29±0.001	7.2±0.03	0.55±0.012	13.8±0.31
Micropowder	2.09±0.004	52.5±0.11	2.38±0.019	59.8±0.47
Granulated powder	0.46±0.006	11.6±0.15	0.56±0.007	14.2±0.17
Granulated powder (monolithic)	/	58.0±3.75	/	71.0±4.25

The comparisons of AD and TD between the nanopowder and granulated powder result in similar findings to the previous study [7]: the nanopowder has a lower AD than the granulated powder while these two powders have a similar TD. However, the hierarchical packing structure of granules in granulated powder was not considered in the previous publication [7]. This consideration is discussed as follows.

The relative AD and TD of the granulated powder (ρ'_{gra}) are governed by the relative packing density of the monolithic granules within the occupied macroscopic space (i.e., intergranular density, ρ'_{interg}) and the relative packing density of nanoparticles within a granule (i.e., intragranular density, ρ'_{intrag}), as schematically illustrated in Figure 6. The relation among these relative packing densities is given by:

$$\rho'_{gra} = \rho'_{interg} \cdot \rho'_{intrag} \tag{9}$$

As granules are the smallest units when a granulated powder flows, relative AD and TD of monolithic granules should be assessed for evaluating its flowability. Therefore, the relative AD and TD of monolithic granules (ρ'_{interg}) [34] were calculated by Equation (9), as listed in Table 4. The relative packing density of nanoparticles within a granule (ρ'_{intrag}) was assumed to be the solid loading of the slurry for spray freezing (20 vol.%). This assumption is fair because of no significant volume change during the freezing and drying processes of the employed granulation

method, as experimentally shown in other work [34,35].

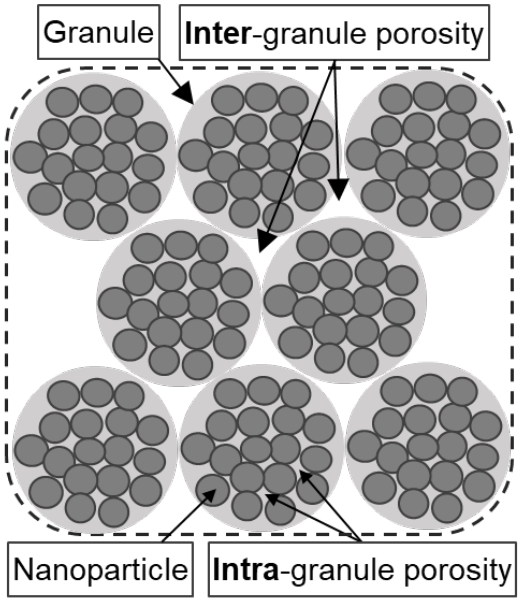

Figure 7.6 Packing structure of granulated powder

With the hierarchical packing structure of granulated powder considered, the relative AD and TD of the monolithic granules (as shown in Table 4) are much higher than those of the nanopowder. This finding makes sense considering the severe agglomeration and irregular agglomerate shape of the nanopowder.

The relative AD of the monolithic granules, 58.0%, is higher than that of the micropowder, 52.5%. The relative TD of the monolithic granules, 71.1%, is also higher than that of the micropowder, 59.8%. The difference in relative TD (11.3%) between these two powders is larger than that in relative AD (5.5%). It could be attributed to the porous structure and thus low strength of the granules. This can lead to plastic deformation and fracture of the granules [36] during the tapping, decreasing the intergranular porosity and increasing the packing density of the monolithic granules.

7.3.2.2. Volumetric and mass flow rates

The volumetric and mass flow rates (VFR and MFR, respectively) of the three powders are listed in Table 5. It should be noted that VFR and MFR cannot be measured for the nanopowder due to the dominant interparticle cohesion and large interagglomerate friction. Therefore, the volumetric and mass flow rates are not suitable metrics to characterize the flowability of the nanopowder.

Table 7.5 Volumetric and mass flow rates of three powders

Powder	Volumetric flow rate (cm^3/s)	Mass flow rate (g/s)
Nanopowder	/	/
Micropowder	0.70±0.01	1.54±0.01
Granulated powder	0.30±0.01	0.15±0.01

The micropowder has a VFR value that is about twice that of the granulated powder. This could be explained by their different apparent densities. As the powder was freely settled in the funnel before the measurements of flow rates, the absolute powder packing density in the funnel (ρ_f, 2.19 g/cm^3 and 0.48 g/cm^3 for the micropowder and granulated powder, respectively) was close to the absolute AD (ρ_a, 2.09 g/cm^3 and 0.46 g/cm^3 for the micropowder and granulated powder, respectively). The micropowder has a larger AD and thus a larger gravity-induced pressure at the funnel opening. Therefore, the micropowder has a larger VFR.

The difference in MFR between the micropowder and granulated powder is more significant than that in VFR. This could be explained by the relationship among MFR, VFR, and absolute powder packing density in the funnel (approximately, absolute AD) as follows:

$$Q_m = Q_V \cdot \rho_f \approx Q_V \cdot \rho_a \tag{10}$$

where Q_m is the MFR, Q_V is the VFR, ρ_f is the absolute powder packing density in the funnel, and ρ_a is the absolute AD. This equation suggests that the difference in MFR between two powders

is actually a product of differences in both VFR and AD. It means that MFR is even more dependent on AD. Since both the VFR and MFR are heavily dependent on the powder packing density itself, they are not suited for comparing the flowability of different powders.

7.3.2.3. Hausner ratio and Carr index

Both Hausner ratio (HR) and Carr index (CI) represent the difference between AD and TD. When AD is measured, a cohesive powder (i.e., of a low flowability) obtains a loose packing structure after free falling from the funnel while a free-flowing powder (i.e., of a high flowability) obtains a relatively dense packing structure [33]. When TD is measured, the loose packing structure of a cohesive powder (i.e., of a low flowability) changes under tapping and its packing density increases significantly, resulting in a large difference between the AD and TD. On the contrary, a free-flowing powder (i.e., of a high flowability) has little room for further rearrangement due to the already dense packing structure induced by gravity during free falling, and thus its packing density only slightly increases after tapping [33].

Table 6 lists the HR and CI values of the three powders. Based on the definition, the smaller the HR (i.e., closer to one), the higher the flowability. Both the micropowder and granulated powder achieved relatively small HR values while the nanopowder had a relatively large HR value. For CI, the same rule applies: the smaller the CI (i.e., closer to zero), the higher the flowability. Similar trends were observed on CI. It should be noted that the HR and CI values of the granulated powder are slightly higher than those of the micropowder. One possible reason is the plastic deformation or fracture of the granules during tapping and thus an unusually high tap density of the monolithic granules (as listed in Table 4).

Table 7.6 Hausner ratio and Carr index of three powders

Powder	Hausner ratio	Carr index
Nanopowder	1.93±0.04	48.15±0.96
Micropowder	1.14±0.01	12.17±0.58
Granulated powder	1.23±0.02	18.66±1.20

7.3.2.4. Repose angle

Table 7 and Figure 7 show the repose angle (RA) values of all three powders. The granulated powder achieved an RA close to that of the micropowder. Both the RA values of these two powders are much smaller than that of the nanopowder. This is probably due to the much less interparticle (or intergranular) cohesion.

Table 7.7 Repose angle of three powders

Powder	Repose angle (°)
Nanopowder	67.80±5.80
Micropowder	25.22±0.59
Granulated powder	29.88±0.49

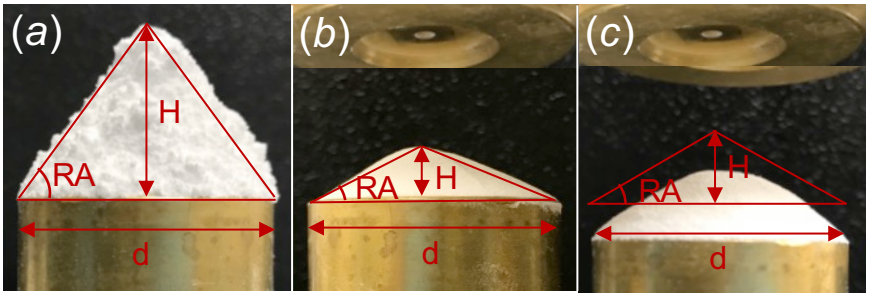

Figure 7.7 Measurements of repose angle for (a) nanopowder, (b) micropowder, and (c) granulated powder

7.3.2.5. Summary of flowability

Normalized values for five flowability metrics are summarized in Figure 8. Flowability values of the micropowder were set as the baseline to obtain the normalized values of each flowability

metric for clear comparisons among different powders. High flowability is associated with large AD and TD and small HR, CI, and RA. The VFR and MFR are not summarized because they are not suitable for comparing the flowability of different powders as discussed in Section 3.2.2.

All flowability metrics show a large difference between the nanopowder and micropowder while a small difference between the micropowder and granulated powder. Specifically, AD and TD suggest the flowability of the granulated powder is slightly higher than that of the micropowder while HR, CI, and RA suggest the opposite. These results indicate the flowability of the granulated powder is comparable to that of the micropowder.

Moreover, the consideration of the hierarchical packing structure of granules in granulated powder makes AD and TD more appropriate for comparing its flowability with other powders. With this consideration, AD and TD of granulated powder are significantly larger than those of the nanopowder, which agrees with the results of other flowability metrics.

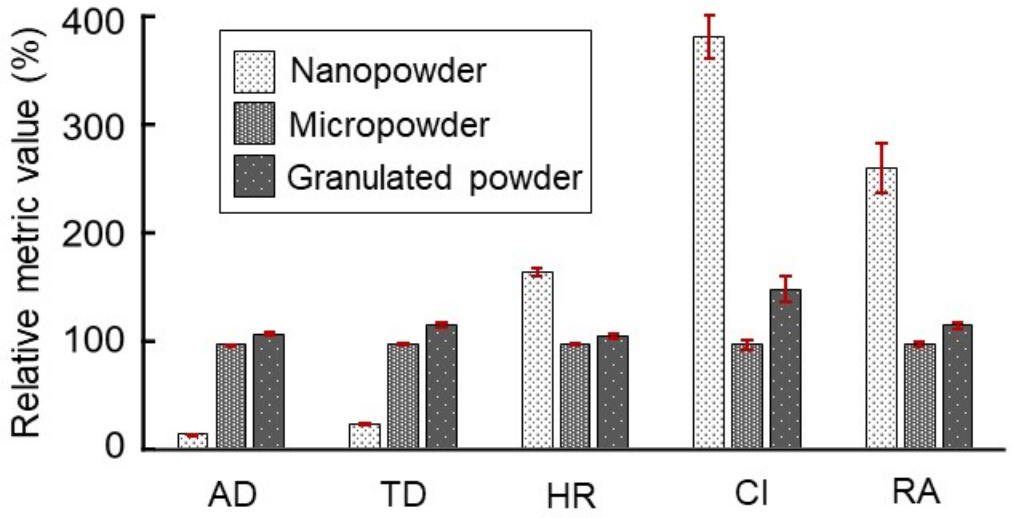

Figure 7.8 Normalized values for different flowability metrics, including apparent density (AD), tap density (TD), Hausner ratio (HR), Carr index (CI), and repose angle (RA)

7.3.3. Sinterability

7.3.3.1. Sintered bulk density

Results for relative sintered bulk density (SBD) are listed in Table 8. As a smaller particle size corresponds to a higher sintering driving force, more significant densification occurred for the nanopowder and granulated powder than the micropowder, leading to higher SBD values. The relative SBD values of the granulated powder and the nanopowder are close since the granulated powder has the same primary particle size (i.e., ~100 nm) as the nanopowder.

Table 7.8 Relative sintered bulk density of three powders

Powder	Relative sintered bulk density (%)
Nanopowder	89.7±0.8
Micropowder	62.4±2.7
Granulated powder	96.9±1.3

7.3.3.2. Volumetric shrinkage and densification ratio

Results for volumetric shrinkage (VS) and densification ratio (DR) are listed in Table 9. The nanopowder and granulated powder have comparably large values of VS, indicating the high sinterability of these two powders. The micropowder has only a limited VS value, suggesting the low sinterability of the micropowder. Similarly, the nanopowder and granulated powder have much higher DR values than the micropowder. Both VS and DR values of the granulated powder are close to those of the nanopowder as the granulated powder has the same primary particle size (i.e., ~100 nm) as the nanopowder.

Table 7.9 Volumetric shrinkage and densification ratio of three powders

Powder	Volumetric shrinkage (%)	Densification ratio (%)
Nanopowder	61.2±1.6	83.9±2.3
Micropowder	5.2±3.7	7.1±1.0
Granulated powder	57.2±1.4	94.5±1.9

7.3.3.3. Summary of sinterability

All sinterability metrics, as summarized in Figure 9, show a large difference between the nanopowder and micropowder while a small difference between the nanopowder and granulated powder. Specifically, SBD and DR suggest the sinterability of the granulated powder is slightly higher than that of the nanopowder while VS suggests the opposite. This indicates that the sinterability of the granulated powder is comparable to that of the nanopowder.

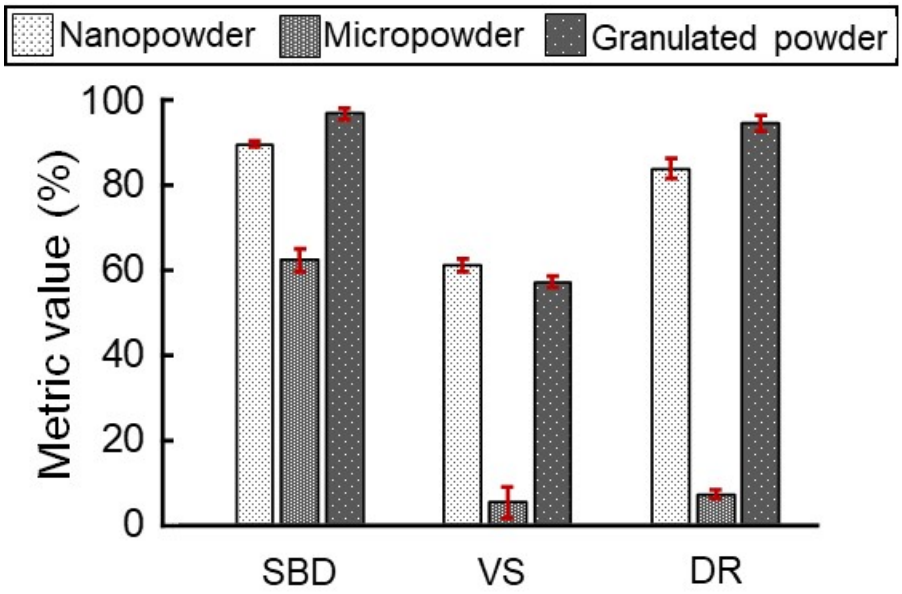

Figure 7.9 Sinterability results of three powders, including relative sintered bulk density (SBD), volumetric shrinkage (VS), and densification ratio (DR)

7.4. Conclusions

This study compares the flowability and sinterability of three types of feedstock powders for binder jetting additive manufacturing, i.e., nanopowder, micropowder, and granulated powder. Various flowability metrics employed include apparent density, tap density, volumetric flow rate, mass flow rate, Hausner ratio, Carr index, and repose angle. Various sinterability metrics employed include sintered bulk density, volumetric shrinkage, and densification ratio.

Experimental data on all metrics indicate that the nanopowder has a significantly lower flowability than the micropowder and granulated powder (with the hierarchical packing structure

considered). The flowability comparison between the granulated powder and micropowder using different metrics has slightly different results. Results on apparent density and tap density indicate that the flowability of the granulated powder is slightly higher while results on Hausner ratio, Carr index, and repose angle indicate that the flowability of the micropowder is slightly higher. Therefore, it is concluded that these two powders have a comparable flowability. Moreover, the consideration of the hierarchical packing structure of the granulated powder makes apparent density and tap density more appropriate for comparing its flowability with other powders.

Experimental data on all metrics indicate that the micropowder has a significantly lower sinterability than the granulated powder and nanopowder. The sinterability comparison between the granulated powder and nanopowder using different metrics has slightly different results. Experimental data on sintered bulk density and densification ratio indicate that the sinterability of the granulated powder is slightly higher while experimental data on volumetric shrinkage indicate that the sinterability of the nanopowder is slightly higher. Therefore, it is concluded that these two powders have a comparable sinterability.

In a nutshell, the micropowder has a high flowability but a low sinterability, the nanopowder has a low flowability but a high sinterability, and the granulated powder has both a high flowability and a high sinterability.

This comparison study of flowability and sinterability among nonopowder, micropower, and gtranulate powder has follwing impacts on binder jetting: (1) it can guide the selection of a proper feedstock powder to avoid spreading-induced defects and achieve a desired printed and sintered density; (2) it confirms that granulated powder has relatively high flowability and high sinterability, and is a promising binder jetting feedstock powder.

7.5. References

[1] ASTM International/International Standard, 2015, “ISO/ASTM 52900:2015 - Additive Manufacturing — General Principles — Terminology.”

[2] Du, W., Ren, X., Pei, Z., and Ma, C., 2020, “Ceramic Binder Jetting Additive Manufacturing: A Literature Review on Density,” Journal of Manufacturing Science and Engineering, **142**(4), p. 040801 (19 pages).

[3] Li, M., Du, W., Elwany, A., Pei, Z., and Ma, C., 2020, “Metal Binder Jetting Additive Manufacturing: A Literature Review,” Journal of Manufacturing Science and Engineering, **142**(9), p. 090801 (17 pages).

[4] Qian, C., and Sun, J., 2013, “Fabrication of the Porous Hydroxyapatite Implant by 3D Printing,” Journal of Ceramic Processing Research, **14**(4), pp. 513–516.

[5] Tarafder, S., Davies, N. M., Bandyopadhyay, A., and Bose, S., 2013, “3D Printed Tricalcium Phosphate Bone Tissue Engineering Scaffolds: Effect of SrO and MgO Doping on in Vivo Osteogenesis in a Rat Distal Femoral Defect Model,” Biomaterials Science, **1**(12), pp. 1250–1259.

[6] Tarafder, S., Dernell, W. S., Bandyopadhyay, A., and Bose, S., 2015, “SrO- and MgO-Doped Microwave Sintered 3D Printed Tricalcium Phosphate Scaffolds: Mechanical Properties and in Vivo Osteogenesis in a Rabbit Model,” Journal of Biomedical Materials Research - Part B Applied Biomaterials, **103**(3), pp. 679–690.

[7] Miao, G., Du, W., Moghadasi, M., Pei, Z., and Ma, C., 2020, “Ceramic Binder Jetting Additive Manufacturing: Effects of Granulation on Properties of Feedstock Powder and Printed and Sintered Parts,” Additive Manufacturing, **36**, p. 101542.

[8] Bai, Y., Wagner, G., and Williams, C. B., 2015, “Effect of Bimodal Powder Mixture on Powder Packing Density and Sintered Density in Binder Jetting of Metals,” *International*

Solid Freeform Fabrication Symposium, Austin, TX, pp. 758–771.

[9] Butscher, A., Bohner, M., Roth, C., Ernstberger, A., Heuberger, R., Doebelin, N., Rudolf Von Rohr, P., and Müller, R., 2012, "Printability of Calcium Phosphate Powders for Three-Dimensional Printing of Tissue Engineering Scaffolds," Acta Biomaterialia, **8**(1), pp. 373–385.

[10] Zocca, A., Gomes, C. M., Bernardo, E., Muller, R., Gunster, J., and Colombo, P., 2013, "LAS Glass-Ceramic Scaffolds by Three-Dimensional Printing," Journal of the European Ceramic Society, **33**(9), pp. 1525–1533.

[11] Lanzetta, M., and Sachs, E., 2001, "The Line Formation with Alumina Powders in Drop on Demand Three Dimensional Printing," *The First International Seminar on Progress in Inovative Manufacturing Engineering*, Sestri Levante, pp. 197–204.

[12] Sun, C., Tian, X., Wang, L., Liu, Y., Wirth, C. M., Günster, J., Li, D., and Jin, Z., 2017, "Effect of Particle Size Gradation on the Performance of Glass-Ceramic 3D Printing Process," Ceramics International, **43**(1), pp. 578–584.

[13] Du, W., Ren, X., Chen, Y., Ma, C., Radovic, M., and Pei, Z., 2018, "Model Guided Mixing of Ceramic Powders with Graded Particle Sizes in Binder Jetting Additive Manufacturing," *ASME 2018 13th International Manufacturing Science and Engineering Conference*, College Station, TX, p. V001T01A014 (9 pages).

[14] Du, W., Roa, J., Hong, J., Liu, Y., Pei, Z., and Ma, C., 2021, "Binder Jetting Additive Manufacturing: Effect of Particle Size Distribution on Density," Journal of Manufacturing Science and Engineering, **143**(9), p. 091002 (9 pages).

[15] Suwanprateeb, J., Sanngam, R., and Panyathanmaporn, T., 2010, "Influence of Raw Powder Preparation Routes on Properties of Hydroxyapatite Fabricated by 3D Printing

Technique," Materials Science and Engineering C, **30**(4), pp. 610–617.

[16] Irsen, S. H., Leukers, B., Höckling, C., Tille, C., and Seitz, H., 2006, "Bioceramic Granulates for Use in 3D Printing: Process Engineering Aspects," Materialwissenschaft und Werkstofftechnik, **37**(6), pp. 533–537.

[17] Gildenhaar, R., Knabe, C., Gomes, C., Linow, U., Houshmand, A., and Berger, G., 2011, "Calcium Alkaline Phosphate Scaffolds for Bone Regeneration 3D-Fabricated by Additive Manufacturing," Key Engineering Materials, **493**, pp. 849–854.

[18] Ben, Y., Zhang, L., Wei, S., Zhou, T., Li, Z., Yang, H., Wang, Y., Selim, F. A., Wong, C., and Chen, H., 2017, "PVB Modified Spherical Granules of β-TCP by Spray Drying for 3D Ceramic Printing," Journal of Alloys and Compounds, **721**, pp. 312–319.

[19] Seitz, H., Deisinger, U., Leukers, B., Detsch, R., and Ziegler, G., 2009, "Different Calcium Phosphate Granules for 3-D Printing of Bone Tissue Engineering Scaffolds," Advanced Engineering Materials, **11**(5), pp. 41–46.

[20] Cox, S. C., Thornby, J. A., Gibbons, G. J., Williams, M. A., and Mallick, K. K., 2015, "3D Printing of Porous Hydroxyapatite Scaffolds Intended for Use in Bone Tissue Engineering Applications," Materials Science and Engineering C, **47**, pp. 237–247.

[21] Chumnanklang, R., Panyathanmaporn, T., Sitthiseripratip, K., and Suwanprateeb, J., 2007, "3D Printing of Hydroxyapatite: Effect of Binder Concentration in Pre-Coated Particle on Part Strength," Materials Science and Engineering C, **27**(4), pp. 914–921.

[22] Du, W., Miao, G., Liu, L., Pei, Z., and Ma, C., 2019, "Binder Jetting Additive Manufacturing of Ceramics: Feedstock Powder Preparation by Spray Freeze Granulation," *ASME 2019 14th International Manufacturing Science and Engineering Conference*, Erie, PA, p. V001T01A006 (6 pages).

[23] Du, W., Miao, G., Liu, L., Pei, Z., and Ma, C., 2019, "Binder Jetting Additive Manufacturing of Ceramics: Comparison of Flowability and Sinterability between Raw and Granulated Powders," *ASME 2019 14th International Manufacturing Science and Engineering Conference*, Erie, PA, p. V001T01A004 (8 pages).

[24] ASTM International, 2017, "B212-17: Standard Test Method for Apparent Density of Free-Flowing Metal Powders Using the Hall Flowmeter Funnel."

[25] ASTM International, 2013, "B417 2013: Standard Test Method for Apparent Density of Non-Free-Flowing Metal Powders Using the Carney Funnel."

[26] ASTM International, 2015, "B527-15: Standard Test Method for Tap Density of Metal Powders and Compounds."

[27] ASTM International, 2017, "B213-17: Standard Test Methods for Flow Rate of Metal Powders Using the Hall Flowmeter."

[28] ASTM International, 2000, "C 1444-00: Standard Test Method for Measuring the Angle of Repose of Free-Flowing Mold Powders."

[29] Kang, S.-J. L., 2005, *Sintering : Densification, Grain Growth, and Microstructure*, Elsevier Butterworth-Heinemann, Burlington.

[30] Hwang, H. J., Yasuoka, M., Sando, M., Toriyama, M., and Niihara, K., 1999, "Fabrication, Sinterability, and Mechanical Properties of Lead Zirconate Titanate/Silver Composites," Journal of the American Ceramic Society, **82**(9), pp. 2417–2422.

[31] Lara, C., Pascual, M. J., and Durán, A., 2004, "Glass-Forming Ability, Sinterability and Thermal Properties in the Systems RO-BaO-SiO2 (R = Mg, Zn)," Journal of Non-Crystalline Solids, **348**(15), pp. 149–155.

[32] ISO, 2013, "ISO 18754:2013 Fine Ceramics (Advanced Ceramics, Advanced Technical

Ceramics) – Determination of Density and Apparent Porosity."

[33] Abdullah, E. C., and Geldart, D., 1999, "The Use of Bulk Density Measurements as Flowability Indicators," Powder Technology, **102**(2), pp. 151–165.

[34] Oberacker, R., 2011, "Powder Compaction by Dry Pressing," *Ceramic Science and Technology, Volume 3: Synthesis and Processing*, R. Riedel, and I.-W. Chen, eds., John Wiley & Sons, pp. 10–14.

[35] Adolfsson, E., and Shen, Z., 2012, "Effects of Granule Density on Strength and Granule Related Defects in Zirconia," Journal of the European Ceramic Society, **32**(11), pp. 2653–2659.

[36] Cheong, Y. S., Mangwandi, C., Fu, J., Adams, M. J., Hounslow, M. J., and Salman, A. D., 2007, "A Mechanistic Description of Granule Deformation and Breakage," Handbook of Powder Technology, **12**, pp. 1055–1120.

8. GRANULATION NANOPARTICLES TO MICRON-SIZED GRANULES: EFFECTS OF POWDER PREPARATION ON POWDER BED CONDITIONS IN ROLLER-COMPACTION-ASSISTED BINDER JETTING

8.1. Introduction

Binder jetting (BJ), as one of the seven additive manufacturing (AM) technologies defined by ASTM and ISO [1], has advantages such as complimentary support structure, high scalability, and low consumption of sacrificial materials [2]. To increase the green or final densities of the part from BJ, many post-processing techniques (such as sintering, infiltration, isostatic pressing, etc.) have been reported. Among all different post-processing techniques, sintering is a favorable route because it can avoid the introduction of a different materials and provide relatively high freedom for part size and geometry. However, one challenge of BJ with the sintering route is the low printed and sintered density, and therefore inferior mechanical properties. This challenge limits the wide applications of BJ [3].

To achieve a high printed and sintered density, the BJ feedstock powder is required to have high flowability (to decrease spreading-induced defects in powder bed) and high sinterability (to achieve high sintering densification) [3]. Granulation with nanopowder is promising to meet both requirements. The nanopowder ensures high specific surface energy and therefore high sinterability, and the enlarged micron-level granule size ensures the dominance of inertia force over intergranular force and therefore high flowability. Various granulation technologies have been studied in the field of BJ, including grinding and sieving [4,5], spray drying [6,7], and spray freeze drying [8,9].

One drawback of granulated powder is the intragranular pores [8], which can decrease the powder bed density and therefore the sintered density. Powder bed compaction by forward-rotating

roller is a promising method to effectively increase the powder bed density in BJ [10–13]. This enhanced BJ process is called roller-compaction-assisted binder jetting in this paper. In the compaction step of this process, the roller rotates forward while it traverses above the powder bed, meaning the rotation tangential speed on the top surface of the roller is the same as the traverse direction.

In this paper, for the first time, powder spreading and compaction experiments with granulated powder from alumina nanopowder were conducted on a commercially available binder jetting printer equipped with forward-rotation roller compaction. A granulation method called direct freeze drying was used to prepare granulated powder. Four different granulated powders were prepared from slurries with different solid loadings (i.e., 2, 5, 10, and 15 vol.%). Apparent density for each granulated powder was characterized. The powder bed density achieved by each powder was measured. Conclusions were drawn based on the experimental results.

8.2. Methods

8.2.1. Materials and feedstock preparation

Four different granulated powders were prepared from slurries with different solid loadings, which were 2, 5, 10, and 15 vol.%. Alumina nanopowder (90-187125, Allied High Tech, Rancho Dominguez, CA) was used as the solid material in the slurry. About 800 mL of slurry was prepared for each batch. The preparation started with adding 1 kg alumina milling balls (~5.6 mm in diameter) to a high-density polyethylene bottle (with a capacity of 2 L and diameter of 67 mm). Then the nanopowder was measured by a scale and added to the bottle, followed by adding water with a corresponding volume for the desired solid loading. Moreover, a dispersant (DOLAPIX CA, ZSCHIMMER & SCHWARZ Chemie GmbH, Lahnstein, Germany) was added to two slurries with high solid loadings of 10 and 15 vol.%. The dispersant amounts added were 2 and 4 vol.%

(based on the solid volume of alumina nanopowder) for the slurries of 10 and 15 vol.%, respectively. Then each slurry was ball-milled (Jar Rolling Mills, Paul O. Abbe, Wood Dale, IL) for 48 hours at a low milling speed (~60 RPM).

After ball milling, the slurry was transferred to a circular pan with a diameter of 15 cm. Thereafter, liquid nitrogen was gradually poured into the pan until the whole slurry froze. Then the frozen slurry was put into a freeze dryer (FreeZone 2.5 L, Labconco, Kansas City, MO) for drying at a vacuum level of 2 mbar. The pan holder in the freeze dryer was heated to accelerate the drying process. The pan holder was set to a drying profile of staying at each temperature of -20, -10, 0, and 10 °C for 1 hour and then staying at 20 °C for the rest of the drying time. The total drying time was 48 hours. Right after drying, all powders were ready for sieving directly without any further comminution. All dried powders were sieved to a size range of 25–90 μm.

8.2.2. Characterization of granule morphology

The granule morphology was characterized by a scanning electron microscope (SEM, TESCAN VEGA II LSU, Brno-Kohoutovice, Czech Republic).

8.2.3. Measurement of apparent density

Apparent density was measured for each granulated powder with a Hall flowmeter [14,15]. The measurement for each granulated powder was repeated three times. Detailed measurement procedure was reported in the authors' previous publication [16].

8.2.4. Powder spreading and compaction test

The granulated powders were spread on a commercially available binder jetting printer (Innovent+, ExOne, North Huntingdon, PA), which was equipped with a forward-rotating roller compaction system. There are two critical parameters during forward-rotating roller compaction: layer thickness (LT) and compaction thickness (CT). The compaction ratio, i.e., (LT+CT)/LT,

affects the compaction significantly [10]. The larger the ratio, the higher the powder bed density after compaction. However, as the ratio increases, the powder bed density can reach a plateau and some compaction-induced defects may occur on the powder bed surface including surface ridges [10]. Therefore, an optimal compaction ratio exists that can achieve the highest powder bed density without compaction-induced defects. The method for powder spreading and compaction test is schematically shown in Figure 1. The following subsections describe this method.

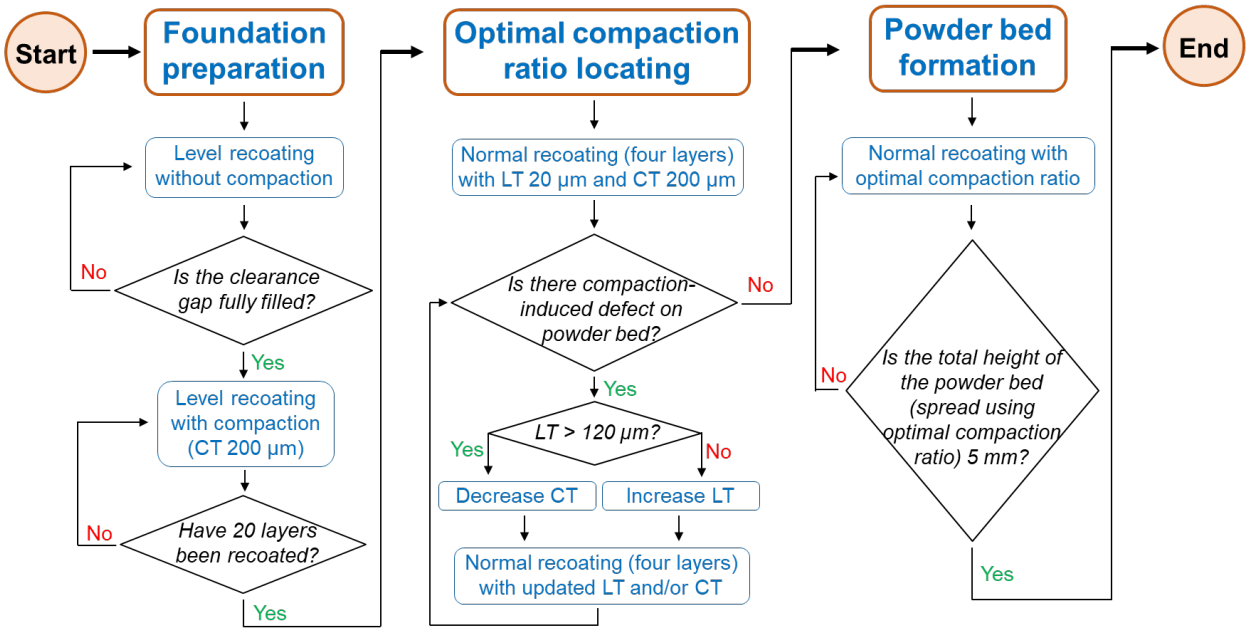

Figure 8.1 Method for powder spreading and compaction test

8.2.4.1. Foundation preparation

When the build platform (BP) rises to its topmost position, there is still a clearance gap (with a thickness of about 1.5 mm) between the roller and the BP, which needs to be fully filled first. The step to fill the gap is called foundation preparation in this study. A specific powder recoating function of the printer called level recoating was used. Level recoating can be conducted at any height between the topmost and bottommost positions of the BP. Here in this study the level recoating was conducted only when BP at its topmost position. As shown in the left column of Figure 1, the foundation preparation started with level recoating without compaction until the gap

was filled. Thereafter, level recoating with compaction was conducted using a CT of 200 μm for 20 layers. This was to obtain a dense foundation for locating the optimal compaction ratio next.

Suppose that the topmost and bottommost heights of the BP are 0 and $-B$, respectively. A level recoating without compaction works as follows:

1) As shown in Figure 2(a), at the initial stage, BP stays at its topmost position (i.e., BP at a height of 0);
2) As shown in Figure 2(b), BP descends by a specific height of h (i.e., BP at a height of $-h$ after descending);
3) As shown in Figure 2(c), the ultrasonic hopper stays above the right edge of the build box for a defined period and then traverses to dispenses the powder onto the powder bed;
4) As shown in Figure 2(d), BP rises to its topmost position (i.e., BP at a height of 0 after rising);
5) As shown in Figure 2(e), the roller counter-rotates to spread the powder.

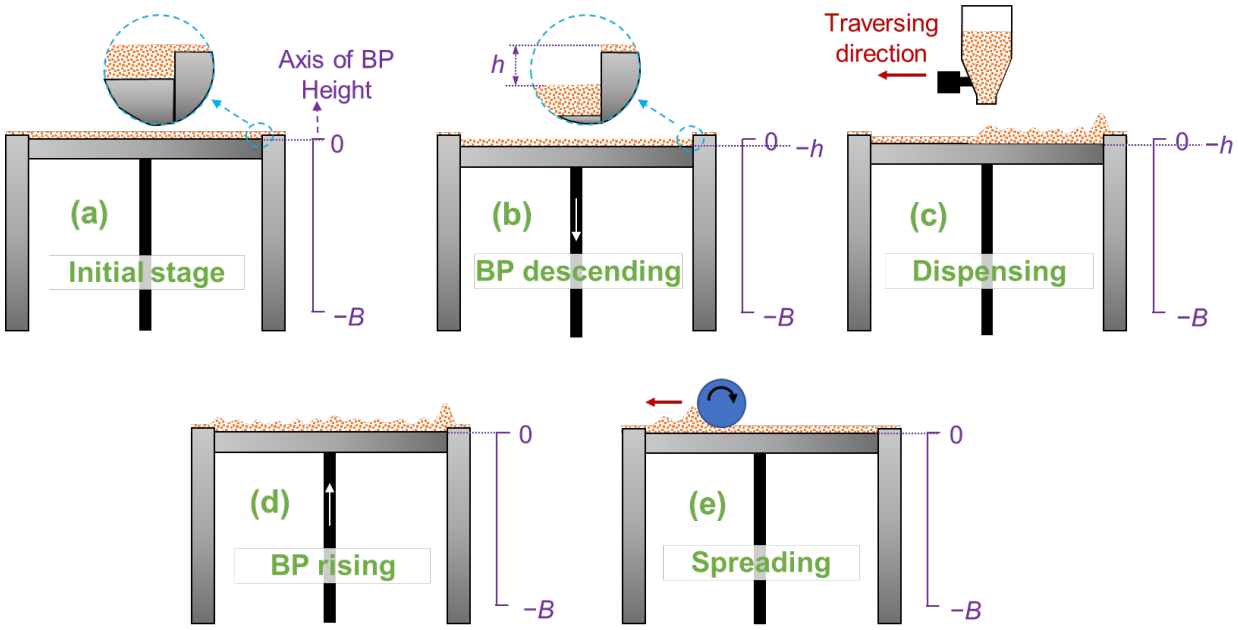

Figure 8.2 Schematic of level recoating without compaction conducted at the topmost position of the build platform (BP): (a) initial stage, (b) BP descending, (c) powder dispensing, (d) BP rising, and (e) counter-rotating roller spreading

It should be noted that the descending height of BP before powder dispensing (h, as shown in Figure 2(b)) is pre-defined by the printer software. Other parameters used for powder dispending (Figure 1(c)) and spreading (Figure 1(e)) are listed in Table 1. The screen size represents the hole size of the screen installed at the bottom of the hopper. Dispense on delay determines the dwelling time of the hopper at the beginning of dispensing above the right edge of the build box. Both ultrasonic mode and ultrasonic intensity control the output power of the ultrasonic vibration unit.

Table 8.1 Parameters of powder dispensing and spreading

Parameter	Value
Screen size (μm)	300
Ultrasonic mode	A
Ultrasonic intensity (%)	100
Dispense on delay (s)	2
Spreading roller traverse (mm/s)	5
Spreading roller rotation (rpm)	100

A level recoating with compaction conducted at the topmost position of the BP is illustrated in Figure 3. An important parameter of forward-rotating roller compaction is the number of compaction pass segments (CPS), which is controlled by the number of compaction passes in the printer software. One compaction pass (i.e., one back-and-forth traversing of forward-rotating roller) corresponds two CPS. In this study, four CPS (i.e., two compaction passes) were used for all recoatings with compaction. A level recoating with compaction through four CPS conducted at the topmost position of the BP works as follows:

1) As shown in Figure 3(a), at the initial stage, BP stays at a height of 0;
2) As shown in Figure 3(b), BP descends by a specific height of h ($CT<h<B$, and BP at a height of $-h$ after descending);
3) As shown in Figure 3(c), a hopper with ultrasonic vibration stays above the right edge of the build box for a defined period and then traverses over the BP to dispense the powder onto the powder bed;
4) As shown in Figure 3(d), BP rises to a height that is lower than its initial height of 0 by CT (i.e., BP at a height of $-CT$ after rising);

5) As shown in Figure 3(e), the roller counter-rotates to spread the dispensed powder into an un-compacted layer with a height of *CT*;

6) As shown in Figures 3(f)–(i), the BP rises by a quarter of CT in each CPS, and the roller traverses while forward-rotating to compact the spread layer, which is repeated by four times.

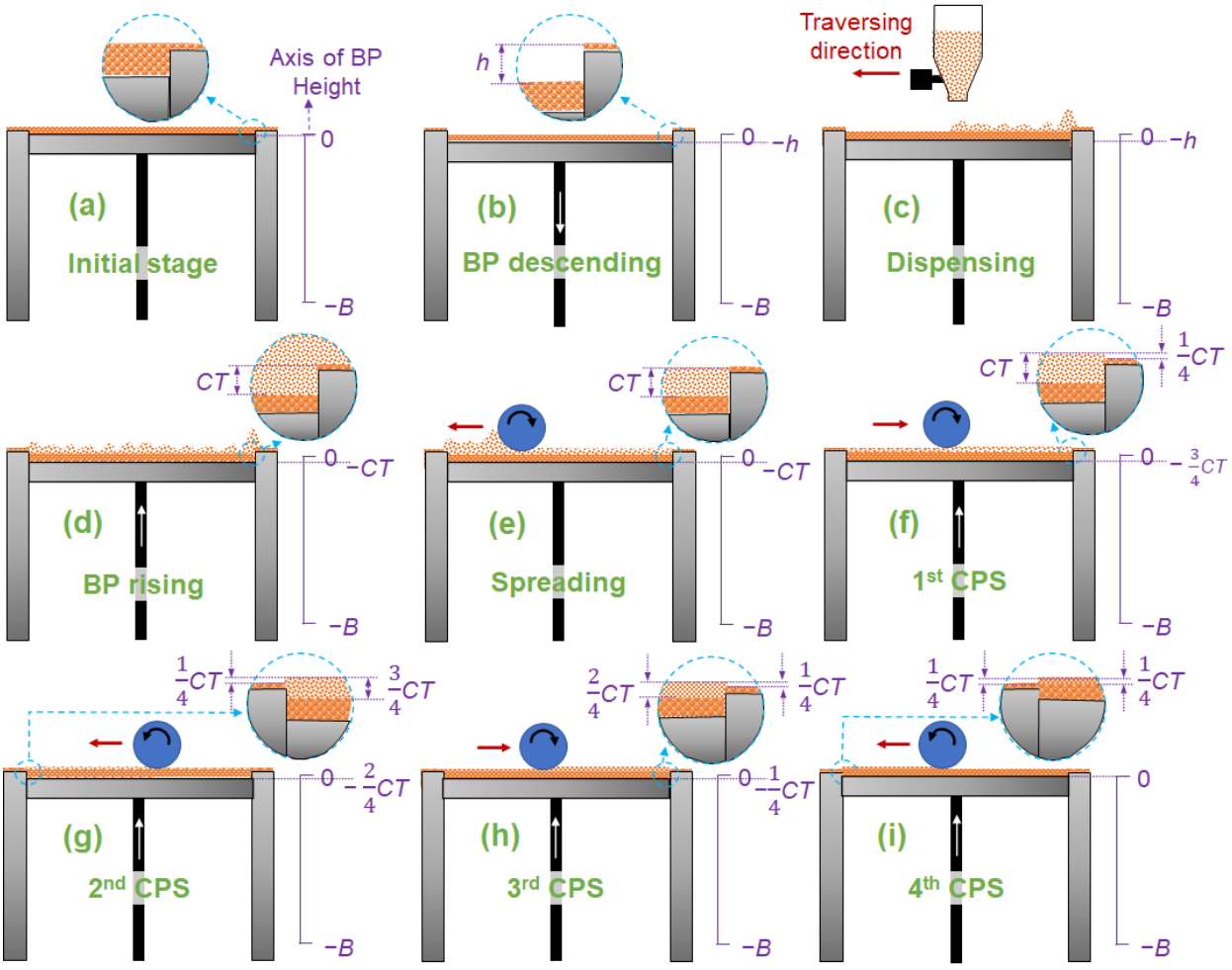

Figure 8.3 Level recoating with compaction through four compaction pass segments (CPS) conducted at the topmost position of the build platform (BP): (a) initial stage, (b) BP descending, (c) powder dispensing, (d) BP rising, (e) counter-rotating roller spreading, (f) first CPS, (g) second CPS, (h) third CPS, and (i) fourth CPS

Parameters of powder dispending (Figure 3(c)) and spreading (Figure 3(e)) used in level recoating with compaction are the same as those used before (listed in Table 1). Moreover, other parameters used for powder bed compaction are listed in Table 2.

Table 8.2 Parameters for forward-rotating roller compaction

Parameter	Value
Compaction pass	2
Compaction roller traverse (mm/s)	5
Roller diameter in software (mm)	12

8.2.4.2. Optimal compaction ratio locating

To find the optimal compaction ratio (i.e., the highest (LT+CT)/LT ratio without compaction-induced defects), a specific powder recoating function of the printer called normal recoating with compaction was used. A normal recoating with compaction through four CPS conducted at an arbitrary BP position of $-b$ is illustrated in Figure 4. It should be noted that b is smaller than B. To compare all three kinds of recoating functions in Figures 2–4, their differences are summarized in Table 3. Parameters for powder dispensing, spreading, and compaction are the same as used in foundation preparation (as listed in Tables 1 and 2).

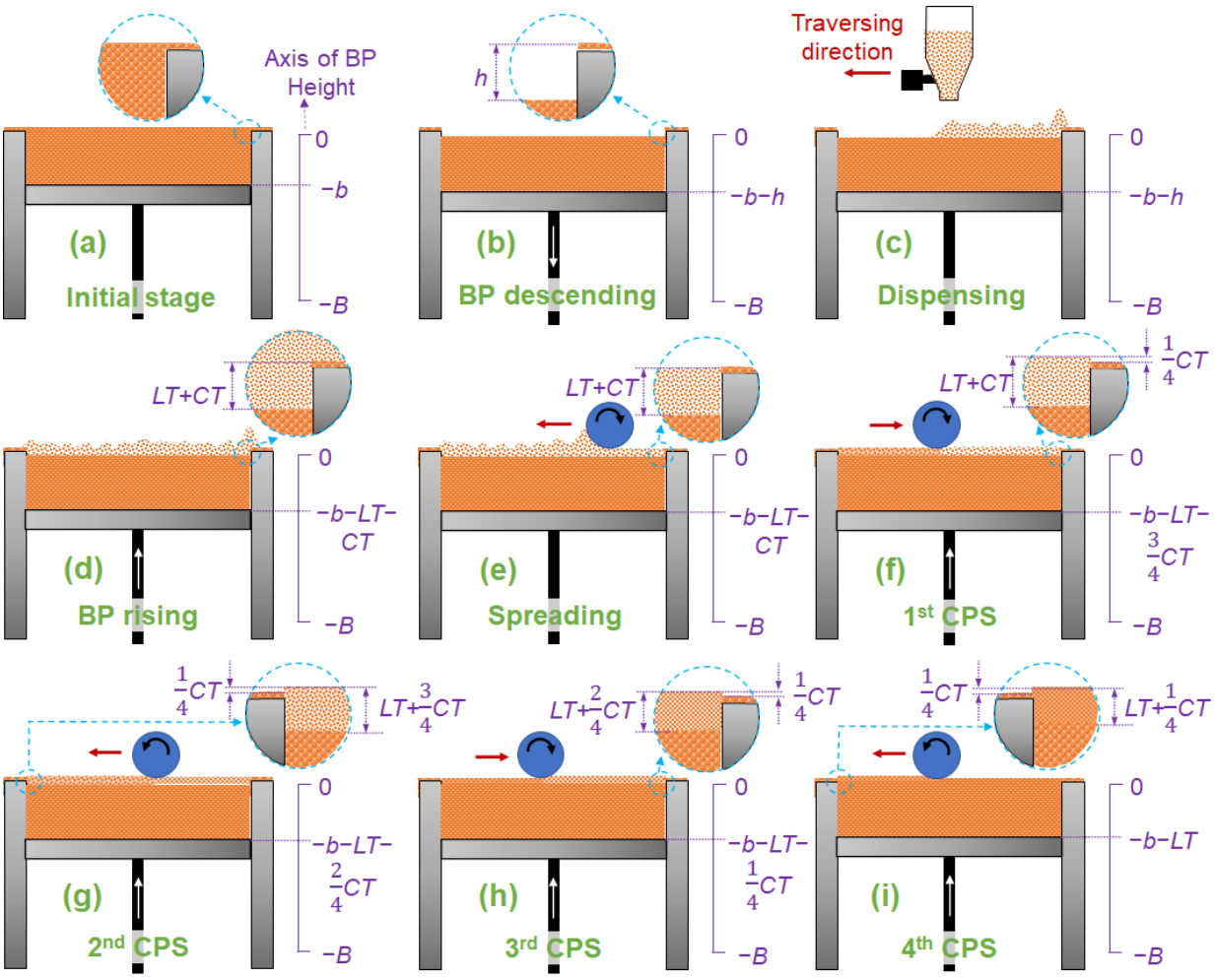

Figure 8.4 Schematic of normal recoating with compaction through four compaction pass segments (CPS) conducted at an arbitrary build platform (BP) position of *-b*: (a) initial stage, (b) BP descending, (c) powder dispensing, (d) BP rising, (e) counter-rotating roller spreading, (f) first CPS, (g) second CPS, (h) third CPS, and (i) fourth CPS

Table 8.3 Comparison among all three recoating functions used in this study

Recoating	BP height before recoating	BP height during spreading	BP height change after recoating
Level recoating without compaction	0 (Figure 2(a))	0 (Figure 2(e))	0 (Figure 2(e))
Level recoating with compaction	0 (Figure 3(a))	*-CT* (Figure 3(e))	0 (Figure 3(i))
Normal recoating with compaction	*-b* (Figure 4(a))	*-b-LT-CT* (Figure 4(e))	*-LT* (Figure 4(i))

Optimal compaction ratio locating (as shown in the middle column of Figure 1) was conducted as follows. After foundation preparation, four layers of normal recoating with compaction using a high compaction ratio of 11 (at a LT of 20 μm and CT of 200 μm) were conducted first. If compaction-induced defects were observed during recoating, the compaction ratio would be lowered by increasing the LT value or decreasing the CT value (depending on the current LT value), and another four layers of normal recoating with compaction were conducted. Finally, the first (i.e., the largest) compaction ratio without compaction-induced defects was located as the optimal compaction ratio for powder bed formation.

It should be noted that there was some powder dropping at the edges of the build box during compaction, especially at high compaction ratios. Therefore, not all powder dispensed on the BP and/or powder bed would be compacted to form the compacted powder layer. This was the reason that high compaction ratios could be used.

8.2.4.3. Powder bed formation

After locating the optimal compaction ratio for each granulated powder, powder bed formation (as shown in the right column of Figure 1) was conducted to a total powder bed height of 5 mm by normal recoating with compaction through four CPS (as illustrated in Figure 3). Parameters used for powder bed formation are the same as those for foundation preparation (as listed in Tables 1 and 2). Since numerous layers were repeatedly spread and the compacted powder layers were relatively consistent, powder bed formation was conducted once for each granulated powder.

8.2.5. Powder bed density measurement

Powder bed density was calculated based on the measurements of whole powder bed dimension and mass. Specifically, the height of the powder bed was measured by a caliper (with a

resolution of 0.01 mm) at the four corners of the build box with three repetitions at each corner, as well as the length and width of the build box. Afterward, the powder left inside the build box was collected and its mass was measured. The mass was then divided by the volume of the whole powder bed to calculate the powder bed density. Relative powder bed density was finally calculated based on the theoretical density of alumina (i.e., 3.97 g/cm^3 [17]).

8.3. Results and Discussion

8.3.1. Granule morphology

The granule morphology was shown in Figure 5. The granules have an irregular shape and a rough surface. Both characteristics could decrease granule sliding by increased intergranular interlocking and consequently benefit the powder bed compaction.

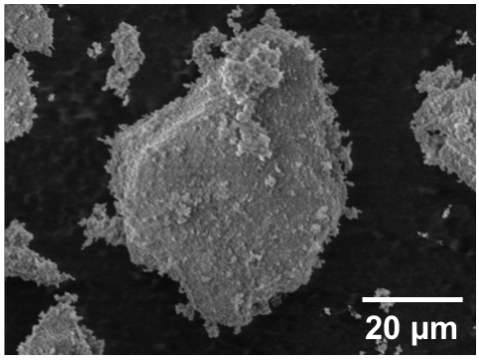

Figure 8.5 SEM of granulated powder (slurry solid loading of 2 vol.%)

8.3.2. Apparent density

As listed in Table 4, relative apparent density results show an increasing trend as slurry solid loading increases. Possible reasons for the increasing trend include the increasing solid loading and consequent intragranular density.

Table 8.4 Apparent densities of granulated powders

Slurry solid loading (vol.%)	Relative apparent density (%)
2	6.3
5	6.2
10	7.1
15	8.3

8.3.3. Powder bed defects and optimal compaction ratios

At high compaction ratio values, compaction-induced powder bed defects occurred. Surface ridge was one of the most common defects that occurred on the powder bed while the optimal compaction ratio was being located. As shown in Figures 6(a–c), at a compaction ratio of 11, surfaces ridges appeared on the powder layers after normal recoating with compaction of 10 and 15 vol.% granulated powders, while there were no surface ridges from the normal recoating with compaction of 2 and 5 vol.% granulated powders. It should be noted that under the same recoating settings, the larger the compaction ratio, the more the surface ridges on the powder bed.

Edge ridge is another kind of compaction-induced powder bed defect that appears at the edge of the build box. It appeared in two cases: (1) at the end of 20 layers of level recoating with compaction in foundation preparation of all powders, and (2) during optimal compaction ratio locating of 2 vol.% granulated powder at a compaction ratio of 11. Moreover, the higher the compaction ratio, the larger and higher the edge ridge.

The location where edge ridge appeared depended on the traversing direction of the final CPS. As shown in Figure 6(c), the edge ridge appeared only at the right-side edge of the build box while the roller traversed from right to left for the final CPS. As shown in Figures 6(c) and 6(d), the edge ridge was right above the boundary line between the powder bed and the build box. This means

that the powder bed was distorted and powder was shifted towards the right side, leading to powder accumulation near the right edge of the build box.

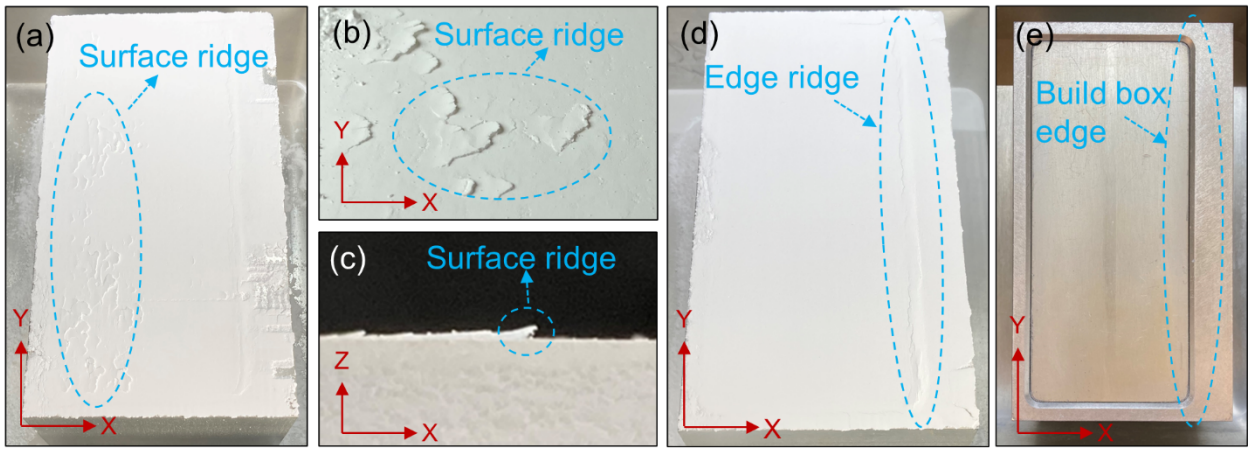

Figure 8.6 (a) surface ridge on powder bed, (b) and (c) close-up photos of surface ridge on different coordinate planes, (d) edge ridge at right edge of build box, and (e) empty build box

The resultant optimal compaction ratios with corresponding LT and CT values are listed in Table 5. Due to the (minor) edge ridges for the 2 vol.% granulated powder at the beginning of optimal compaction ratio locating, the compaction ratio was decreased by increasing LT from 20 µm to 30 µm (leading to a compaction ratio of 7.67). The 5 vol.% granulated powder had no compaction-induced defects during optimal compaction ratio locating and powder bed formation even using the highest compaction ratio of 11. Due to the severe surface ridges that appeared on the powder beds, the powder bed formation using 10 and 15 vol.% granulated powders had to use much lower compaction ratio (i.e., 2.25 for 10 vol.% granulated powder and 2.67 for 15 vol.% granulated powder). These findings suggest that, as slurry solid loading decreased, compactibility (i.e., the ability to be compacted by a forward-rotating roller without compaction-induced defects) increased. Therefore, powder beds from 2 and 5 vol.% granulated powders can be flawlessly formed with high compaction ratios. On the contrary, the 10 and 15 vol.% granulated powders

cannot be compacted at high ratios due to much more compaction-induced defects on the powder bed.

Table 8.5 Optimal compaction ratios with corresponding layer and compaction thicknesses

Slurry solid loading (vol.%)	Layer thickness (μm)	Compaction thickness (μm)	Optimal compaction ratio
2	30	200	7.67
5	20	200	11.0
10	120	150	2.25
15	120	200	2.67

8.3.4. Powder bed density

The powder bed densities achieved after powder bed formations by four granulated powders are listed in Table 6. The 2 vol.% granulated powder achieved the highest powder bed density of 19.5%. This is significantly higher than the powder bed density (15.8%) achieved by a spherical granulated powder without compaction [8]. This increase in the powder bed density indicates the effectiveness of compaction. Moreover, the irregular granule shape might have benefitted the powder bed density by intergranular interlocking during compaction.

Table 8.6 Powder bed densities achieved by all granulated powders

Slurry solid loading (vol.%)	Powder bed density (%)
2	19.5
5	17.2
10	14.6
15	16.0

8.3.5. Compactibility

As discussed in Section 3.3, the compactibility of a powder is critical for a high powder bed density under forward-rotating roller compaction. Since the highest powder bed density without

compaction-induced defects on powder bed, as shown in Section 3.4, has been measured, the compactibility of each granulated powder is assessed by the ratio of powder bed density with compaction to that without compaction in this paper. Moreover, apparent density is a strong predictor for powder bed density without compaction [18]. Therefore, the compactibility for each granulated powder can be quantified as the ratio of powder bed density with compaction to apparent density, as in the following equation:

$$C = \frac{\rho_{PB}}{\rho_A} \tag{1}$$

where C is the compactibility, and ρ_{PB} and ρ_A are the powder bed density after compaction and apparent density, respectively.

The calculated compactibilities for four granulated powders are shown in Figure 7. All compactibilities in Figure 7 are larger than one, indicating that powder bed density significantly increased (compared with apparent density) after compaction. The 2 vol.% granulated powder has the highest compactibility of 3.10. Furthermore, the compactibilities of 2 and 5 vol.% granulated powders are much higher than those of 10 and 15 vol.% ones. The reason for the higher compactibility of granulated powders with lower solid loadings will be investigated in future work.

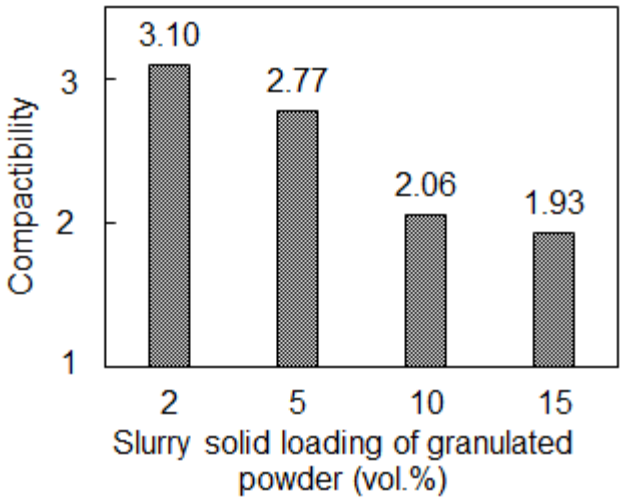

Figure 8.7 Compactibilities for four granulated powders

8.4. Conclusions

Four slurries with different solid loadings of 2, 5, 10, and 15 vol.% were prepared for granulation. A commercially available binder jetting printer equipped with a forward-rotating roller compaction system was used afterward for investigating the effect of slurry solid loading on powder bed conditions. Compactibility, defined as the ratio of powder bed density with compaction to apparent density, was calculated for each granulated powder. The granulated powder prepared at a slurry solid loading of 2 vol.% achieved the highest powder bed density of 19.5% as well as the highest compactibility of 3.10. This study indicates that a low slurry solid loading helps enhance powder bed density in roller-compaction-assisted binder jetting.

8.5. References

[1] ASTM International/International Standard, 2015, “ISO/ASTM 52900:2015 - Additive Manufacturing — General Principles — Terminology.”

[2] Li, M., Du, W., Elwany, A., Pei, Z., and Ma, C., 2020, “Metal Binder Jetting Additive Manufacturing: A Literature Review,” Journal of Manufacturing Science and Engineering, **142**(9), p. 090801 (17 pages).

[3] Du, W., Ren, X., Pei, Z., and Ma, C., 2020, "Ceramic Binder Jetting Additive Manufacturing: A Literature Review on Density," Journal of Manufacturing Science and Engineering, **142**(4), p. 040801 (19 pages).

[4] Yin, X., Travitzky, N., Melcher, R., and Greil, P., 2006, "Three-Dimensional Printing of TiAl3/Al2O3 Composites," Zeitschrift für Metallkunde, **97**(5), pp. 492–498.

[5] Fu, Z., Schlier, L., Travitzky, N., and Greil, P., 2013, "Three-Dimensional Printing of SiSiC Lattice Truss Structures," Materials Science and Engineering A, **560**, pp. 851–856.

[6] Chumnanklang, R., Panyathanmaporn, T., Sitthiseripratip, K., and Suwanprateeb, J., 2007, "3D Printing of Hydroxyapatite: Effect of Binder Concentration in Pre-Coated Particle on Part Strength," Materials Science and Engineering C, **27**(4), pp. 914–921.

[7] Gildenhaar, R., Knabe, C., Gomes, C., Linow, U., Houshmand, A., and Berger, G., 2011, "Calcium Alkaline Phosphate Scaffolds for Bone Regeneration 3D-Fabricated by Additive Manufacturing," Key Engineering Materials, **493**, pp. 849–854.

[8] Miao, G., Du, W., Moghadasi, M., Pei, Z., and Ma, C., 2020, "Ceramic Binder Jetting Additive Manufacturing: Effects of Granulation on Properties of Feedstock Powder and Printed and Sintered Parts," Additive Manufacturing, **36**, p. 101542.

[9] Du, W., Miao, G., Liu, L., Pei, Z., and Ma, C., 2019, "Binder Jetting Additive Manufacturing of Ceramics: Feedstock Powder Preparation by Spray Freeze Granulation," *ASME 2019 14th International Manufacturing Science and Engineering Conference*, Erie, PA, p. V001T01A006 (6 pages).

[10] Li, M., Wei, X., Pei, Z., and Ma, C., 2021, "Binder Jetting Additive Manufacturing: Observations of Compaction-Induced Powder Bed Surface Defects," Manufacturing Letters, **28**, pp. 50–53.

[11] Budding, A., and Vaneker, T. H. J., 2013, "New Strategies for Powder Compaction in Powder-Based Rapid Prototyping Techniques," Procedia CIRP, **6**, pp. 527–532.

[12] Yoo, J., 1996, "Fabrication and Microstructural Control of Advanced Ceramic Components by Three Dimensional Printing," Massachusetts Institute of Technology.

[13] Niino, T., and Sato, K., 2009, "Effect of Powder Compaction in Plastic Laser Sintering Fabrication," *Solid Freeform Fabrication Symposium*, Austin, TX, pp. 193–205.

[14] ASTM International, 2017, "B212-17: Standard Test Method for Apparent Density of Free-Flowing Metal Powders Using the Hall Flowmeter Funnel."

[15] ASTM International, 2000, "C 1444-00: Standard Test Method for Measuring the Angle of Repose of Free-Flowing Mold Powders."

[16] Du, W., Miao, G., Pei, Z., and Ma, C., 2021, "Comparison of Flowability and Sinterability among Different Binder Jetting Feedstock Powders: Nanopowder, Micropowder, and Granulated Powder," Journal of Micro- and Nano-Manufacturing, 2021, 9(2): 021008 (8 pages).

[17] Rahaman, M. N., 2003, *Ceramic Processing and Sintering*, CRC Press, New York.

[18] Li, M., Miao, G., Moghadasi, M., Pei, Z., and Ma, C., 2021, "Ceramic Binder Jetting Additive Manufacturing: Relationships among Powder Properties, Feed Region Density, and Powder Bed Density," Ceramics International, **47**(17), pp. 25147–25151.

APPENDIX A

Supplementary data for Figure 2.9

Special treatment	Density or porosity type	Value (%)	Standard deviation (%)	Reference
/	Bulk density	32	/	[55]
/	Bulk porosity	60.5	1.4	[108]
/	Bulk density	40	/	[82]
/	Bulk density	46.8	1.9	[61]
/	Bulk density	50.7	/	[62]
/	Bulk density	55	/	[73]
/	Apparent porosity	35.28	/	[158]
G	Bulk density	31	/	[68]
G	Bulk density	35.3	/	[67]
G	Bulk density	36	/	[68]
G	Bulk density	42	/	[91]
G	Apparent solid density	45	/	[60]
G	Bulk density	45.9	/	[86]
L	Bulk density	54	/	[25]
L	Bulk density	57.2	/	[38]
L	Bulk density	58	/	[27]
L	Bulk density	63.4	/	[23]
L	Bulk density	66	/	[77]
L	Bulk density	67	/	[24]
S	Bulk density	36.05	0.57	[54]
S	Bulk density	39.6	0.6	[59]
S	Bulk density	45	/	[74]
S	Bulk porosity	55	/	[153]
S	Bulk density	65.7	/	[62]
S, G	Apparent porosity	55	/	[88]
S, G	Bulk porosity	55	/	[87]

APPENDIX B

Supplementary data for Figure 2.10

Special treatment	Density or porosity type	Value (%)	Standard deviation (%)	Reference
/	Bulk density	35	/	[55]
/	Bulk density	38.4	/	[69]
/	Apparent porosity	46.07	8.52	[127]
/	Bulk density	55.89	/	[89]
/	Apparent porosity	41.42	4.35	[154]
/	Apparent solid density	65.2	/	[167]
/	Bulk porosity	32.1	2.6	[108]
/	Bulk porosity	32	/	[107]
C	Bulk density	55.3	/	[53]
C	Bulk porosity	12.9	0.5	[83]
G	Apparent solid density	32.2	/	[85]
G	Bulk density	38.78	3.64	[130]
G	Apparent porosity	59.43	/	[147]
G	Bulk density	42.95	1.6	[125]
G	Bulk density	43.2	/	[155]
G	Bulk density	48	/	[124]
G	Apparent solid density	48	/	[60]
G	Apparent porosity	51	0.9	[152]
G	Bulk density	62.5	/	[68]
G	Apparent porosity	36	/	[70]
G	Bulk density	67	/	[67]
G	Apparent solid density	91.4	2.8	[133]
I	Bulk density	85	/	[69]
L	Bulk density	99	/	[24]
L	Bulk density	99.9	/	[27]
M	Bulk porosity	65.3	/	[142]
M	Bulk porosity	44	/	[106]
M	Bulk density	66	/	[96]
M	Bulk density	72	2	[95]
M	Bulk density	94.5	/	[171]
P	Bulk density	60.1	/	[55]
P	Bulk density	94.33	/	[89]
S	Bulk density	65.5	2.4	[57]
S	Bulk porosity	30	/	[153]

S	Apparent solid density	96	/	[166]
G, I	Bulk porosity	19	0.5	[71]
G, I	Bulk density	91	/	[86]
G, I	Apparent porosity	2.4	/	[85]
G, P	Bulk density	97.8	/	[68]
G, S	Bulk density	86.8	/	[94]
M, G	Bulk density	45.06	3.05	[130]
M, G	Bulk density	52.84	2.76	[131]
M, G	Apparent solid density	95.1	4.72	[133]
M, G	Bulk density	95.74	/	[91]
M, G	Apparent porosity	2.5	0.12	[101]
M, G	Apparent solid density	99	0.1	[144]
M, L	Bulk porosity	8.79	1.44	[77]
M, L	Bulk density	99.2	/	[38]
M, S	Bulk density	54.8	/	[97]
M, G, P	Bulk density	99.2	/	[68]
M, G, C	Bulk porosity	48	2	[102]
M, G, I	Apparent porosity	1.7	/	[88]
M, L, P	Bulk density	100	/	[93]
M, S, G	Bulk density	53.01	/	[99]

APPENDIX C

Supplementary data for Figure 2.13

Density before sintering			Density after sintering (%)	Reference
Powder bed density (%)	**Green density (%)**	**Pressed green density (%)**		
39.7	/	/	46.8	[57]
45.2	/	/	50.7	[57]
51	/	/	87.1	[83]
53	/	/	100	[93]
57.1	/	/	57.5	[57]
58.2	/	/	60.5	[57]
59.5	/	/	64.3	[57]
53.6	/	/	64.8	[57]
61.7	/	/	65.5	[57]
67	/	/	99	[24]
/	31	/	62.5	[68]
/	32	/	35	[55]
/	43.6	/	61.5	[67]
/	45	/	48	[60]
/	45	/	70	[153]
/	46.9	/	64.1	[67]
/	48	/	67	[67]
/	57.2	/	99.2	[38]
/	58	/	99.9	[27]
/	/	47	87.9	[68]
/	/	54	95.9	[68]
/	/	56	97.8	[68]
/	/	61	99.2	[68]